Fall 2010

High temperature tolerant optical fiber inline microsensors by laser fabrication

Tao Wei

Department: Electrical and Computer Engineering

HIGH TEMPERATURE TOLERANT OPTICAL FIBER INLINE MICROSENSORS BY LASER FABRICATION

by

TAO WEI

A DISSERTATION

Presented to the Faculty of the Graduate School of the

MISSOURI UNIVERSITY OF SCIENCE AND TECHNOLOGY

In Partial Fulfillment of the Requirements for the Degree

DOCTOR OF PHILOSOPHY

in

ELECTRICAL ENGINEERING

2010

Approved by

Dr. Hai Xiao, Advisor
Dr. Hai-Lung Tsai, Co-advisor
Dr. David J. Pommerenke
Dr. Steve. E. Watkins
Dr. Reza Zoughi

ABSTRACT

Fiber sensors are particularly attractive for harsh environment defined by high temperature, high pressure, corrosive/erosive, and strong electromagnetic interference, where conventional electronic sensors do not have a chance to survive. However, the key issue has been the robustness of the sensor probe (not the fiber itself) mostly due to the problems stemmed from the traditional assembly based approaches used to construct fiber optic sensors. For example, at high temperatures (e.g., above 500°C), the thermal expansion coefficient mismatch between different composited parts has a high chance to lead to sensors' malfunction by breaking the sensor as a result of the excessive thermo-stress building up inside the multi-component sensor structure. To survive the high temperature harsh environment, it is thus highly desired that the sensor probes are made assembly-free. We are proposing to fabricate assembly-free fiber sensor probes by manufacturing various microstructures directly on optical fibers.

This dissertation aims to design, develop and demonstrate robust, miniaturized fiber sensor probes for harsh environment applications through assembly-free, laser fabrication. Working towards this objective, the dissertation explored three types of fiber inline microsensors fabricated by two types of laser systems. Using a CO_2 laser, long period fiber grating (LPFG) and core-cladding mode interferometer sensors were fabricated. Using a femto-second laser, an extrinsic Fabry-Perot interferometric (EFPI) sensor with an open cavity was fabricated. The scope of the dissertation work consists of device design, device modeling/simulation, laser fabrication system setups, signal processing method development and sensor performance evaluation and demonstration.

This research work provides theoretical and experimental evidences that laser fabrication technique is a valid tool to fabricate previously undoable miniaturized photonic sensor structures, which can avoid complicated assembly processes and, as a result, enhance robustness, functionality and survivability of the sensor for applications in harsh environments. In addition, a number of novel optical fiber sensor platforms are proposed, studied and demonstrated for sensing and monitoring of various physical and chemical parameters in high temperature harsh environments.

ACKNOWLEDGMENTS

I would like to take this opportunity to thank all those people who helped me with the successful completion of my research. First, I would like to express my gratitude to my advisor Dr. Hai Xiao, without who this research could be considered incomplete. I thank him for giving me a chance to work with him and for his continued support with valuable advice and encouragement. His subtle guidance with unbelievable patience has made a great impact on this research and me. Also, I would like to thank my co-advisor Dr. Hai-Lung Tsai, Dept. of Mechanical and Aerospace Eng., for his very generous help on research facilities and wonderful advices along the way I was pursuing my degree.

I am grateful to Dr. David Pommerenke, Dr. Steve Watkins and Dr. Reza Zoughi, Dept. of Electrical and Computer Engineering, for their very well organized classes, which cultivated my interest in study and inspired my research work. Also, I am much honored to have them as my committee members.

Additional gratitude is owed to all the members and alumni from Dr. Xiao's research group. I am very happy to work with everybody during my stay in this lab. Also, special thanks go to two out-of-department PhD students, Yukun Han and Ying Huang, from mechanical and civil engineering, respectively. It was a great learning experience for me to work with these two ladies. Many thanks should go to Xiaotong Wei, Carrie Eggen, Dept. of Chemical Eng., Arizona State University, and Xiling Tang, Dept. of Chemical Eng., University of Cincinnati. It was wonderful to collaborate with them.

I am very grateful to Prof. Junhang Dong, Department of Chemical Engineering, University of Cincinnati, for his help on my graduate study as well as my research work.

I thank my parents for everything they have done for me and I am happy that they agree to participate in my commencement all the way from the opposite of the earth.

Finally, I would like to thank the sponsors for this project. They are the U.S. Department of Energy through the National Energy Technology and the Office of Naval Research through the Young Investigator Program. Also, I would like to thank Center for Transportation Infrastructure and Safety, National University of Transportation Center for the 2008-2009 fellowship support.

TABLE OF CONTENTS

Page

LIST OF ILLUSTRATIONS

1. INTRODUCTION

This chapter presents a general introduction of optical fiber sensors with a special interest on their unique and attractive attributes toward various sensing applications in high-temperature harsh environments. A brief review of the current state-of-the-art harsh environment sensing technologies is provided. The challenges, limitations and unsolved issues are summarized. Consequently, the research objectives and the scientific /technical topics to be addressed by this dissertation are derived. After a brief description of the scope of the dissertation work, the research innovations are summarized in the context of design, development and demonstration of a number of novel, robust inline optical fiber micro-sensors uniquely fabricated by assembly-free laser fabrications.

1.1. BACKGROUND

The field of fiber optics has undergone tremendous growth and advancement over the past several decades. Initially considered as a medium to deliver light and images for medical endoscopic applications, optical fibers were later proposed as an information carrying medium for telecommunication applications in the mid 1960's [1]. Charles K. Kao and George A. Hockham of the British company Standard Telephones and Cables (STC) were the first to promote the idea that the attenuation in optical fibers could be reduced below 20 dB/km, allowing fibers to be a practical medium for communication [2]. Since then, considerable research efforts have been carried out. Today, optical communication has become the preferred method to transmit vast amounts of data and information over a long distance.

As shown in Fig. 1.1, a typical communication optical fiber is a cylindrical optical waveguide consisting of a number of layers. The center layer typically made of doped glass is the core of the fiber where most of the light energy is confined. The middle layer is typically made of fused silica glass. The outer layer, typically made of polymer or plastic materials, is the buffer and/or jacket for the purpose of reinforcing the mechanical strength. From the optical perspective, the refractive index of the core is higher than that

of the cladding. The light is guided inside the core as a result of total internal reflection (TIR) at the core-cladding interface.

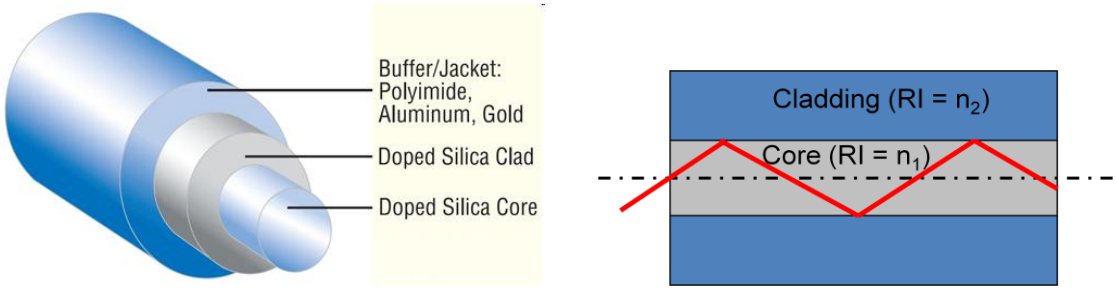

Figure 1.1 Schematic of layered optical fiber structure and the demonstration of wave guided in an optical fiber core under TIR condition

Fibers which support many propagation paths or transverse modes are called multi-mode fibers (MMF), while those which can only support a single mode are called single-mode fibers (SMF). MMFs generally have a larger core diameter, and are used for short-distance communication links. On the other hand, SMFs are used for most communication links longer than one thousand meters.

Besides its communication applications, optical fibers have also been used widely for constructing various sensors for the measurement of strain, temperature, pressure, magnetic and electric field, chemical and biological parameters sensing and etc. [3-10] Compared with electrical sensors, fiber optic sensors (FOS) offer many intrinsic advantages such as,

- Light weight, small size and energy efficient
- High sensitivity, large bandwidth and dynamic range
- Resistance to harsh environment such as high temperature, high pressure and corrosion/erosion
- Insensitivity to electromagnetic interference (EMI)
- Long-distance remote operation
- Capability of multiplexing of many sensors along a single optical fiber

Optical fiber sensors are often loosely classified into two basic categories referred to as extrinsic (or hybrid) optical fiber sensors, and intrinsic (or all fiber) sensors. Fig. 1.2 illustrates the concepts of these two types of optical fiber sensors. The upper one is the

case of an intrinsic sensor. In this case, an optical fiber is used for both light transmission and signal transduction. The parameters to be measured directly affect the light wave transmitted inside the optical fiber. The lower one in Fig. 1.1 shows the idea of an extrinsic optical fiber sensor. In this case, the optical fiber serves as the light transmission medium only and the transducer is outside the fiber. Through the external transducer, the parameters to be measured modulate the phase, intensity, frequency, polarization, spectral content of the light. An optical fiber then carries the light with the environmentally impressed information to a light detector for signal recording and processing. Sometimes, optical fiber sensors can operate in reflection mode in which the lead-in optical fiber acts as the output fiber.

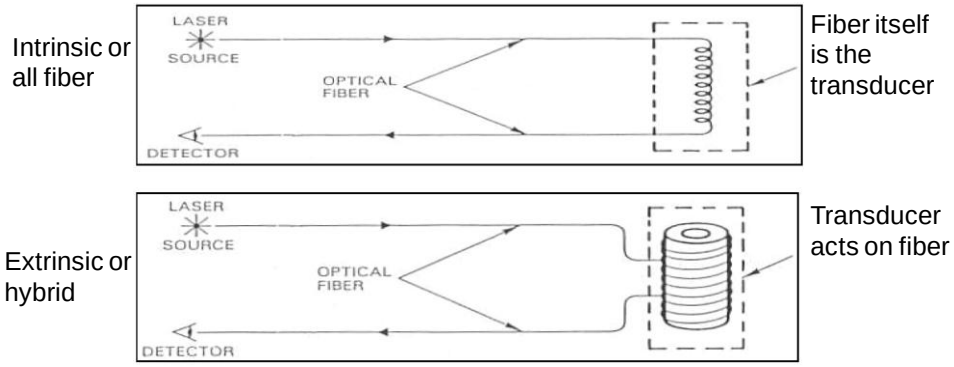

Figure 1.2 Classification optical fiber sensors

Fiber optic sensors have been long-envisioned as a cheap and reliable solution for many applications, where inexpensive, miniaturized fiber-pigtailed sensor probes can be deployed to otherwise inaccessible areas for fast and accurate measurement of a wide variety of physical, chemical, and biological quantities. However, although the past half century has seen a steady growth of appearance of optical fibers in various industry sectors, the fiber sensor market has not seen the boom as predicted. On the contrary, many of the unique advantages of fiber sensors are yet to be fully harvested. The conflicting picture suggests that the realization of the full potentials offered by fiber sensors requires continuing research innovations.

1.2. SENSORS FOR HARSH ENVIRONMENT APPLICATIONS

Sensors and sensor systems that are capable of surviving and operating in harsh environments have found many applications in modern industry. Examples include oil and gas extraction, power generation, coal gasification, gas turbine operation, aircraft engineer design and monitoring, and petrochemical refining and separation. The term "hash environment" can be the summary of a lot of extreme conditions including high temperature, high pressure, chemically corrosive/erosive, toxic, explosive, radioactive, and strong electromagnetic disturbance. These extreme conditions normally prevent the usage of commercially available, general purpose electrical sensors. Optical fiber sensors, with its glass nature and optical interrogation principle, may provide a viable solution for sensing and monitoring in these harsh conditions [11].

There exist a number of important considerations for sensors targeting harsh environment applications. First, the sensor needs to survive the harsh environment. This requires that the sensor material, structure, package, and connection must be robust to experience drastic changes in environmental conditions such as a large temperature swing. Second, the sensor structure needs to be stable to operate in these extreme conditions. The common concerns for sensors targeting harsh environment applications include the long-term stability and cross-sensitivity. Long-term stability requires that the sensor does not drift as a result of structural degradation when placed in an extreme environment. Cross-sensitivity, especially the temperature cross-sensitivity, could result in large amount of measurement error induced by changes in environmental parameters other than the one to be measured/monitored. In most cases, more than one adverse parameter can be found in a typical harsh environment. For example, in a combustion engine, high temperature and high pressure coexist at the same time. In this case, a pressure sensor for engine monitoring should have zero response to temperature change. Third, the accessibility of the sensor needs to be considered. Sometimes, engineers found that even if the sensor itself survived harsh environments, it is hard to route the cable to attach the sensor or the cable may not survive the environment as the sensor does. Or it is simply not possible to place the sensor in the shielded environment, for example, to monitor the inner environment of an ignition chamber of a combustion engine, once

needs to intrusively deploy the sensors, making the ignition less efficient or even bringing in safety issues.

In the past, a number of technologies have been explored for harsh environment sensing. Here we summarize four general research and development areas, representing the current state-of-the-art the directions.

High temperature electronic sensors: Specially designed electronic sensors and circuits have been investigated for high temperature applications. Many of the research efforts have focused on the silicon-on-insulator (SOI) technology. Representative examples include thin or thick film SOI devices for temperature measurement [12], piezoresistive SOI sensors for stress/strain measurement [13], and surface acoustic wave (SAW) SOI sensors for pressure measurement [14]. These sensors had shown high resolution for applications in high temperatures up to 700 ℃. Sensors have also been developed using silicon carbide (SiC) and silicon nitride (SiN) substrates which can operate at temperatures as high as 800 ℃ [15]. However, these electronic devices are inherently sensitive to EMI, which renders relatively low accuracy in measurement. In addition, the strong temperature dependence (thus large temperature cross-sensitivity) has also made it difficult to develop sensors for measurement of parameters other than temperature.

MEMS sensors: Microelectromechanical systems (MEMS) technology has been investigated for fabrication of miniaturized sensors to measure temperature, pressure, strain and accelerations. These MEMS devices were manufactured using standard IC processing along with orientation dependent (or anisotropic) etching and wafer bonding [16-19]. Optically interrogated MEMS devices are expected to be more suitable than electrically interrogated MEMS devices for harsh environment applications [16, 17]. MEMS-based sensors have the advantages of small size, high sensitivity, low cost, potential of large production, and batch fabrication process for a large production yield. However, a major problem associated with most MEMS sensor is its inherent cross sensitivity to temperature. For example, the influence of temperature on a piezoresistive MEMS pressure sensor can cause a drift of about 100 Pa per day, which makes them deficient for long-term measurement [20]. The packing is always a challenge for MEMS

sensors. As a result, MEMS sensors are limited for applications in temperatures below 600 ℃ [19].

Silica optical fiber sensors: Optical fiber sensors are very attractive for applications in harsh environment due to their abovementioned advantages of small size, lightweight, immunity to EMI, resistance to chemical corrosion, high sensitivity, large bandwidth, and remote operation capability [21, 22]. In addition, some of accessibility issue will be automatically solved by applying the optical fiber sensor. For example, because the optical fiber itself is a transmission line, the transducer collected sensing signals can be easily sent to the base station placed far away from the harsh environment site via high temperature harsh environment survivable cable, optical fiber. Moreover, its small size makes it possible to apply within very limited space and the small scale would less disturb the application fields as well.

Among the many types of fiber sensors, fiber Bragg gratings (FBG) and long period fiber gratings (LPFG) are the most extensively investigated. Fiber grating sensors have the advantages of immunity to the optical power loss variation of the optical network and the capability of multiplexing many sensors to share the same signal processing unit [23-26]. Fiber gratings made by CO_2 laser irradiation, chemical etching, mechanical dicing and electric arc modification have successfully survived temperatures up to 1200 ℃ [27]. Among these high temperature survivable LPFG fabrication techniques, using CO_2 laser irradiation to induce periodic refractive index change is supreme to other fabrication approaches for the reason that the perturbed area, unlike others, does not decrease the mechanical strength of the optical fiber. Also, CO_2 laser fabrication stage is comparatively simple to set up, which makes it more attractive. However, although the analytical and numerical modeling of LPFG have been widely investigated during the past decade, there is always a key parameter missing in the chain of relating the model to the real device, which makes the math model only valid for understanding, but not a good tool for quantitative analysis in most cases [28, 29]. This parameter is the amount of index modulation induced by CO_2 laser exposure. The refractive index change at each localized grating point is at a scale of 10^{-4}, making it very hard to be measured experimentally, using the most popular reflection coefficient based measurement. As a result, the existence of this gap results in the fact that the fabrication

of LPFG is more or less guided by trial-and-error, preventing LPFG from mass production. In addition, their long-term reliability has been a concern due to the degradation of optical properties and mechanical strength when the grating is exposed to high temperature and high pressure environments. Moreover, fiber grating sensors exhibit relatively large cross-dependence of temperature which limits their scale of applications in harsh environments.

Hermetically packaged extrinsic fiber Fabry-Perot interferometers (EFPI) have also been successfully applied to harsh environment applications [30-32]. The laser fusion or electric arc sealed cavity was successfully tested for measurement of temperature (up to 800 ℃) and pressure (up to 10,000 psi). Micromachined single crystal silicon carbide Fabry-Perot interferometer temperature and pressure sensors have also been demonstrated for high temperature applications [33, 34]. However, fabrications of these EFPI sensors involve complicated procedures of assembling multiple components together, which compromise the robustness of the device due to the limited strength of the joints. The mismatch of the coefficient of thermal expansion (CTE) of the various parts can also seriously lower the thermal stability of the device.

Based on the above reviews, it is clear that, in spite of the large amount of progress made in the past toward high temperature harsh environment sensing, there still exist technical challenges and issues that are missing appropriate solutions and the current state-of-art technologies do not provide satisfactory solutions. Among most of the high temperature sensors, survivability is still an issue, since they are manufactured through assembling a number of components. And in most cases, these components are made by different materials, which making it less mechanically stable at higher temperatures. The CTE mismatch of different components would induce dominant stress in between the different components and eventually damage the device from inside at elevated temperatures. This problem challenges the packaging of the sensors associated with assembly process. Another common issue among these sensors is the temperature cross-sensitivity. Although it may be more evident for electric based sensors, temperature cross-sensitivity is critical in optical based sensor as well at higher temperatures. To deal with this, the conventional way is to place a high accuracy temperature sensor next to the original sensor designed for a specific parameter monitoring. Apparently, this would

increase the sensor operating expense. In addition, the strong electromagnetic field may couple into the sensor system, either from sensor probe or from the trace routing to the sensor head. Specifically in LPFG based sensor system, the lack of accurate measurement of CO_2 laser induced index modulation restricts the modeling work to be used to guide the design and fabrication. Thus, current immatureness of current high temperature harsh environment sensors is still challenging the researchers on how to achieve improvement on the above listed issues.

Sapphire fiber based sensors: Single crystal sapphire fibers with a high melting point of about 2053 ℃, low optical loss in a large spectrum window, superior mechanical strength, and excellent resistance to chemical corrosion, is a good candidate for high temperature sensing platform. Up to date, a number of sapphire fiber sensors have been demonstrated by various research groups. Examples include: 1) sapphire rod blackbody radiation-based temperature sensors [35], 2) sapphire fiber temperature sensors based on birefringence-balanced polarimetry [36], 3) EFPI sensors made by bonding sapphire fibers on a ceramic substrate for measurement of temperature, strain, and pressure [36], and 4) intrinsic Fabry-Perot interferometric (IFPI) sensors by attaching a sapphire fiber to a sapphire plate for temperature measurement [37]. Although these sensors have been demonstrated for high temperature (>1000 ℃) applications in laboratory and field tests, their long term stability is a concern due to the use of ceramic epoxies in device fabrication. More recently, a sapphire fiber grating based temperature sensor was demonstrated [38, 39]. However, the grating has a very weak strength due to the highly multimode nature of a non-cladded sapphire fiber, resulting in poor measurement accuracy.

Another major issue related to sapphire fiber based high temperature sensor stems from its uncladded nature. Single crystal sapphire fibers cannot be grown as a core-clad structure from source rod-in-tube because convective currents in the molten zone quickly destroy the geometrical structure of the source rod [40, 41]. Uncladded sapphire fibers suffer from a number of undesirable characteristics such as unpredictable loss and highly multimode operation. The unpredictable loss during applications may impose a large error to the measurement results. The highly multimode nature makes it difficult to obtain

high quality sensor signal in conventional assembly based sensor constructions, especially when optical interference is used as the sensing principle.

1.3. MOTIVATIONS AND OBJECTIVES

Applications and Motivations: This research was initially motivated by developing novel sensing or monitoring in extreme environments of fossil energy systems. The societal impact of improvements in efficiency of existing fossil-fuel infrastructure can be very substantial. According to the International Energy Agency's 2002 World Energy Outlook, renewable energy sources (including hydro) provided about 5% of the world's energy use in 2000, and they project the growth in renewables to barely keep-up with the growth in demand providing 6.5% in 2030 [42]. Energy forecasts predict that fossil fuels will be the dominant energy source in the foreseeable future and that by 2030 we will rely on fossil fuel for about 80% of our energy needs. Coal continues to be the dominant fossil fuel around the world for electric power generation [43]. Production of affordable and clean-coal energy is thus the key to secure a sustainable economic development. Towards this goal, the research community and industry have been working diligently to develop and implement various advanced technologies for improved operation efficiency/ safety/ reliability/ availability/ maintainability, enhanced fuel-flexibility and reduced (or even near-zero) emissions [44]. It has long been realized that operations of coal-based power plants must be optimized at all levels by utilizing advanced process controls. Low-cost, reliable, in situ sensors are highly demanded for advanced process control and lifecycle management in existing and future advanced power and fuel systems. The Electric Power Research Institute (EPRI) estimated that approximately $409 million can be saved annually in the existing fossil-fuel-based power generation plants in the United States by implementing advanced monitoring and control technology to achieve a 1% increase in efficiency [43].

Next generation coal power plants (e.g., the new IGCC plant) use synthesis gas (syngas) produced by coal gasification that may operate at temperatures as high as 1450 ℃. Recent studies have shown that gas turbines operating at elevated temperatures will not only increase efficiency (about 60% efficiency improvement on average), but

also reduce emissions through improvement in waste product removal and storage [4]. In addition, future coal power plants need to be fuel-flexible. Coal syngas and high-hydrogen content (HHC) fuels could vary considerably in fuel composition and heating value. The variations could lead to instabilities and excessive pressure pulsations, resulting in component fatigue, mechanical failures and costly outages and repair.

It has been estimated that more than 1000 sensors are needed in a typical power plant to ensure its correct operation [43]. These sensors share the common requirement of being able to survive and operate in the high temperature, high pressure and corrosive/erosive harsh environments for a long period of time. Among the parameters of interests, temperature and dynamic gas pressure are the two important parameters that need to be constantly monitored to ensure proper operation of the system [7]. Temperature sensors are needed throughout the entire system for in situ measurements of the flame, gas and surface temperatures at various sections. The information of dynamic pressures within a combustion turbine may be used to detect and correct instabilities before they cause serious damage [8-11].

Although power plant control systems have been constantly upgraded, improvements in sensors and instrumentation have lagged behind. The bulk of the efforts have focused on signal processing and signal conditioning, rather than the basic sensing elements and devices. Consequently, the various sensors used in today's typical power plant have remained virtually unchanged since 1970. Unfortunately, these sensors are incapable of operating directly in the locations of high temperature and high pressure harsh environments. Current sensor technologies capable of operating in harsh conditions are extremely limited. Given that clean-coal power production will be the necessity and reality for many years to come, fundamental and applied research is required to address the significant technological challenges and capability gaps in harsh environment sensors needed for monitoring existing and future power and fuel systems.

Objectives: From the previous reviews, it is concluded that optical fiber sensor is a promising candidate for high temperature harsh environment. However, the assembly based microsensors suffer from a high chance to be damaged at high temperature due to the CTE mismatch among different components. Also, there still exist a series of unsolved issues in association with optical fiber sensors in practical implementations.

The main objective of this work is to develop novel optical fiber sensors using modern laser fabrication techniques that would resolve some of the current remaining problems in optical fiber sensors for applications in harsh environments. Specifically, we will design, develop and demonstrate novel optical fiber sensors with enhanced robustness, survivability, long-term stability and functionality through assembly-free, laser based fabrication. In addition, this dissertation intends to close the gap between theoretic and experimental work and provide guidance for device design and fabrication. The specific objectives of this research include:

1) Establishment of a fundamental understanding of the refractive index change inside an optical fiber caused by CO_2 laser irradiation for guided fabrication of high performance LPFG sensors. A comprehensive analytical modeling of the LPFG is developed to understand the device physics. An automated CO_2 laser LPFG fabrication station is developed. The CO_2 laser irradiation induced refractive index in the fiber core is measured using optical interferometry and verified by real devices. The temperature response of the fabricated LPFGs is characterized. By coating LPFGs with chemical functional materials, the device is demonstrated for high temperature gas sensing.
2) Design, fabrication and demonstration of fiber inline core cladding mode interferometer (CCMI) using controlled CO_2 laser exposure method for various harsh environment sensing applications such as high temperature and ambient refractive index under extreme conditions. To justify the application potentials of this optical fiber inline device, experimental evaluation and theoretic analysis are conducted.
3) Development and demonstration of a novel, assembly-free optical fiber inline Fabry-Peort interferometer by femtosecond laser micromachining. The high temperature survivability of the device is characterized experimentally. The small temperature cross-sensitivity and the unique capability of device for highly sensitive refractive index measurement are demonstrated.

1.4. ORGANIZATION OF THE DISSERTATION

The dissertation is organized into five chapters with their contents briefly described below:

Chapter 1 provides a general introduction of optical fiber sensors with a special interest on their unique and attractive attributes toward various sensing applications in high-temperature harsh environments. A brief review of the current state-of-the-art harsh environment sensing technologies is provided. The challenges, limitations and unsolved issues are summarized. Consequently, the research objectives and the scientific/technical topics to be addressed by this dissertation are derived. After a brief description of the scope of the dissertation work, the research innovations are summarized in the context of design, development and demonstration of a number of novel, robust inline optical fiber micro-sensors uniquely fabricated by assembly-free laser fabrications.

Chapter 2 starts with a general introduction to the long period fiber grating (LPFG). A series of LPFG fabrication techniques used in the past are reviewed to reach the conclusion that the CO_2 laser irradiation method holds the promise for fabrication of high-quality LPFGs for applications under high temperature conditions without changing the geometry and decreasing the mechanical strength of the device. The operation principle is understood by a comprehensive coupled-mode theory (CMT) based model and simulation of the transmission spectrum. The transmission characteristics of LPFG are discussed based on the experimental results taken from the LPFGs fabricated using CO_2 laser irradiations. High temperature survivability is tested to justify the potential for LPFG to be used under extreme conditions. A thermal shock method is used to improve LPFG's high temperature stability. For the first time to our knowledge, an interferometric technique is employed to measure the laser induced refractive index change in an optical fiber. The measured refractive index changes are used to simulate the transmission characteristics of LPFGs and verified by the real devices fabricated by a CO_2 laser. In addition, various functional materials are coated on LPFGs to develop high-sensitivity chemical sensors.

Chapter 3 reports a new assembly-free optical fiber incline sensor fabricated by controlled CO_2 laser irradiations and operating based on the optical interference between the core and cladding modes in an optical fiber. The operation principle of such a

core-cladding mode interferometer is described and the possible configurations are presented. The previous reported fabrication techniques are reviewed and the associated challenges are discussed. A new method of using a CO_2 laser to fabricate such a device is proposed and studied experimentally. The mode excitation in the device is also discussed based on experimental results. The new device is evaluated for its capability for high temperature sensing applications.

Chapter 4 reports a novel, assembly-free, optical fiber inline Fabry-Perot interferometer (FPI) with an open cavity fabricated by femtosecond (fs) laser ablation. Starting with a brief introduction to the optical fiber FPI device, the operating principle, sensing mechanism and signal processing methods of the device are described and the common device fabrication methods are reviewed. The fs laser based fabrication method and the quality of the device are then described in details. The high temperature survivability of the fabricated FPI device is experimentally evaluated. The device is used to measure the temperature-dependent refractive index of water, demonstrating its potential for chemical sensing.

Chapter 5 summarizes the dissertation work and identifies the future work.

1.5. SUMMARY OF MAJOR INNOVATIONS/CONTRIBUTIONS

The major innovations/contributions of this dissertation include:

1) For the first time, an inteferometric method was investigated to measure the refractive index change in an optical fiber core caused by CO_2 laser exposure. The interferometry based method had shown high measurement accuracy and our measurement results confirmed that the CO_2 laser modification decreased the optical fiber core refractive index. Together with the developed device model, the measurement results provided the guidance for optimal sensor design and fabrication.
2) A novel CCMI sensor structure was successfully fabricated by controlled CO_2 laser irradiations. The device survived high-temperature tests upto 1100°C. The excited cladding modes in the CCMI structure were experimentally

determined. The device was also successfully demonstrated for refractive index measurement.

3) An optical fiber inline EFPI senor with an open cavity was successfully fabricated using femtosecond laser ablation. The assembly-free fabrication prevents the sensor from being affected from CTE mismatch caused mechanical deterioration, making it more robust for high temperature sensing applications. The sensor survived high temperatures upto 1100°C. The open-cavity FPI sensor was also successfully demonstrated for highly sensitive monitoring of ambient refractive index change. With many unique advantages such as small size, negligible temperature cross-sensitivity, and linear response toward refractive index changes, the assembly-free, open cavity FPI sensor may find many applications in chemical and biological sensing, especially under high temperature harsh environment.

2. LONG PERIOD FIBER GRATING SENSOR

This chapter starts with a general introduction to the long period fiber grating (LPFG). A series of LPFG fabrication techniques used in the past are reviewed to reach the conclusion that the CO_2 laser irradiation method holds the promise for fabrication of high-quality LPFGs for applications under high temperature conditions without changing the geometry and decreasing the mechanical strength of the device. The operation principle is understood by a comprehensive coupled-mode theory (CMT) based model and simulation of the transmission spectrum. The transmission characteristics of LPFG are discussed based on the experimental results taken from the LPFGs fabricated using CO_2 laser irradiations. High temperature survivability is tested to justify the potential for LPFG to be used under extreme conditions. A thermal shock method is used to improve LPFG's high temperature stability. For the first time to our knowledge, an interferometric technique is employed to measure the laser induced refractive index change in an optical fiber. The measured refractive index changes are used to simulate the transmission characteristics of LPFGs and verified by the real devices fabricated by a CO_2 laser. In addition, various functional materials are coated on LPFGs to develop high-sensitivity chemical sensors.

2.1. INTRODUCTION TO LONG PERIOD FIBER GRATING

2.1.1. Fiber Bragg Gratings. Fiber gratings are among the most popular optical fiber devices that have been widely used in both optical communications and optical fiber sensing. There are two general types of fiber gratings, including the fiber Bragg grating (FBG) and the long period fiber grating (LPFG). Both types of fiber gratings have a periodic perturbation of the refractive index along the fiber length. As the names suggested, an FBG has a short period that is on the scale of the optical wavelength while an LPFG has a period that is much longer than the wavelength of light.

Hill et al. in 1978 at the Canadian Communications Research Centre (CRC), Ottawa, Ont., Canada, firstly demonstrated the formation of permanent gratings in an optical fiber [45, 46]. An intense Argon-ion laser was launched into a Germania-doped

fiber and after a couple of minutes an increase in the reflected light intensity occurred which grew until almost all the light was reflected from the fiber. Spectral measurements confirmed that a very narrowband Bragg grating filter had been formed over a 1-m length of fiber. This achievement, namely "Hill gratings," was an outgrowth of research investigating in the nonlinear properties of Germania-doped silica fiber. It created an unknown photosensitivity of Germania fiber, which brought up other question into the cause of the fiber photo-induced refractivity and its dependence on the wavelength of the light which was used to the form the gratings. Detailed studies showed that the grating strength increased as the square of the light intensity, suggesting a two-photon process as the mechanism [47]. In the original experiments, laser radiation at 488 nm was reflected from the fiber end producing a standing wave pattern that formed the grating. Ten years later, Meltz et al. demonstrated that FBGs can be fabricated to reflect any wavelength by illuminating the fiber from the side of the fiber the cladding with two intersecting beams of UV light, and later UV wavelength rather than the visible radiation was found to be efficient in forming gratings on an optical fiber [48].

The index perturbation in the core is a periodic structure, similar to a volume hologram or a crystal lattice that serves as a stop-band filter. A narrow band of the incident optical field within the fiber is reflected resulted from successive, coherent scattering from the index variations. The incident wave is coupled to a counter-propagating like mode and thus reflected. The strongest interaction or mode coupling occurs at the Bragg wavelengths, described by well known Bragg condition.

$$\lambda_B = 2n_{eff}\Lambda \tag{2.1}$$

where λ_B is the Bragg wavelength, n_{eff} is the effective index of the optical fiber (fundamental mode for single mode fiber) and Λ is the grating period. Strain and temperature change may vary the modal index or grating pitch, which will change the Bragg wavelength observed from reflection or transmission spectrum.

FBG first came as a by-product of nonlinear optics research and solely a scientific curiosity at its earlier age, but soon after the first observation, FBG was quickly transforming to the basis for a technology that currently plays a significant role in optical communications and sensor systems. FBG's are now commercially available and they have found key applications in routing, filtering, control, and amplification of optical

signals in the next generation of high-capacity WDM telecommunication networks. On the other hand, FBG-based sensors appear to be useful for a variety of applications. Particularly, the area of distributed embedded sensing in materials for creating "smart structures" is of primary interest. Here, fibers with sensor arrays are embedded into the materials to allow measurement of parameters such as load, strain, temperature, and vibration, from which the health of the structure can be assessed and monitored in real-time. It is worth noting that, intrinsically, FBG is solely sensitive to temperature and strain. However, by implementing transducers that can transfer other parameter to temperature or strain, one can break the restriction. It was reported that FBG can also prove to be useful as the optical sensing element in a range of other fiber sensor configurations; grating-based chemical sensors, pressure sensors, and accelerometers are examples [49].

2.1.2. Long Period Fiber Bragg Grating. In 1990, Hill et al., the same group who developed the FBG, demonstrated that by inscribing grating point-by-point through the side of the fiber using a UV laser source with controlled long period. Efficient mode conversion between forward propagating modes in a multimode fiber is demonstrated. The wavelength at which conversion occurs is determined by the periodicity of the grating. Then, the grating can be designed to couple light at any wavelength of interest by tuning the period. In 1995, Vengsarkar et al. were inspired by the propagating mode conversion gratings and introduced a new type of fiber grating device to the optics community, the long period fiber Bragg grating [50].

Long period fiber grating (LPFG), has a periodically modulated core refractive along a single mode optical fiber. As illustrated in Figure 2.1, the LPFG promotes coupling between the propagating core mode and co-propagating cladding modes. The high attenuation of the cladding modes results in the transmission spectrum of the fiber containing a series of attenuation bands located at discrete wavelengths, and each attenuation band corresponds to the coupling to a different cladding mode. The transmission spectrum of a typical LPFG is shown in Figure 2.2. The centre wavelengths of the attenuation bands, are sensitive to the period of the LFPG, the length of the LPFG (typically of the order of 30 mm) and to the local environment: temperature, strain, bend

radius and to the refractive index of the medium surrounding the fiber. Changes in these parameters can modify the period of the LPFG and/or the differential refractive index of the core and cladding modes. This then modifies the phase matching conditions for coupling to the cladding modes, and results in a change in the central wavelengths of the attenuation bands [51].

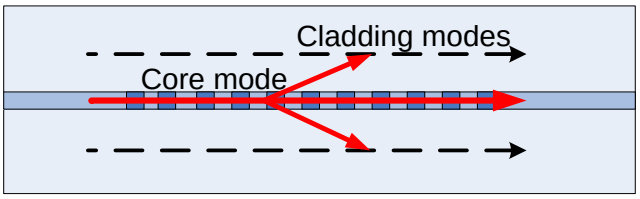

Figure 2.1 Schematic of LPFG operating mechanism

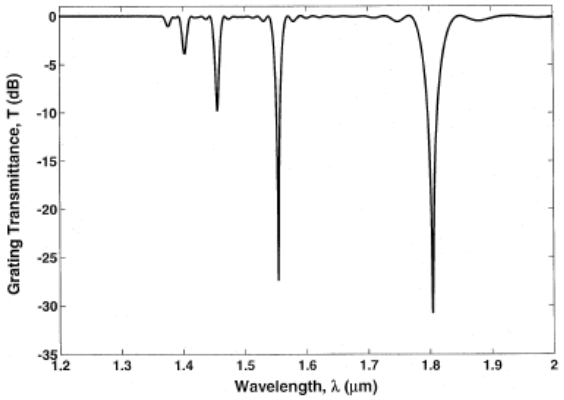

Figure 2.2 Transmission spectrum of a typical LPFG

The sensitivity to a particular measurand is dependent upon the core cladding refractive index contrast as well as the core cladding dimension of the optical fiber and upon the order of the cladding mode to which the optical power is promoted. Therefore, different cladding modes have different sensitivity, which will be discussed in detail. The responses to ambient environment makes them particularly attractive for sensor applications, with the prospect for multi-parameter sensing using a single sensor element [52].

Both active and passive LPFG-based devices have been reported in the literature, of which, besides communication applications, a small representative number for the interest of optical sensing applications are mentioned here. The high sensitivity of cladding modes to surrounding refractive index values makes LPFGs suitable for chemical sensing such as gas concentration or environmental measurements [53-60]. Meanwhile, since bending, stress, torsion and temperature can affect on LPFGs, physically change the system and cause a resonant wavelength shift correspondingly, it has been widely reported that LPFGs can be used for bending, stress, torsion and temperature sensing [51, 54, 61-63]. All these sensing applications are unique because the all-glass structure helps these devices survive extreme conditions such as corrosion and high temperature (1200 ℃) [27, 64, 65].

2.2. LPFG FABRICATION TECHNIQUES

2.2.1. LPFG Fabrication Review. A number of techniques have been developed for fabricating LPFGs in addition to exposing photosensitive optical fibers to UV light. Electric arc discharge and focused infrared femtosecond (fs) laser pulses have both been used to write LFPGs on a point-by-point basis.[66] Both of the two methods can achieve a permanent density variation on optical fiber which helps create a permanent modification of the refractive index of the core periodically [67-69]. LPFGs have also been created by ion implantation (bombardment) through a metal amplitude mask. Though a graded mask, ion implantation of silica glass increases the refractive index of optical fiber in a periodic pattern achieving LPFGs [70]. Hollow-core optical fiber filled with a liquid crystal solution can be periodically poled (spatially) by applying voltage to electrodes to create an LPFG structure [71]. Pressing on an optical fiber with a grooved plate is another method by which an LPFG can be temporarily created. This is based on the physical deformation on optical fiber which also changes the refractive index of the fiber core [72, 73]. Most recently, the CO_2 laser irradiation methods have been developed [64, 65]. The localized rapid heating and subsequent cooling of the optical fiber results in the stress relief-induced refractive index changes inside the fiber core.

Although the conventional UV inscription method is a very mature method to fabricate LPFG and both mask and point-by-point exposure techniques have been demonstrated in previous publication, the grating fabricated using such method cannot survive at an elevated temperature. As the temperature goes beyond room temperature, the UV written grating in an optical fiber starts to fade and eventually loses the modal coupling. Among the LPFG fabrication technique, fs laser, CO_2 laser irradiation and electric discharge are able to help the gratings survive a temperature up to 1000 ℃. However, fs lasers are generally very expensive to operate. Electric discharge may significant affect optical fibers' mechanical strength. Therefore, at the early stage, this research started to investigate the LPFG fabrication based on CO_2 laser exposure induced refractive index changes inside an optical fiber [74].

2.2.2. Using CO_2 Laser to Fabricate LPFG. Figures 2.3 and 2.4 show the schematic and photograph of the CO_2 laser based LPFG fabrication system, respectively. The LPFG inscription method used is similar to that described in the references [64, 65]. As shown in Fig. 2.3, a CO_2 laser (SYNRAD, Inc.) with a free space wavelength of 10.6 μm and a maximum output power of 20 W was used in the system. A ZnSe cylindrical lens with a focal length of 50 mm was used to shape the CO_2 laser beam into a narrow line with a linewidth of 220 μm. The CO_2 laser is controlled by the computer through the laser controller to produce a desired power.

The optical fiber (Corning SMF-28) with its buffer stripped is placed on a one axis motorized translation stage (Newport PM500, resolution 500 nm, dynamic range 100 mm) controlled by a computer, providing the option of displacing the translation stage in unison so that the fiber can be precisely moved to the center of the laser beam. The focused laser beam was transversely loaded onto the single mode optical fiber. Controlled by a computer, the translation stage moves the fiber at fixed step for laser exposure, resulting in a periodic refractive index modulation in the fiber core. The output power and exposure time-trajectory of the CO_2 laser could be accurately adjusted by a laser controller through computer software. A microscope video camera was used to visualize the micro-displacement of the optical fiber while the fabrication process is activated.

During grating fabrication, a tunable laser (HP 81642A) and an optical power meter (HP 81618A) were also used to monitor the grating transmission spectrum. As shown in Fig. 2.4, the tunable laser is coupled into one end of the fiber and the other end is connected to the power meter. The tunable laser was controlled by the computer to step from 1510 to 1640 nm and the transmitted power after the grating was detected by the optical power meter so that the LPFG spectrum could be recorded in real-time during its fabrication.

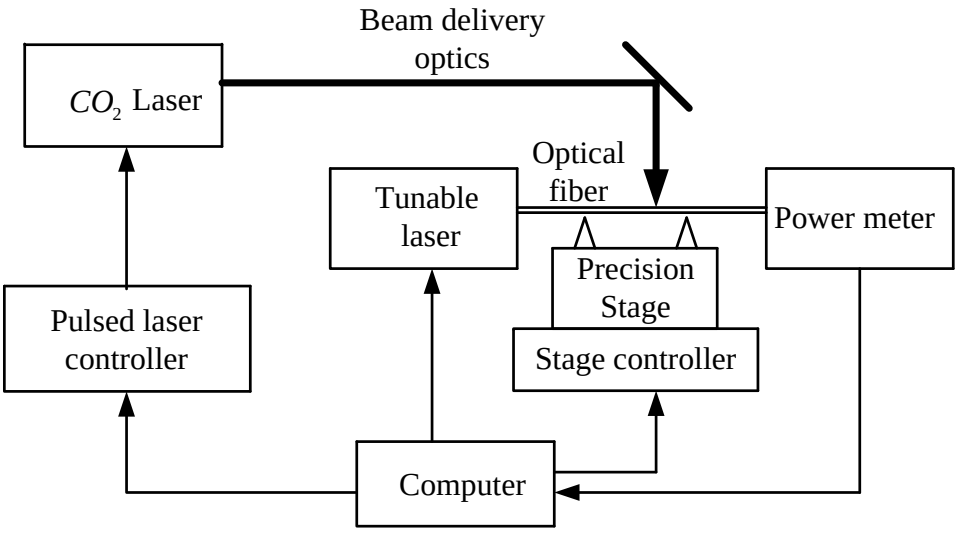

Figure 2.3 Schematic setup of the CO_2 laser based LPFG fabrication system

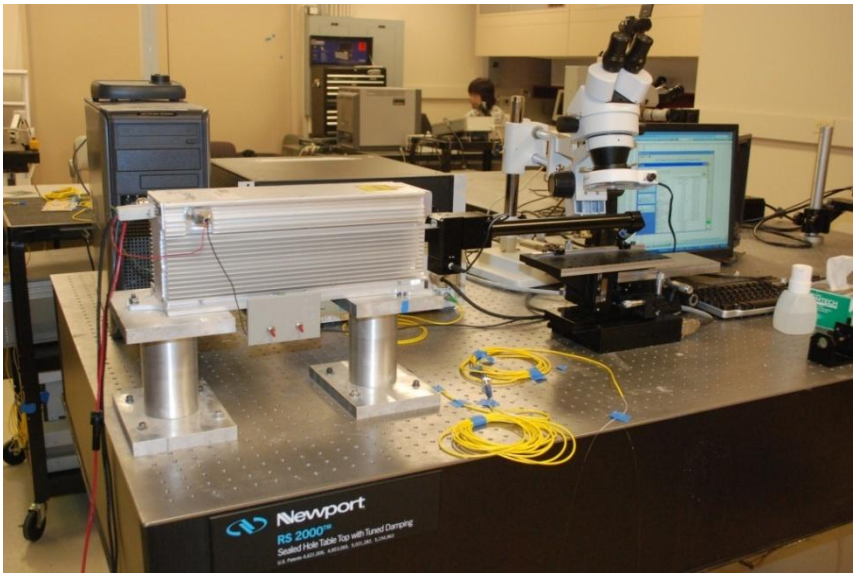

Figure 2.4 Photograph of LPFG fabrication system

2.3. LPFG THEORY AND SIMULATION

An LPFG is formed typically by inducing a periodic refractive index modulation in the fiber core. The resulting transmission spectrum consists of distinct resonant loss bands that are due to the coupling of the fundamental core mode to the forward propagating cladding modes. Because in a SMF, cladding modes are not designed to guide light waves, energy guided by these modes will quickly dies out along propagation, resulting in the loss bands in the transmission spectrum. It is well known that the resonance wavelength of an LPFG with period can be approximated by the phase matching condition or Bragg condition: [50]

$$\lambda_{res} = (n_{co}^{eff} - n_{cl,m}^{eff})\Lambda \tag{2.2}$$

where Λ is the grating period, λ_{res} is the resonant wavelength, n^{eff}_{co} and $n^{eff}_{cl,m}$ are the effective indices of the fundamental core mode and the m^{th} cladding mode, respectively. Although the Bragg condition of FBG and LPFG look very similar from formulation, the analytical modeling of LPFG is a lot more complicated than that of FBG. For the reason that cladding modes in a SMF has a huge number, LPFG operation mechanism is very different from the FBG case, where forward propagation core mode energy exclusively couples into the backward propagation mode.

In an LPFG, light energy can be coupled from the fundamental core mode to various forward propagating cladding modes, depending on the coupling conditions. Therefore, intuitively speaking, the coupling process is more like a competition among different cladding modes. In addition, the coupling between different forward propagation cladding modes make the modeling more complex. Eventually, at certain wavelength, one cladding mode would dominantly receive power from the core mode (when the phase matching condition fits well), determined by the length of period, number of grating points (total length of LPFG), depth of modulation, and the optical fiber waveguide properties including its core/cladding dimension and the refractive index of the glass material.

2.3.1. Cladding LP Modes. To establish the analytical model of LPFG, the definition and calculation of different LP modes is firstly visited. Snyder considered the LP modes simply to be plane waves by letting E and H field on propagation direction equal to zero [75]. This definition is very simple and accessible to physical interpretation in a weakly guided SMF structure [76]. The LP modes of a cylindrical dielectric waveguide having an arbitrary refractive index profile on the cross section of an optical fiber are described. Here, for the simplicity, we assume that the modes we are dealing with in the LPFG modeling are azimuthally uniform. According to the LP mode formulation, an LP_{vj} mode of order j and within a cylindrical dielectric layer i having radius $r_{i-1} < r < r_i$ and refractive index n_i shown in Figure 2.5, has transverse electric field components propagating along the fiber axis given by: [77, 78]

$$\begin{aligned} U_{vj,i}(r,\phi,z) &= e^{-j\beta_{vj}z}\Psi_{vj,i}(r,\phi) = e^{-j\beta_{vj}z}\Phi_v(\phi)R_{vj,i}(r) \\ &= e^{-j\beta_{vj}z} \times \begin{cases} A_{vj,i}J_v(r\gamma_{vj,i}) + B_{vj,i}Y_v(r\gamma_{vj,i}) & when \quad \beta_{vj} < k_0 n_i \\ A_{vj,i}I_v(r\gamma_{vj,i}) + B_{vj,i}K_v(r\gamma_{vj,i}) & when \quad \beta_{vj} > k_0 n_i \end{cases} \end{aligned} \tag{2.3}$$

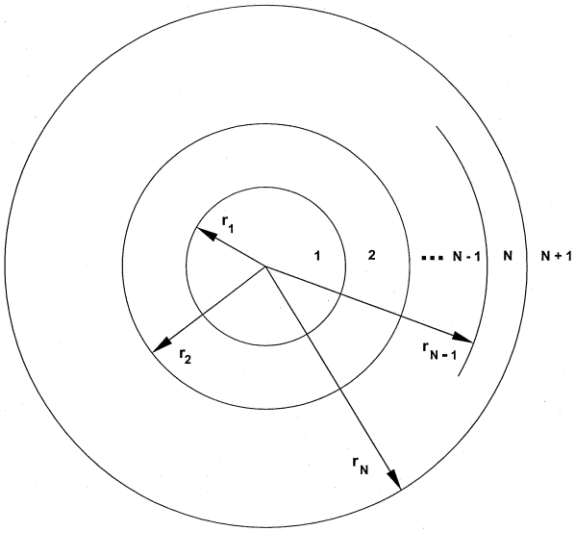

Figure 2.5 Cylindrical fiber waveguide with multilayer structure

where $k_0 = 2\pi/\lambda$ is free space wavenumber, β_{vj} is the longitudinal propagation constant of the LP_{vj} mode, $\gamma_{vj,i} = (|k_0^2 n_i^2 - \beta_{vj}^2|)^{1/2}$ is the magnitude of the transverse wavenumber. ϕ is

the azimuthal angle, and $A_{vj,I}$ and $B_{vj,I}$ are field expansion coefficients determined by the boundary conditions within the cylindrical layer *i*. $J_v(r\gamma_{vj,i})$ and $Y_v(r\gamma_{vj,i})$ are the ordinary Bessel functions of the first and second kind of order *v*, while $I_v(r\gamma_{vj,i})$ and $K_v(r\gamma_{vj,i})$ are the modified Bessel functions of the first and second kind of order *v*, generally being a nonnegative integer number. The transfer matrix method is applied to find the propagation constant of LP modes for optical fibers [29].

2.3.2. Refractive Index Modulation. LPFGs in our lab are formed by exposing a single mode optical fiber to periodic CO_2 laser irradiations, which change the fiber refractive index in the exposed areas as a result of the localized laser heating. LPFGs can be fabricated either with or without applying a longitudinal tension (i.e. external load). For LPFGs fabricated without tension, the change in physical length of the fiber does not vary after laser irradiations. For LPFGs fabricated with a small tension within a short exposure time, the fiber physical elongation is very small. In this paper, we mainly focus on the gratings fabricated with a low laser power and without applying tension in which the fiber length change is negligible. Under these assumptions, the change in optical length is mainly caused by the laser irradiation induced refractive index change inside the fiber core. With a low laser irradiation power, the laser irradiation produces a Gaussian-shaped index perturbation profile along the axial direction (z) of the optical fiber [79].

As shown in Figure 2.6, the shaded areas represent the portions exposed to CO_2 laser beam with a Gaussian-shaped intensity distribution. The refractive modulation function can be written as:

$$\Delta n = \Delta n_{\max} \exp\left(-\frac{2z^2}{W_0^{\,2}}\right) \tag{2.4}$$

where Δn_{max} is the peak refractive index change in the core at the position corresponding to the center of the laser beam; W_0 is the Gaussian beam radius, at which the amplitude of refractive index perturbation decreases to $1/e^2$ or (13.5%) of its maximum value. Based

on this definition, the full width at half-maximum (FWHM) of the index perturbation, W_{FWHM}, is given by:

$$W_{FWHM} = \sqrt{2\ln 2} \cdot W_0 \tag{2.5}$$

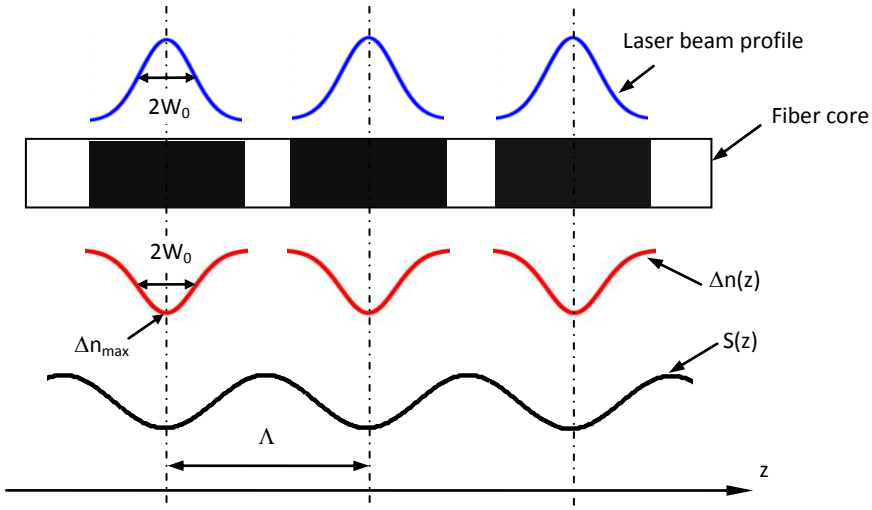

Figure 2.6 Periodic CO_2 laser irradiation induced refractive index modulation in an optical fiber (W_0 is the Gaussian beam radius of the laser.).

Assuming that the period of laser exposures is Λ, the axial refractive index modulation function S(z) can be approximated by the first two terms of Fourier series of the periodic Gaussian-shaped perturbation in LPFG modeling [29]. Using the first two terms of Fourier series will dramatically reduce the amount of computation in simulation. However, this approximation practically uses a sinusoidal function to approximate the periodic index perturbation, which may introduce error in the LPFG simulation. Under this approximation, the index modulation function is given by:

$$\Delta n(z) \approx S(z) = s_0 + s_1 \cos\left(\frac{2\pi}{\Lambda} z\right) \tag{2.6}$$

where s_0 and s_1 are the coefficients of the first two terms of the Fourier series, respectively, given by

$$s_0 = \Delta n_{\max} \frac{1}{\Lambda} \int_{-\Lambda/2}^{\Lambda/2} \exp\left(-\frac{2z^2}{W_0^2}\right) dz \tag{2.7}$$

$$s_1 = \Delta n_{\max} \frac{2}{\Lambda} \int_{-\Lambda/2}^{\Lambda/2} \exp\left(-\frac{2z^2}{W_0^2}\right) \cos\left(\frac{2\pi}{\Lambda} z\right) dz \tag{2.8}$$

According to reference [29], the transmission characteristics of an LPFG can be determined once we know the fiber parameters, modulation function S(z), the period and the grating length (or the number of irradiation points). In Eqs. (7) and (8), W_0 can be measured using a laser beam profiler, and the period Λ is a variable to be controlled during grating fabrication. The only unknown to be measured is the peak refractive index change Δn_{max}. In the following section, we proposed a novel method based on interference tracking to measure the laser induced refractive index change in an optical fiber or in another word, Δn_{max}.

2.3.3. Coupled-Mode Theory. The interaction among the LP modes in the fiber can be modeled through coupled-mode theory (CMT). According to the CMT the interaction (coupling) between optical modes is proportional to their coupling coefficient *K*. Assuming that each forward propagating mode (core and cladding) can be expressed with a complex form A(z) and by neglecting any backward propagating waves, the generalized coupled-mode equations governing the interaction of co-propagating modes are: [80, 81]

$$\frac{dA_{\mu k}(z)}{dz} = -j \sum_{vj=01}^{M} [K_{vj,\mu k}^{t} + K_{vj,\mu k}^{z}] A_{vj}(z) e^{-j(\beta_{vj} - \beta_{\mu k})z} \qquad for\ \mu k = 01,...M \tag{2.9}$$

With the assumption of LP mode analysis, the coupling coefficient $K^{z}_{vj,\mu k}$ on propagation direction between the LP_{vj} and the $LP_{\mu k}$ mode goes to zero. Then, $K_{vj,\mu k}$ will be used to substitute $K^{t}_{vj,\mu k}$ and this coupling coefficient can be derived by integrating the different mode fields over the whole fiber cross-section: [29]

$$K_{vj,\mu k} = [s_0 + s_1 \cos(\frac{2\pi}{\Lambda} z)]\zeta_{vj,\mu k} \tag{2.10}$$

where s_0 and s_1 represent the dc and ac component of refractive index perturbation and $\varsigma_{vj,\mu k}$ is the term describing the field overlapping within the entire fiber cross-section region between the LP_{vj} and the $LP_{\mu k}$ modes, given by:

$$\varsigma_{vj,\mu k} = \frac{\omega \varepsilon_0}{2P_0} \sum_{i=1}^{N} n_0(r_i) \int_{r=r_{i-1}}^{r_i} R_{vj}(r) R_{\mu k}(r) r dr \tag{2.11}$$

where ω is the radial frequency of the light wave, ε_0 is the permittivity of free space, P_0 is the normalized power in LP_{vj} mode, n_0 is the refractive index of the fiber glass, N is the number of layers in the optical fiber structure, and $R_{vj}(r)$ and $R_{\mu k}(r)$ are the radial component of electrical field in the LP_{vj} and the $LP_{\mu k}$ modes, respectively. For an LPFG sitting in the air, we only need to deal with 2 layers, since the cladding diameter is much larger than the core diameter, making the outer diameter of optical fiber infinity with regard to the position of the boundary between core and cladding. It is also worth noting that, in this case, n_0 is a step function along the radius r, where it is slightly higher in the core area.

2.3.4. Coupled Differential Equation. Substituting Eqs. (2.10) and (2.11) into (2.9) and neglecting rapidly oscillating terms by applying common synchronous approximation, the coupled-differential- equation (DE) system with dimension $M \times M$ is formed, shown in Eq. (2.12).

$$\frac{dA_{\mu k}(z)}{dz} = -j \sum_{vj=01}^{M} \begin{Bmatrix} s_0 \zeta_{vj,\mu k} A_{vj}(z) & if\ \mu k = vj \\ \frac{s_1}{2} \zeta_{vj,\mu k} A_{vj}(z) e^{-j(\beta_{vj} - \beta_{\mu k} \pm \frac{2\pi}{\Lambda}) z} & otherwise \end{Bmatrix} \quad for\ \mu k = 01, ...M \tag{2.12}$$

We further define,

$$Q_{vj} = -js_0\zeta_{vj,vj}$$
$$V_{vj,\mu k} = -j\frac{s_1}{2}\zeta_{vj,\mu k} \times e^{[-j(\beta vj - \beta vj \pm \frac{2\pi}{\Lambda})z]} \tag{2.13}$$

The Q_{vj} terms correspond to self-coupling coefficients, the $V_{vj,\mu k}$ terms correspond to the cross-coupling coefficients between different LP modes. Then, the M × M coupled-DE system can be written as,

$$\begin{bmatrix} A_{01}(z) \\ A_{02}(z) \\ A_{03}(z) \\ \vdots \\ A_M(z) \end{bmatrix}_{z=0} = \begin{bmatrix} Q_{01} & V_{01,02} & V_{01,03} & \cdots & V_{01,M} \\ V_{02,01} & Q_{02} & V_{01,02} & \cdots & \vdots \\ V_{03,01} & V_{01,02} & Q_{03} & \cdots & \vdots \\ \vdots & \vdots & \vdots & \ddots & V_{M-1,M} \\ V_{M,01} & \cdots & \cdots & V_{M,M-1} & Q_M \end{bmatrix} \begin{bmatrix} A_{01}(z) \\ A_{02}(z) \\ A_{03}(z) \\ A_{04}(z) \\ A_{05}(z) \end{bmatrix} \tag{2.14}$$

With initial condition A_{01} (z=0) = 1 and A_{vj} (z=0) = 0 for *vj* = 02, …M, one can calculate the electrical field of one wavelength for each mode at certain grating length by solving this coupled differential equation set. In this work, the M is chosen to be nine, for the reason that only the modes with low order have substantial fields and in application, we are more interested in coupled cladding mode less than tenth order.

2.4. LPFG CHARACTERISTICS

2.4.1. Typical Transmission Spectrum of LPFG. The transmission. characteristics can be measured by sweeping a tunable laser source as shown in Figure 2.3. The tunable laser served as the light source at one end of the fiber and at the other end an optical power meter was used to detect the power transmitted through the grating. The wavelength stepping of the laser and the power detection of the power meter were coordinated by a computer. The typical transmission spectrum of the fabricated LPFG with a period of 535 μm and a resonance peak corresponding to LP_{05} cladding mode coupling is shown in Figure 2.7. The curve with black square dots is the resonance peak corresponding to the energy coupling from the fundamental core mode to the fifth cladding mode, The spectrum indicated a low insertion or background loss (~1 dB), a narrow Full-Width-at-Half-Maximum (FWHM ~7 nm) and a high resonance strength (>20 dB) of the fabricated LPFG.

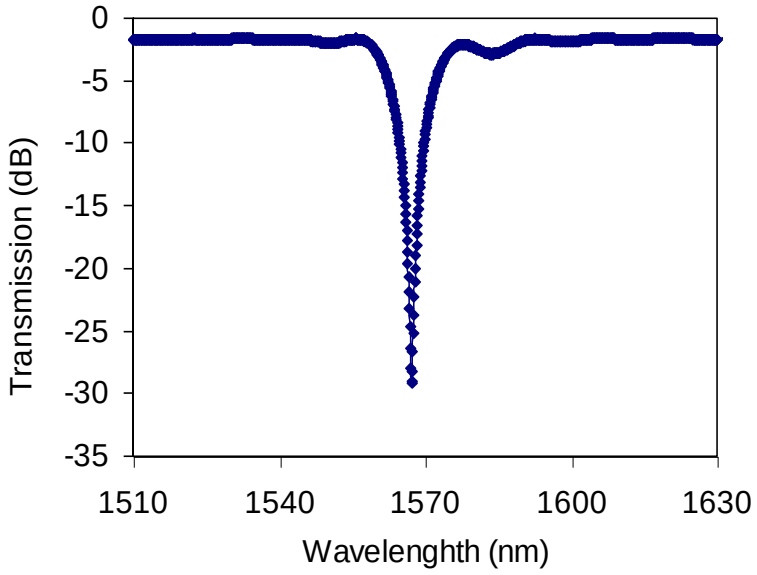

Figure 2.7 Measured transmission spectra of a LPFG with cladding mode LP_{05} resonance

2.4.2. Transmission Spectra with Different Periods. As shown in Fig. 2.8, by varying the grating period from 505 to 545 μm, it is possible to effectively change the resonant wavelength of the LPFG from 1520 to 1640 nm, which was is the tuning range of the tunable laser in a communication wavelength regime. It is possible to further expand the resonance wavelength beyond the 1520 to 1640 nm range. According to Eq. 2.2, since the effective refractive indices for both core mode and cladding modes are fixed after fabrication, the resonant wavelength is linearly proportional to the grating period. This linear relation was confirmed by the experiments as shown in Fig. 2.9.

2.4.3. Transmission Spectra with Different Cladding Mode Resonances. For the reason that the observation bandwidth is very limited in communication range, it is generally not possible to see more than two resonant modes in one scan. By further tuning the period length to a smaller value, the higher order mode resonances can be obtained in the transmission spectrum, shown in the Figure 2.10, where the period length for LP_{06}, LP_{07}, LP_{08} and LP_{09} are 440 μm, 375 μm, 315 μm and 268 μm, respectively.

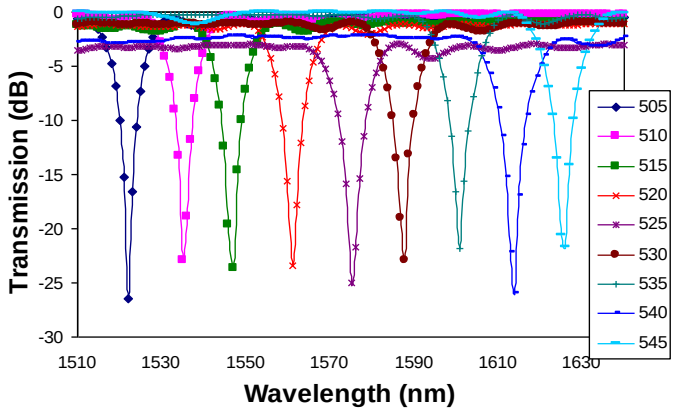

Figure 2.8 LPFG transmission spectra with different periods

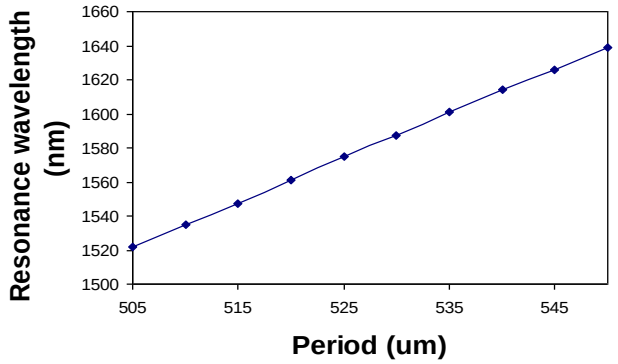

Figure 2.9 Resonant wavelengths as a function of period

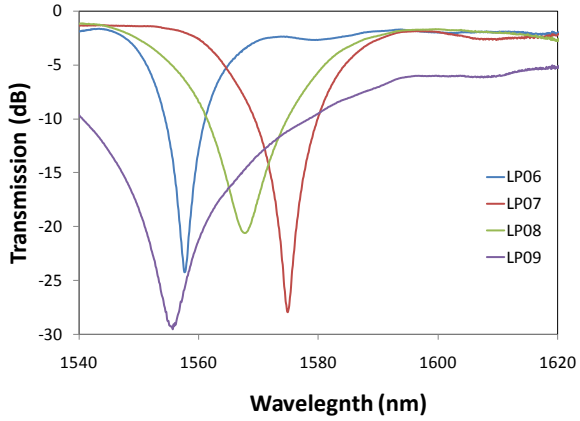

Figure 2.10 Transmission spectra for LP_{06}, LP_{07}, LP_{08} and LP_{09} cladding mode resonances

2.5. MEASUREMENT OF REFRACTIVE INDEX CHANGE IN OPTICAL FIBER INDUCED BY CO_2 LASER IRRADIATION

2.5.1. Importance of Measuring the Refractive Index Modulation. The amount of refractive index modulation inside a fiber core is one of the most critical variables that determine the transmission characteristic of an LPFG. Accurate knowledge of the CO_2 laser irradiation caused refractive index changes can thus help us adjust the CO_2 laser parameters such as the power and pulse duration during LPFG fabrication to achieve desired performance. Modeling of the fabricated LPFG predicted that the magnitude of refractive index change caused by CO_2 laser exposure was at a scale of 10^{-4} [29, 80]. Due to the very small change, direct measurement of the refractive index modulation with a high accuracy has been a great challenge. The process of using a CO_2 laser to fabricate LPFGs still remains in the trail-and-error stage.

During the drawing process, residual stress is developed inside the fiber as a result of radial variations of the thermal expansion and viscoelastic properties. The refractive index of an optical fiber thus depends on the amount and distribution of the residual stress [82, 83]. The CO_2 laser irradiation induced refractive index change on an optical fiber has been explained as a result of development or relation of residual stress inside a fiber caused by the localized thermo shocks [84, 85]. Using a modified polariscope, Kim et al. measured the residual axial stress in the fiber core caused by CO_2 laser irradiation [79]. It was found that the refractive index of fiber core decreased as a result of residual stress relaxation. Based on the photoelastic effects [86], the laser irradiation induced refractive index change was estimated using the axial stress data only. At a low irradiation power, the net core stress distribution along the fiber axis was a well fitted Gaussian function with its width smaller than the laser beam diameter. At high irradiation power, the net core stress distribution was flat (i.e. saturated) in the center of the fiber core. The polariscope technique has also been used to measure the Arc-induced axial stress modulation [87]. It was found that residual stress relaxation might not be the only major cause of refractive index modulation during the grating formation.

Kim el al. used a Mach-Zehnder interferometer constructed by an LPFG pair to measure the CO_2 laser induced refractive change [88]. In the reported approach, two LPFGs were separated by a section of fiber with a length of about 15 cm. The first LPFG

coupled part of the light energy into the cladding mode while the rest remained inside the fiber core. After passing the middle section, the cladding and core modes were recoupled and mixed at the second LPFG, resulting in interference fringes inside the transmission spectrum of the grating. The phase of the interference signal was proportional to the optical path difference (OPD) between the cladding and core modes. By monitoring the spectral shift of the interference fringe, it was found that the laser irradiation induced refractive index change was negative and in the range from -8.0×10^{-5} to -2.1×10^{-4}, depending on the fiber type, laser power, as well as the applied tension. The reported method measured the change in index contrast between the fiber core and cladding in the fiber sections exposed to CO_2 laser irradiations, not the refractive index difference between the modified and unmodified fiber sections, whereas the later attributes to LPFG formation. In order to generate a detectable amount of change in OPD, the reported method used a CO_2 beam of large diameter (7.2 mm) to modify a large fiber section between the two LPFGs. In addition, the long exposure time (5 minutes) also produced a significant amount of fiber elongation (~100 μm). These measurement conditions were substantially different from those used for LPFG fabrications. As a result, the measurement results cannot be directly used for LPFG modeling and design.

So far, measurement of refractive index change in optical fibers has mainly focused on clarification of the grating formation mechanisms. From the grating design and fabrication perspectives, it will be very useful to correlate the measured refractive index change with the writing parameters through a detailed comparison of experimental data with simulated data.

In this section, we report a new method to measure the CO_2 laser irradiation-induced refractive index changes inside the fiber core with various laser pulse durations for the purpose of design and fabrication of LPFG. The measurement was performed using a simple fiber Fabry-Perot interferometer. The measured refractive index modulations were used to simulate the LPFG transmission spectra. The tension free point-to-point laser exposure used in our lab to fabricate LPFGs is considered in refractive index measurements.

2.5.2. Index Modulation Measurement Using an Interferometer. As articulated in the modeling part, the amount of refractive index modulation inside a fiber core is converted to the peak refractive index change Δn_{max}, which can be measured using a fiber Fabry-Perot interferometer as schematically shown in Fig. 2.11. The light from a tunable laser is directed into a fiber segment through a 3 dB fiber coupler. With both ends cleaved, the fiber piece operates as a Fabry-Perot interferometer in which the reflections at the two endfaces, coupling back through the lead-in fiber and counter propagating through the 3 dB coupler, superimposed to form an interference signal at the optical power meter. By stepping the tunable laser through its available wavelength range and coordinating the signal detection at the power meter using a computer, the interference spectrum of the Fabry-Perot interferometer can be recorded. When exposed to CO_2 laser irradiations, the fiber segment changes its refractive index, resulting in a phase shift in the interference signal. The CO_2 laser induced fiber refractive index change can thus be calculated based on the amount of phase shift after laser irradiation.

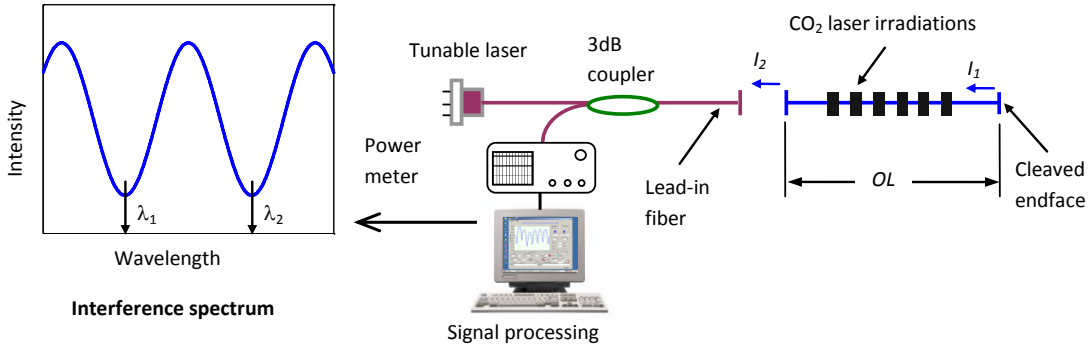

Figure 2.11 Fiber Fabry-Perot interferometer for measurement of refractive index modulation

Assuming that the two reflections from the cleaved fiber segment endfaces have the intensities of I_1 and I_2, respectively, the interference signal I generated by these two reflections is given by [89]:

$$I = I_1 + I_2 + 2\sqrt{I_1 I_2}\cos\left(\frac{4\pi}{\lambda}(OL) + \phi_0\right), \tag{2.15}$$

where OL is the optical length of the fiber segment, defined as the product of the length and the refractive index of the fiber core; ϕ_0 is the initial phase of the interference; λ is the optical wavelength in vacuum.

As shown in Fig. 2.11, the two adjacent valleys at λ_1 and λ_2 in the interference spectrum have a phase difference of 2π, that is:

$$\left(\frac{4\pi}{\lambda_1}OL\right) - \left(\frac{4\pi}{\lambda_2}OL\right) = 2\pi. \tag{2.16}$$

Therefore, the initial optical length of the fiber segment can be calculated using the following equation:

$$OL = \frac{\lambda_1\lambda_2}{2(\lambda_1 - \lambda_2)}. \tag{2.17}$$

Under the assumptions of a low laser power and no axial tension on the fiber during laser irradiation, the change in optical length is mainly caused by the laser irradiation induced refractive index change inside the fiber core. Based on the Gaussian-shaped refractive index perturbation profile as denoted in Eq. (2.4), the single laser irradiation induced change in optical refractive index (ΔOL_{single}) can be found by integrating over the entire exposure section, which is given by:

$$\Delta OL_{\text{single}} = \int_{-\infty}^{+\infty} \Delta n_{\max} \exp\left(-\frac{2z^2}{{W_0}^2}\right) dz = \Delta n_{\max} W_0 \sqrt{\frac{\pi}{2}}. \tag{2.18}$$

For multiple-point laser irradiations (with the same laser conditions) at different locations, the accumulated change in optical length (ΔOL) along the fiber section is

$$\Delta OL = m \cdot (\Delta OL_{\text{single}}) = \left(\Delta n_{\max} W_0 \sqrt{\frac{\pi}{2}} \right) m \quad , \tag{2.19}$$

where m is the total number of laser irradiations.

When the amount of optical length change is small so that the phase shift is less than 2π, the phase ambiguity issue can be avoided. The relative optical length change can be calculated based on the spectral shift of the interferogram at the featured points such as the peak, valley and the center of the interference fringes, given by [90]

$$\Delta OL = \frac{\Delta \lambda_1}{\lambda_1} OL \quad , \tag{2.20}$$

where λ_1 and $\Delta\lambda_1$ are the wavelength and the shift of wavelength at the corresponding feature point, respectively.

Combining Eqs. (2.18) and (2.19), one finds the peak refractive index change, given by

$$\Delta n_{\max} = \frac{1}{m W_0 \sqrt{\pi / 2}} \frac{\Delta \lambda_1}{\lambda_1} OL \quad . \tag{2.21}$$

An alternative way of calculating the peak refractive index change is directly based on Eq. (2.19) in which the change in optical length is a linear function of the number of laser exposures and the slope of the line is linearly proportional to Δn_{max}. Experimentally, one can measure the optical length change after a various number of laser exposures and curve-fit the measurement results into a line. The slope of the fitted line can thus be used to calculate Δn_{max}. This method uses multiple data points in calculation and effectively reduces the measurement uncertainty.

Once Δn_{max} is determined, the refractive index modulation coefficients (s_0 and s_1) can be calculated according to Eqs. (2.7) and (2.8), and the LPFG transmission spectrum can be determined by computer simulation.

2.5.3. Index Measurement Experiment. A fiber Fabry-Perot interferometer was constructed according to Fig. 2.11. The fiber used in the experiment was Corning SMF-28e single mode fiber. A small segment of fiber with a length of about 20 mm was prepared by cleaving both sides and cleaned carefully in an ultrasonic acetone bath. The fiber sample was mounted on the 3D translation stage for laser exposures. The lead-in fiber was brought in to a very close distance (~2 μm) to the fiber segment. After careful alignment, the interference spectrum of the fiber segment was taken by scanning the tunable laser with a resolution of 1 pm per step. The fiber segment was exposed to CO_2 laser irradiation and the distance from the laser to the fiber segment was kept to be the same as that in the grating fabrication. After one laser irradiation, the stage moved the fiber segment along the fiber axial direction for another exposure in a new location. The axial separation between two adjacent exposure locations was varied randomly from 500 to 600 μm to avoid grating effects in the interference spectrum. For each fiber sample used in experiments, an initial spectrum was taken before laser irradiation and a spectrum was recorded after every eight laser exposures. The reason of recording the spectrum after every eight laser exposures was to allow enough phase shift accumulation within the 2π unambiguity limit. The length of the fiber segment (~20 mm) allowed a total of 24 laser exposures to leave a few millimeter unmodified length for fiber positioning. Therefore, 4 interference spectra were recorded on each fiber sample. Increasing the length of the fiber segment will allow more measurement points. However, a long fiber segment results in dense interference spectrum, requiring a high spectral resolution in spectrum acquisition. The spectral resolution of our system was limited by the step size (1 pm) of the tunable laser.

The laser power was set to a constant value of 8 W for all experiments but the laser exposure time was varied from 50 ms to 125 ms to investigate the possibility of controlling the laser-induced refractive index changes. The initial optical length (OL) of the fiber segment was calculated using Eq. (2.17). The changes in optical length were

calculated using Eq. (2.20) and the peak refractive index change (Δn_{max}) was determined based on the slope of the line-fitted measurement data.

2.5.4. Index Measurement and LPFG Modeling. Modeling of the LPFG mainly followed the methods and procedures in the previous section, where the coupled-mode theory was applied to treating the interaction between the fundamental core mode to various cladding LP modes, and the transfer matrix method was used in the calculations. It has been pointed out that gratings produced by CO_2 laser irradiation may have non-uniform azimuthal refractive index profile in the cross section of a fiber. Again, the modeling work in this paper only considered an LPFG with uniform azimuthal refractive index profile for simplicity. Here we highlight the major steps. First, the propagation constants (β) and the amplitude coefficients of the fundamental core mode (LP_{01}) and the cladding modes up to the tenth order (LP_{02}, $LP_{03, \ldots}$, LP_{10}) were calculated in the wavelength range from 1510 to 1640 nm. Second, the dc and ac modulation coefficients s_0 and s_1 in Eqs. (2.7) and (2.8) were calculated based on the measured Δn_{max}. The coupling coefficients of these modes were computed correspondingly. Third, the optical powers of the modes were computed in the wavelength range using the transfer matrix formed based on the coupled model equations. Finally, the transmission spectrum of the grating was calculated and plotted.

2.5.5. Results and Discussions. Fig. 2.12(a) shows the initial interference spectrum and those after 8, 16, and 24 points laser irradiations with the laser power of 8 W and exposure time of 125 ms. Under these laser parameters, no obvious fiber deformation was observed under the optical microscope. The large fringe visibility indicated high-quality of the interference signals. Since each laser exposure induced a small amount of power loss, the fringe visibility of the interference signal reduced as the number of laser exposures increased. The loss can be attributed to the micro distortion of the fiber caused by CO_2 laser irradiation. The micro distortion induced loss also accounts for the insertion loss of an LPFG. The initial optical length of this particular fiber segment was found to be 31.806 mm based on Eq. (2.17). The fiber length was calculated to be 21.663 mm using the core refractive index of 1.4682 from the datasheet.

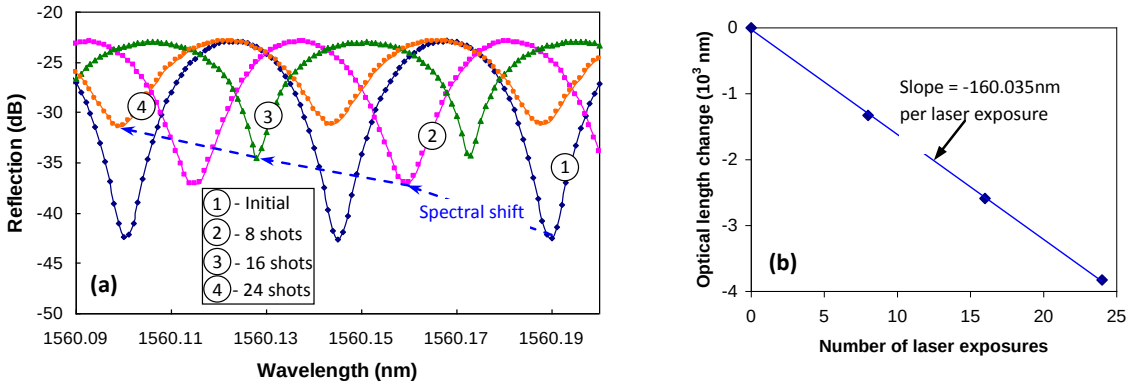

Figure 2.12 Optical length changes of fiber segment caused by CO_2 laser irradiations with the power of 8 W and exposure time of 125 ms; (a) interference spectra; (b) change in *OL* as a function of the number of laser exposures.

According to reference [79], the CO_2 laser irradiation induces a negative refractive index change in an optical fiber as a result of residual stress relaxation. The interference spectrum shifts to the short wavelength as the number of laser exposures increases. By tracing the interferogram shifts, we calculated the changes in optical length of the fiber segment based on Eq. (2.19). The results, as a function of the number of laser exposures, are plotted in Fig. 2.12(b), where the measured data points fit nicely into a line with a slope of -160.035 nm per laser exposure. Under the assumption that the FWHM of the laser induced refractive index perturbation profile was the same as that of the focused CO_2 laser beam (180 μm), the laser induced Δn_{max} was calculated to be -7.12×10^{-4}. Based on Eq. (2.7) and (2.8), the modulation coefficients s_0 and s_1, were determined to be -3.04×10^{-4} and -1.82×10^{-4}, respectively.

To investigate the possibility of controlling the laser-induced refractive index changes. We repeated above experiments by varying the exposure time of laser irradiation while keeping all other parameters the same. Fig. 2.13(a) shows the change in fiber optical length as a function of the number of laser exposures with four different exposure times of 50, 75, 100 and 125 ms, respectively. As the laser exposure time increased, the change in fiber optical length became more negative (i.e., increasing magnitude). The corresponding peak refractive index changes (Δn_{max}) are plotted in Fig. 2.13(b). We found that the laser-induced refractive index change is a very sensitive function of the laser exposure time. The magnitude of Δn_{max} increased with the increase

of laser exposure time, following almost a linear relation. Because the laser exposure time can be accurately varied by computer control (e.g., at the resolution of 1ms in our current laser system), it is possible to obtain a preferred refractive index modulation for fabrication of LPFGs with desired performance.

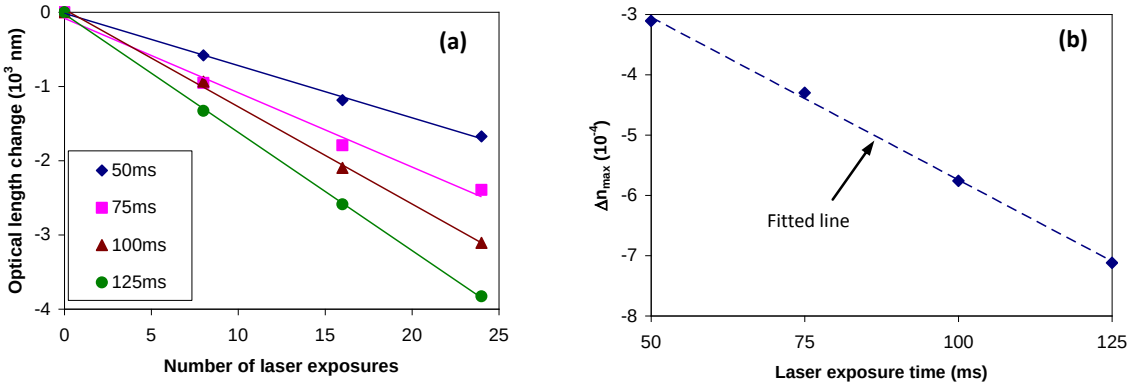

Figure 2.13 CO_2 laser irradiation induced fiber refractive index changes at various laser exposure times (50, 75, 100 and 125 ms, respectively); (a) *OL* change as a function of the number of laser exposures; (b) Δn_{max} as a function of laser exposure time.

The measured refractive index modulation coefficients were used to calculate the grating spectra in the wavelength range of 1510-1640 nm. The following Corning SMF-28e fiber parameters from datasheet were used in the calculations: core refractive index 1.4682 at 1550 nm, core and cladding index contrast 0.36%, and the core and cladding diameters of 8.2 and 125 μm, respectively. The period and length of the LPFG were 525 μm and 46.725 mm (total of 89 points), respectively. It was found that the resonance peak was a result of light coupling from the fundamental LP_{01} core mode to the LP_{05} cladding mode in the observing wavelength range. We also fabricated four LPFGs using the parameters corresponding to each simulation case for the purpose of verification. The simulated and measured transmission spectra are plotted in Fig. 2.14 where the background losses of the fabricated gratings were around 1 dB and subtracted from their original spectra for easy examination. There were large differences among the simulated and measured transmission spectra. As detailed in the insert tables, the measured resonant wavelengths were 1608, 1595, 1579, 1561 nm corresponding to the four different laser exposure times of 50, 75, 100 and 125 ms, respectively The simulated resonant

wavelengths, however, were at 1630, 1617, 1600, and 1580 nm. In addition, large differences existed in the resonance peak strengths.

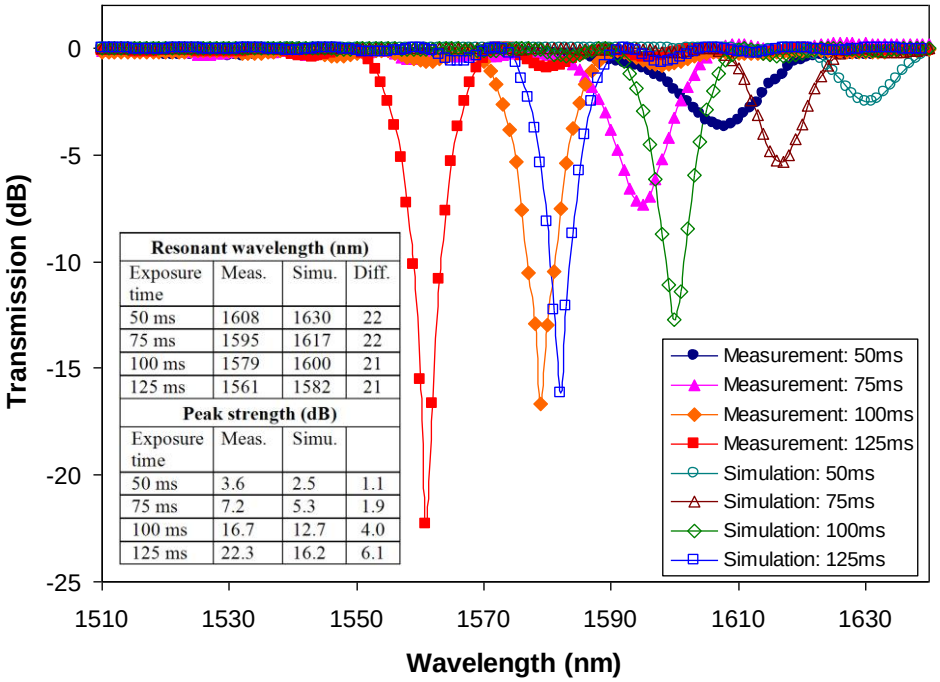

Resonant wavelength (nm)			
Exposure time	Meas.	Simu.	Diff.
50 ms	1608	1630	22
75 ms	1595	1617	22
100 ms	1579	1600	21
125 ms	1561	1582	21
Peak strength (dB)			
Exposure time	Meas.	Simu.	
50 ms	3.6	2.5	1.1
75 ms	7.2	5.3	1.9
100 ms	16.7	12.7	4.0
125 ms	22.3	16.2	6.1

Figure 2.14 Comparison between the measured and simulated transmission LPFG spectra. The simulations used the datasheet fiber parameters (Corning SMF-28e) and the FWHM of index perturbation of 180 μm (same as the measured FWHM of the laser beam). Inset table: detailed comparisons between measured and simulated resonant wavelengths and peak strengths.

However, it is interesting to note that the difference in resonant wavelength between the measured and simulated spectra of each corresponding case was almost constant, 21 or 22 nm. The resonant wavelength of a LPFG can be estimated by the following phase matching condition in Eq. (2.2). A constant offset between the simulation and the measured spectra in resonant wavelength suggests an offset in $n_{eff,\ core}$ and $n_{eff,\ cladding}$, which both depend on the fiber parameters. We modified the core-cladding index contrast slightly from the 0.36% (given in the datasheet) to 0.355% and repeated the simulations. The simulated spectra are shown in Fig. 2.15. The slight modification of the index contrast resulted in a large change in the simulated spectra. The use of modified fiber parameter produced much better match between the simulated and

measured spectra in all four cases. As detailed in the embedded table in Fig. 2.15, the difference in resonance wavelength was within 2 nm and maximum deviation of resonance peak strength was about 1.1 dB.

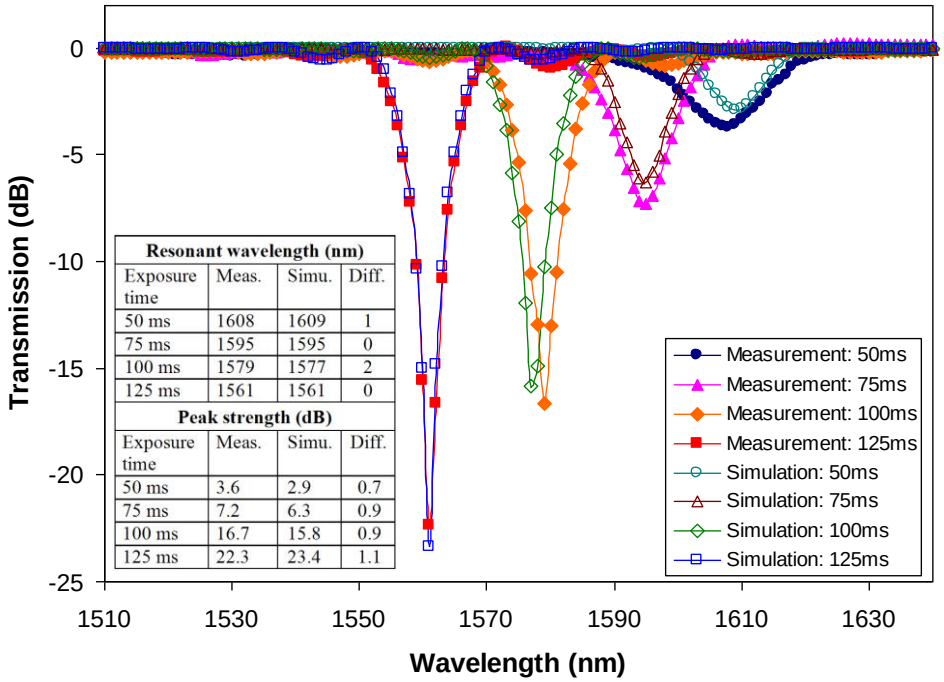

Resonant wavelength (nm)			
Exposure time	Meas.	Simu.	Diff.
50 ms	1608	1609	1
75 ms	1595	1595	0
100 ms	1579	1577	2
125 ms	1561	1561	0
Peak strength (dB)			
Exposure time	Meas.	Simu.	Diff.
50 ms	3.6	2.9	0.7
75 ms	7.2	6.3	0.9
100 ms	16.7	15.8	0.9
125 ms	22.3	23.4	1.1

Figure 2.15 Comparison between the simulated and measured transmission LPFG spectra. The simulations used a core-cladding index contrast of 0.355% (slightly modified from the datasheet value) and the FWHM of index perturbation of 180 μm (same as the measured FWHM of the laser beam). Inset table: detailed comparisons between measured and simulated resonant wavelengths and peak strengths.

The assumption of a Gaussian shaped refractive index along the fiber axis shall be valid at a low laser irradiation power. [79] However, previous research results indicated that the width of the refractive index perturbation might be smaller than the laser beam width. To investigate the influence, we assumed that the FWHM of the refractive index perturbation was 120 μm, which was significantly smaller than the measured FWHM of the laser beam (180 μm). The peak index change at each measurement point was recalculated based on Eq. (10). The new index data were used to repeat the LPFG simulations. The results are shown in Fig. 2.16. The maximum difference in resonant wavelength between the simulated and measured spectra was -4 nm, which happened

when the laser exposure time was 75 ms. The peak resonance strength matched well with those of real devices at short exposure times (50 and 75 ms) but had large deviations at long laser exposure times (100 and 125 ms).

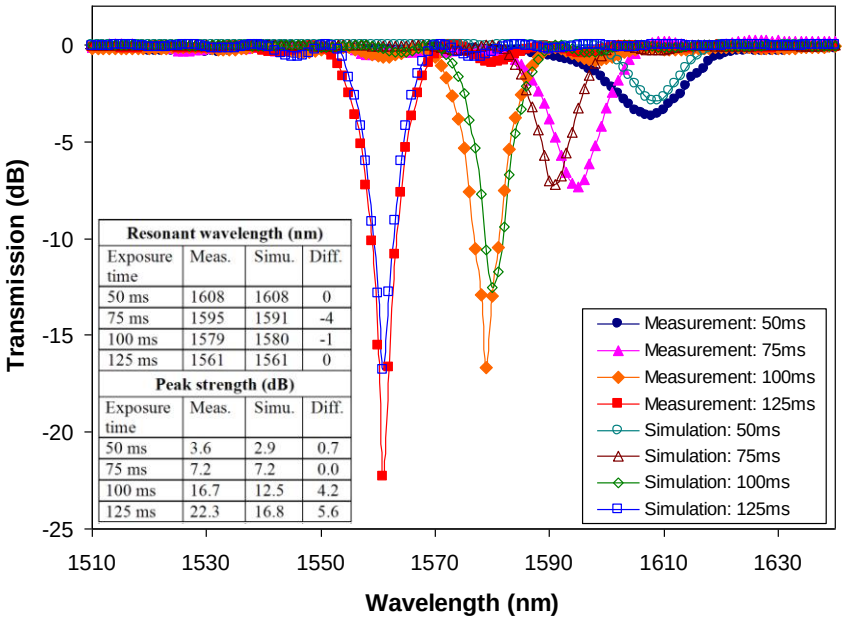

Resonant wavelength (nm)

Exposure time	Meas.	Simu.	Diff.
50 ms	1608	1608	0
75 ms	1595	1591	-4
100 ms	1579	1580	-1
125 ms	1561	1561	0

Peak strength (dB)

Exposure time	Meas.	Simu.	Diff.
50 ms	3.6	2.9	0.7
75 ms	7.2	7.2	0.0
100 ms	16.7	12.5	4.2
125 ms	22.3	16.8	5.6

Figure 2.16 Comparison between the simulated and measured transmission LPFG spectra. The simulations used a core-cladding index contrast of 0.355% (slightly modified from the datasheet value) and a reduced width of index perturbation of 120 μm (smaller than the measured laser beam width of 180 μm). Inset table: detailed comparisons between measured and simulated resonant wavelengths and peak strengths.

In general, we found that the transmission characteristics (especially the resonant wavelengths) of the simulated LPFG spectra did not change much even with one-third reduction in the width of refractive index perturbation profile. The relative insensitivity of the index perturbation width to the resonant wavelength (λ_{res}) can be explained using the following modify Bragg (or phase matching) condition [29]:

$$\left(\frac{2\pi}{\lambda_{res}} n_{eff,01} + s_0 \zeta_{01,01}(\lambda)\right) - \left(\frac{2\pi}{\lambda_{res}} n_{eff,05} + s_0 \zeta_{05,05}(\lambda)\right) = \frac{2\pi}{\Lambda} \tag{2.22}$$

where $n_{eff,\,01}$ and $n_{eff,\,05}$ are the effective refractive index of the fundamental core mode (LP_{05}) and the LP_{05} cladding mode, respectively; $\zeta_{01,01}$ and $\zeta_{05,05}$ are the self-coupling coefficients of the LP_{01} and LP_{05} modes, respectively.

Eq. (2.19) indicates that the grating resonant wavelength is mainly a function of s_0 for a chosen fiber. s_0 is the coefficient of the first term of the Fourier series, representing the dc level of the periodic index perturbation. The interferometric method described herein measures the total refractive index change. As indicated in Eq. (9), a reduction in the width of index perturbation required an increase in the peak index change (Δn_{max}) in order to maintain the same total refractive index change. Therefore, the dc level of index perturbation is relatively constant at the same measured total refractive index change.

However, the peak strength depends mainly on the ac component s_1 which contributes to the light coupling from the core mode to the cladding modes. [29] A change in the width of the index perturbation profile may cause a change in s_1. This explains the relatively large deviation of the peak strength in Fig. 8 when the width of index perturbation was reduced. Nevertheless, comparing the results shown in Fig. 2.15 and Fig. 2.16, we found that the case of using the laser beam width as the width of index perturbation produced a better match between the simulated and measured spectra.

There were some noticeable residual disparities in the simulated and measured LPFG spectra shown in Fig. 2.18, especially in the width of resonance peaks, and the difference became more pronounced at short exposure times (or small refractive index modulations). In addition to the measurement errors, we believe that the mismatches may be attributed to the following two major reasons. First, in the current simulation model, we only considered the light coupling between the core mode and the circularly symmetric cladding modes (e.g., LP_{0x}). This is under the assumption that the refractive index modulation has a uniform azimuthal distribution in the fiber cross section. However, it has been suggested that the CO_2 irradiation induced refractive index modulation may have non-uniform azimuthal distributions [91]. As the laser exposure time decreases, a non-uniform azimuthal refractive index modulation becomes more likely due to the nonequilibrium heat distribution within the short heating time period. The non-uniform azimuthal index perturbation in the fiber cross section promotes light coupling from the core mode (LP_{01}) to the circularly asymmetric cladding modes (e.g.,

LP_{1x}) [29], resulting in a difference between the simulated and measured spectra. Second, the critical fiber parameters, such as the diameter and the refractive indices of the core and cladding, of commercial products may vary from time to time. Unfortunately, as shown in our experiments, the slight change in fiber parameters may produce a large error in the simulated grating spectrum.

In summary, we demonstrated a new method to measure the CO_2 laser irradiation-induced refractive index modulation in the core of a single mode optical fiber for the purpose of design and fabrication of LPFGs. The total refractive index change was measured using an optical fiber Fabry-Perot interferometer. Under the assumption of a Gaussian-shaped axial refractive index perturbation, with a laser power of 8W, index perturbation FWHM of 180 μm (same as the laser beam width) and exposure time of 125 ms, the CO_2 laser irradiation generated a negative refractive index change in the fiber core with a peak value of -7.12×10^{-4}. The laser induced refractive index change was also measured at four different laser exposure times including 50, 75, 100 and 125 ms.

Using the first two terms of Fourier series approximation of the periodic Gaussian-shaped index perturbation profile, the axial refractive index modulations were computed to simulate the LPFG transmission spectra. LPFGs with the same laser exposure parameters were also fabricated for the purpose of verification. Using a slightly modified core-cladding refractive index contrast, the simulated spectra matched well with those of real devices. It was also found that the refractive index was a sensitive function of the laser exposure time following almost a linear relation. This relation can be used to guide the selection of a preferred refractive index modulation, through accurate control of the laser exposure time, for fabrication of LPFGs with desired transmission characteristics.

However, it is worth noting that the fiber parameters have a large impact on the simulated grating spectrum. In any case, a detailed comparison of the experimental data with simulated data is crucial. In addition, the described method does not apply to LPFGs fabricated with large tension because it does not consider the optical path change induced by fiber elongation.

2.6. HIGH TEMPERATURE PERFORMANCE AND IMPROVEMENT

2.6.1. High Temperature Survivability. To test the temperature survivability and sensitivity of the fabricated LPFGs, a LPFG was installed into an electric furnace and increased the temperature from 100°C to 800°C. The LPFGs used in the experience were fabricated with the same period of 500μm in Corning SMF-28 fiber. The temperature was held for one hour and measured the transmission spectrum of the LPFG at each 100°C increment as shown in Fig. 2.17 The grating transmission spectrum maintained the similar characteristics (e.g., strength and width) in all the temperatures except that the resonance wavelength of the LPFG moved to the long wavelength region when the temperature increased as shown in Fig. 2.17(a). Fig. 2.17(b) shows the resonant wavelength of the LPFG as a function of temperature. The test results clearly demonstrated that the LPFG successfully survived high temperatures up to 800°C. The results also indicated that the resonant wavelength was a linear function of temperature.

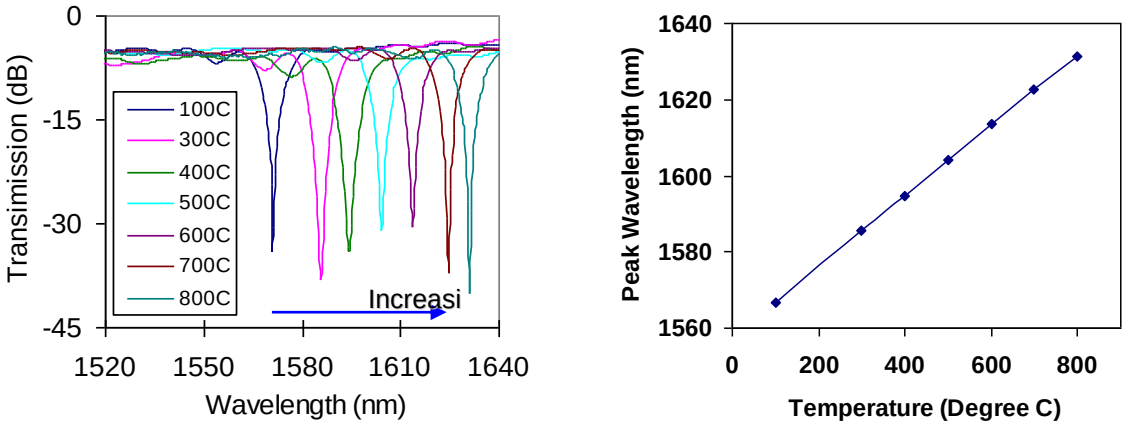

Figure 2.17 Test of LPFG at various temperatures (a) LPFG transmission spectra at different temperatures, (b) resonance wavelength as a function of temperature

2.6.2. Thermo Stability and Improvement. Annealing: The stability of the LPFG is a concern when it is designed and fabricated for high temperature applications. It is highly desired that the resonant peak of the grating does not drift when the grating is exposed to a high temperature environment for a long period of time. However, due to the fact that the refractive index change is caused by thermal treatment and the inevitable thermal relaxation of the treated glass, it is expected that the resonance wavelength will have a non-reversible drift, especially in a high temperature environment.

To evaluate the thermal stability of the fabricated LPFG, a CO_2 laser fabricated LPFG was placed in electric furniture at a temperature of 550 ℃. One end of the fiber was fixed to the test chamber (a ¼ inch stainless steel tube) while the other one was set loose so that the thermal expansion of the container itself would not affect the LPFG. As shown in Fig. 2.18, the lower curve with circle is the resonance wavelength as a function of time. A wavelength shift of 25.3nm after 200 hours was observed. It can also be seen that the wavelength change was faster at the beginning and getting slower as the experiment went along, indicating that the thermal stability of the LPFG improved after annealing. However, the improvement was slow and would take a long time to stabilize.

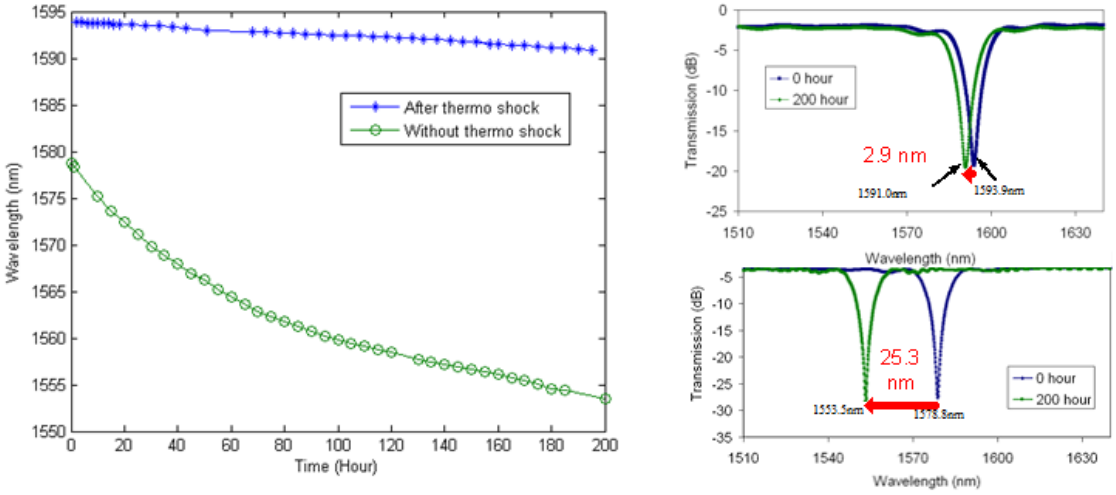

Figure 2.18 Thermo stability tests and improvement

Thermal Shock: In the second experiment, a LPFG was heated up to 700 ℃ for 2 hours, and then, cooled it down to 550 ℃ and maintained for 200 hours. As shown in Fig. 2.18 (the upper curve), the resonant wavelength still shows a continuous drift towards a shorter wavelength but with a much smaller shift of 2.9 nm after 200 hours annealing. The experiment indicates that thermal shock indeed improved the thermo stability of LPFG at high temperatures. To better understand the reason under this thermal shock phenomenon, it is necessary to go to the material fundamentals and the micro structure performance of the quiz. It is believed to be an issue in the future research.

2.7. LPFG APPLICATIONS

2.7.1. Ambient Refractive Index Measurement. Because the phase matching condition depends on the effective indices of the coupled cladding modes, which rely on the difference between the refractive index of the cladding and that of the medium surrounding the cladding, the resonance wavelengths of the LPFG show a dependence upon the refractive index of the medium surrounding cladding. LPFGs can thus be used to monitor the refractive index of the surrounding medium. To investigate the effect of refractive index of the surrounding medium on the resonance wavelength, the LPFG was placed in the air (refractive index =1), water (refractive index = 1.333), acetone (refractive index = 1.3590) and isopropanol (refractive index = 1.3776) and measured the transmission spectrum of the LPFG, respectively.

As shown in Fig. 2.19, the LPFG, fabricated with a period of 530 μm using a Corning SMF-28 fiber, had a resonance wavelength of 1583.23 nm in air. Its resonance wavelength shifted to 3.0229, 4.0019, and 4.3783 nm when placed in water, acetone, and isopropanol, respectively. In general, the resonant wavelength shifted towards the short wavelength region as the environmental refractive index increased. Figure 2.19 also plots the simulated resonance wavelength shift, with respect to that in air, as a function of the refractive index of the surrounding environment. The three measurement data points were charted on the simulated curve and found that the measured data were in a good agreement with the numerical simulations.

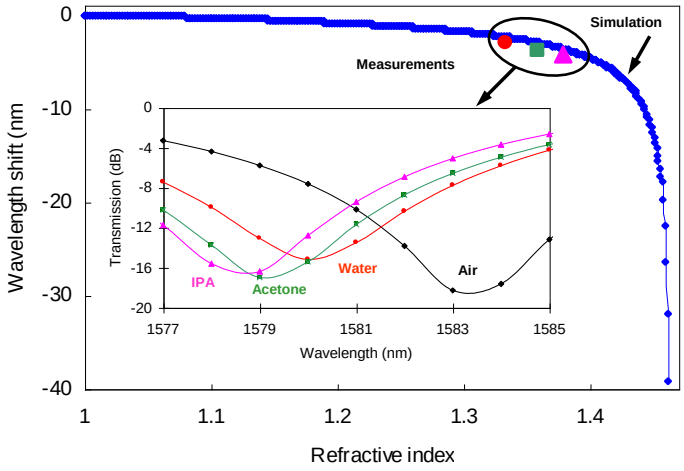

Figure 2.19 LPFG in response to ambient refractive index changes

In addition, the resonant wavelength shift as a function of refractive index of LPFG with higher cladding modes are measured as plotted in Fig. 2.20. By a quick observation, we conclude that the refractive index sensitivity, defined as resonant wavelength shift as a function of refractive index of ambient environment, is higher for resonance corresponding to higher cladding modes. The explanation for this phenomena can be drawn from the fact that higher order cladding mode extend more into the ambient environment, making it more sensitive to the ambient refractive index change.

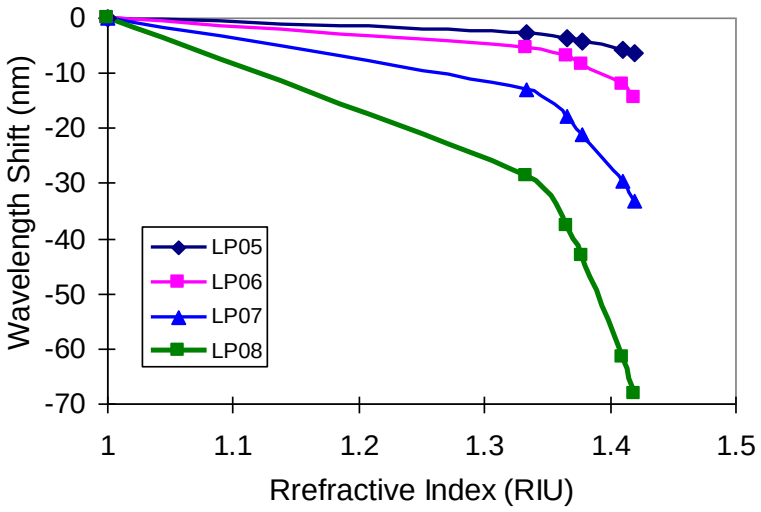

Figure 2.20 Resonant wavelength shift as a function of ambient refractive index

2.7.2. Palladium Coated LPFG for Hydrogen Sensing. Considered as a clean and renewable energy source, hydrogen has become a promising alternative to fossil fuels to solve the energy crisis and pollution problems. Consequently, in-situ monitoring hydrogen concentration has become important for the purposes of process control in hydrogen production and safety guard in hydrogen applications. In the last two decades, great efforts have been devoted into the development and commercialization of electrical type hydrogen sensors. Even though some of them exhibited high sensitivity and fast response time, a main drawback of electrical type sensors is that the use of electricity may lead sparks at the sensing point. As an alternative, optical sensors seem to be more attractive due to the lack of sparking possibilities. Moreover, most optical hydrogen sensors operate in a non-contact mode and can be deployed into regions where common electrical sensors are difficult to reach, especially when an optical fiber is used to

transmit the signal [92]. To perform hydrogen sensing, many of these optical sensors use specially designed sensing materials that selectively interact with hydrogen molecules to generate an optical signal [93, 94].

Principle of Operation: The hydrogen sensor designed in this work selected palladium (Pd) as the sensing material [95]. When Pd is exposed to hydrogen, hydrogen dissociates into two hydrogen atoms at the Pd surface with an efficient rate. The hydrogen atoms then diffuse into the palladium, resulting in the formation of palladium hydride (PdH). The hydration of Pd is also reversible. When the hydrogen concentration in the environment reduces, the Pd releases the adsorbed hydrogen. The hydration leads to an increase in the lattice parameters and consequently a decrease in the volume density of free electrons. As a result, the complex refractive index of the Pd changes, which can be used to monitor the hydrogen concentration in the environment.

The unique hydrogen related optical property of Pd can be used to develop a hydrogen sensor when integrated with a photonic device, such as the LPFG described in this thesis. The concept is to coat a thin layer of Pd film on a LPFG. Upon exposure to hydrogen, the coated Pd film changes its refractive index and correspondingly the mode coupling condition, resulting in a shift of the resonance wavelength of the grating. Therefore, by monitoring the resonance wavelength shift, the change of the hydrogen concentration can be accurately detected.

Experiment Setup: The nanosized Pd thin layer was deposited on LPFG by magnetron sputter deposition. During the deposition, the fiber was rotated periodically in order to prepare the thin film coating with relatively uniform thickness.

The schematic of hydrogen concentration sensing system is shown in Fig. 2.21. The Pd coated LPFG was placed in a 1/8-inch stainless steel tube. To simulate the actual application environment, two cylindrical gas tanks were connected to the stainless steel tube through a mixer. One is filled with hydrogen gas, while the other is helium gas. The gas flow rates of these two gases can be controlled individually by adjusting the mass flow controllers to obtain the desired concentration of hydrogen inside the stainless steel tube. The stainless steel tube was hosted inside an electric tubular furnace, by which the environmental temperature can be controlled. During sensor installation, one end of the Pd-coated LPFG sensor was fixed to the stainless steel tube by a gas stopper, while the

other end was set free to eliminate stress. The two ends of the fiber were connected to a broadband optical source and an optical spectrum analyzer (OSA), respectively. The resolution bandwidth was set 2 nm, while the number of the points taken by OSA within certain wavelength range was set 1000 for each scan. The OSA was connected to a computer, where the transmission spectrum of the LPFG was recorded and analyzed.

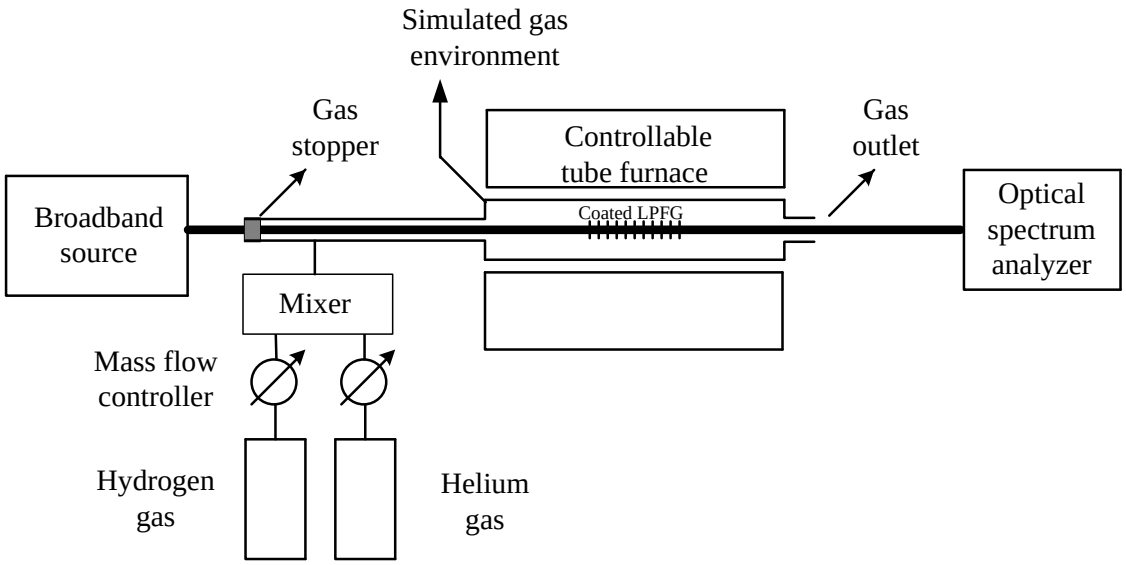

Figure 2.21 Schematic of Pd-LPFG in-situ measurement for hydrogen concentration sensing

Results and Discussions: Fig. 2.22 shows a scanning electronic micrograph (SEM) of the Pd-coated LPFG (Pd-LPFG), indicating a thin layer of uniform, defect-free Pd film has been successfully coated on the LPFG. The high magnification SEM image of the film (Fig. 2.21(b)) suggested that the Pd film had a nanostructure with a grain size distribution in the range of 20-30nm. It is preferred that the Pd coating remains in this nanostructure as it facilitates the speed of hydrogen adsorption and desorption. The thickness of the coating can be varied by change the duration of sputtering. In general, a thick coating results in high detection sensitivity. However, thick film will also reduce the speed of detection. Therefore, there is a tradeoff between the speed and sensitivity.

Prior to the test of the Pd-LPFG in response to hydrogen, the temperature dependence of the sensor was characterized. In the work, the shift of wavelength was found to be 35 pm/ ℃. The Pd-LPFG sensor was then tested in the temperatures ranging from 30 to 250 ℃ under various hydrogen concentrations. To minimize the noise influences, each measured transmission spectrum was first partially fitted by a 4-th order polynomial series. The resonance wavelength was then calculated as the tuning point of the fitted polynomial.

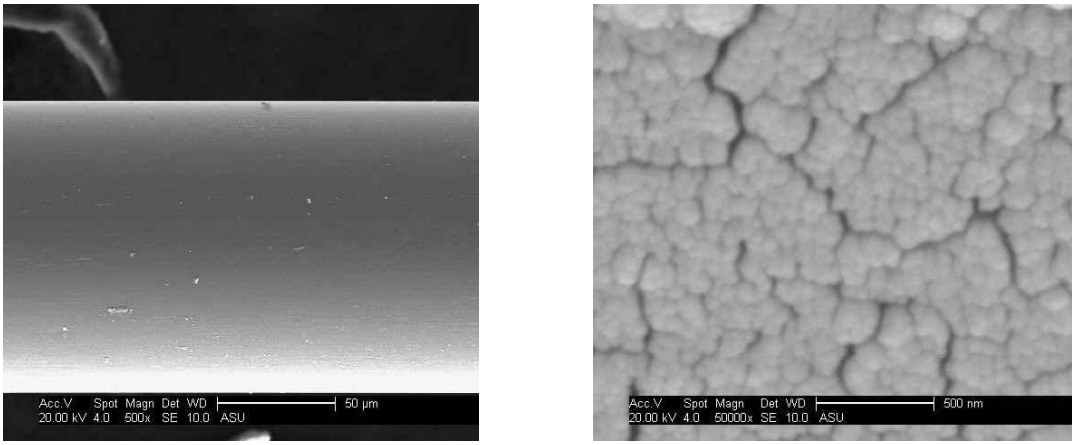

(a) (b)

Figure 2.22 SEM image of Pd-coated LPFG (a) 500x magnification (b) 50000x magnification

The transmission spectrums of Pd-LPFG in helium and 8% hydrogen at various temperatures are shown in Fig. 2.23, where the resonance wavelength clearly shifted towards the short wavelength region (blue shift) indicating the increase of Pd refractive index as a result of hydrogen adsorption into the thin film. Comparing the sensor response at various temperatures, it has been found that the amount of resonance wavelength shift highly depended on the temperature. As the temperature went up, the amount of blue shift decreased in response to 8% hydrogen concentration change. At room temperature, 8% hydrogen induced 4.2 nm of shift in resonance wavelength. While at 200°C, the same 8% hydrogen only caused about 0.1nm shift.

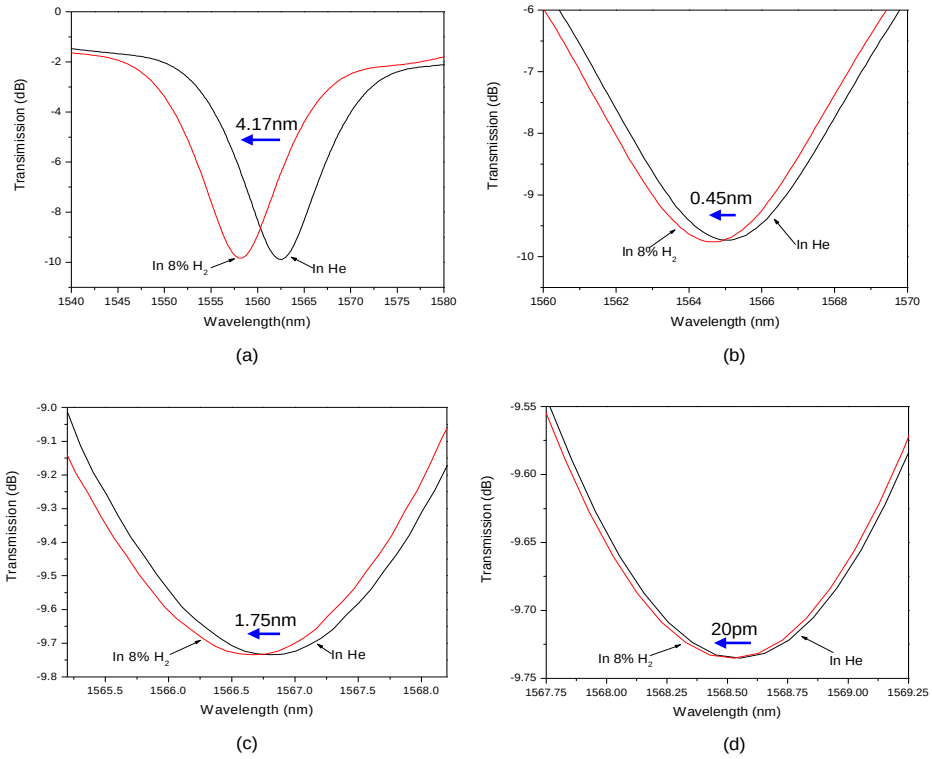

Figure 2.23 Spectrum of LPFG coated with Pd in 8% H_2 and H_2 free atmosphere at (a) room temperature (b) 100 ℃ (c) 150 ℃ (d) 200 ℃

The dependence of resonance wavelength shift as a function of hydrogen concentration at different temperatures is shown in Fig. 2.24. In general, it has been found that the amount of blue shift was almost linearly proportional to the hydrogen concentration up to 16%. However, the sensor response decreased significantly as the temperature increased. This can be explained by the fact that the hydrogen adsorption into the film reduces as the temperature increases. Even at 200 ℃, 4% hydrogen concentration increment resulted in a10pm shift in the resonance wavelength, which was still detectable using the existing system. However, when testing the sensor at 250 ℃, the amount of hydrogen dissolved into Pd was too low to cause any observable wavelength shift in the hydrogen concentration up to 16%. In conclusion, the tests successfully proved that Pd-LPFG sensor was working properly as expected in the temperature range from 25 ℃ to 200 ℃.

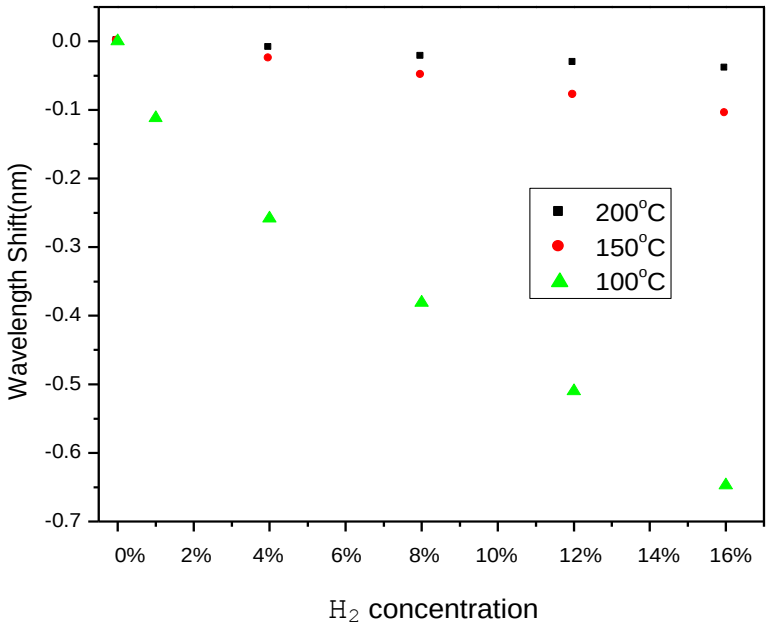

Figure 2.24 Wavelength shift as a function of H_2 concentration at various temperatures

The temporal characteristic of the Pd-LPFG in response to the hydrogen was also experimentally tested. Figure 2.25 shows the response and recovery time of Pd-LPFG when the sensor was exposed to 4% hydrogen at room temperature and 100 ℃, respectively. At each temperature, the response time to 4% hydrogen was less than one minute. The uptake time at 100°C was slightly shorter than that at room temperature. Compared to the hydrogen uptake process, the recovery time was much longer. At room temperature, it took about 5 minutes to shift back to the 90% of the original position in pure helium, and about 14 minutes to reach the completely stabilized point. It is worth noting that the response and recovery times also included the time required for the experimental setup to stabilize. At 100 ℃, the recovery time was much shorter than the case under room temperature. It took about 1 minute for the sensor recover to the 90% of its original value, and less than 5 minute to reach stabilization. The shorter response and recovery times of the sensor at a higher temperature can be explained by that fact that the adsorption and desorption of hydrogen are much fast at an elevated temperature as predicted by the thermal dynamics.

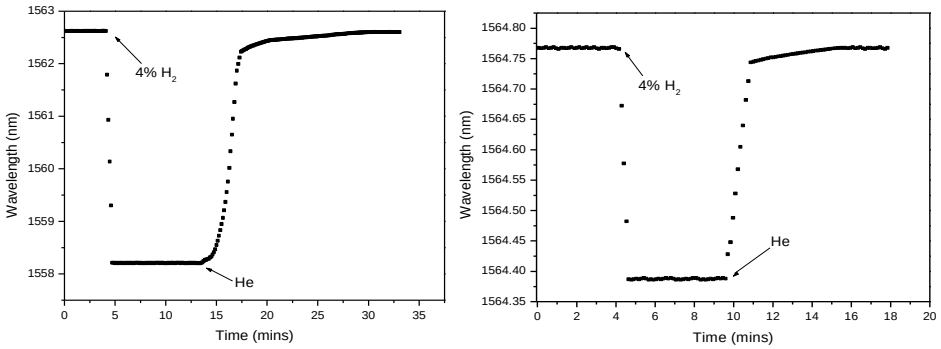

(a) (b)

Figure 2.25 Response time and recovery time of LPFG in 4% H_2 at (a) room temperature (b) 100^{o}C

The repeatability of the Pd-LPFG sensor in response to hydrogen was also experimentally evaluated at room temperature and 100 ℃, respectively, with the results shown in Fig. 2.26. In each test, the sensor was exposed to 4% hydrogen and recovered by pure helium for 5 cycles. The results indicated no observable difference in either the response time or the amount of wavelength shifts in different cycles, implying that the whole absorption and desorption process was repeatable within accuracy of instruments.

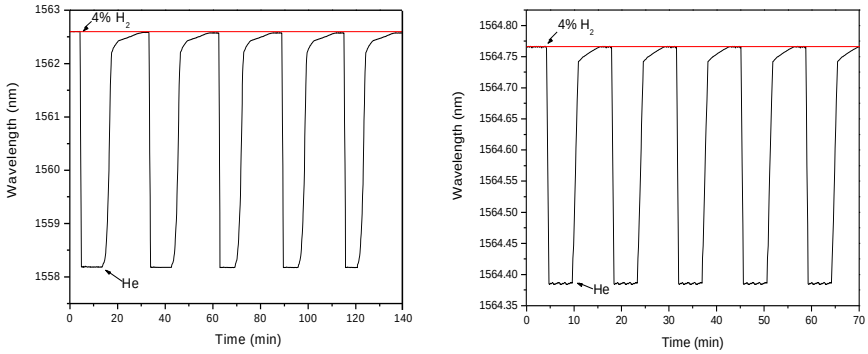

(a) (b)

Figure 2.26 Repeatability test of Pd-LPFG at (a) room temperature (b) 100^{o}C

2.7.3. Zeolite Thin Film-Coated LPFG for Trace Chemical Sensing. Zeolites are crystalline aluminosilicate materials possessing a unique combination of chemical and optical properties that is ideal for developing various optical chemical sensors [96-98]. The uniform nanopores with effective diameter from ~3Å to >10Å depending on zeolite structure and the enormous surface-to-mass ratio (400~1000 m^2/g) are suitable for selective molecular adsorption. The pore size and structure as well as the surface chemistry of zeolites can be finely tuned by isomorphous elementary substitution in the framework, exchange of the extra-framework cation compensators, and chemical deposition in the zeolitic cavity to further improve the selectivity of molecular adsorption [99-101].

Zeolites also have excellent thermal, chemical, and mechanical stabilities to function in harsh conditions. The adsorbed analyte molecules are organized and aligned in the nanoscale zeolite pores due to spatial confinement and guest-host interactions. Loading and unloading sorbate molecules can thus alter the optical and structural properties of zeolite that can be effectively examined by various optical methods [98]. Thereby, zeolites with multidimensional functions as an effective sample concentrator and optical probe have the potential for developing a variety of optical chemical sensors.

However, developing zeolite-based optical chemical sensors is still in the very early stage because of the difficulties associated with integrating zeolite with operational optical devices and the lack of fundamental understanding on the optical behavior of zeolite guest-host systems. Recently, we successfully synthesized highly coherent silicalite thin films on straight cut endfaces of single mode optical fibers [101]. The endface-coated zeolite-fiber device was used to investigate the relationship between zeolite refractive index and organic sorption level by an interferometric method [102, 103].

Silicalite is an organophilic material with an effective pore size of ~6 Å. It is an excellent adsorbent for a large number of organic molecules including aromatic compounds. The silicalite refractive index was found to increase from 1.3361 in pure N_2 to 1.4020 in 5353 ppm isopropanol vapor in N_2 [102]. This particular range of refractive index is desirable for constructing highly sensitive, film-coated LPFG sensors. In this

study, we demonstrate a silicalite thin film-coated LPFG sensor for highly sensitive detection of organic vapors.

Synthesis of zeolite film on the LPFG: A CO_2 laser fabricated LPFG with a period of 520 μm and a total grating length of ~5 cm was used. The LPFG was tested to be stable when annealing at 550^{o}C in air for 200 hours. Such thermal stability is necessary because the silicalite-coated LPFG requires activation by calcination at >400^{o}C to remove the structure directing agent (SDA) from the as-synthesized zeolite pores.

The silicalite film was grown directly on the LPFG cylindrical surface by *in situ* crystallization from an aluminum-free precursor solution using tetrapropylammonium ion (TPA^{+}) as SDA. The synthesis solution was prepared by mixing 11.3 ml (1M) of TPAOH (tetrapropylammonium hydroxide) (1M, Aldrich), 20.4 ml of TEOS (tetraethyl orthosilicate) (98%, Acros), and 60 ml of H_2O [101]. This particular precursor was found to be chemically friendly to the fiber surface due to its low alkalinity and high organic concentration. The mixture was vigorously stirred at 50 ℃ for 3 hours. The resultant clear solution was transferred into a Teflon-lined stainless steel synthesis vessel.

The synthesis vessel had a tubular geometry with a 3/4″ inner diameter and a total length of 13 cm. About 13 cm of the fiber including the stripped grating segment was mounted in the vessel. The fiber was positioned with the grating section located in the middle of the tube (vessel) length. The vessel was then sealed and placed vertically in an oven. The hydrothermal synthesis was conducted at 180 ℃ under autogeneous pressure for 4 hours. After the hydrothermal treatment, the zeolite-coated LPFG was rinsed with deionized water and then dried and fired at 500^{o}C in air for 2 hours to remove the TPA SDA.

The morphology and thickness of the zeolite film were examined by a scanning electron microscope (SEM). Fig. 2.27 shows the SEM images of the silicalite-LPFG. The images indicate that a continuous, well inter-grown zeolite film formed on the cylindrical LPFG surface although the outer surface had a discontinuous coverage of zeolite crystals. The thickness of the continuous zeolite layer was about ~10 μm as estimated from the SEM image. The crystals in the continuous zeolite layer appeared to be primarily *b*-oriented, which as straight channels with diameter of 5.6 Å.

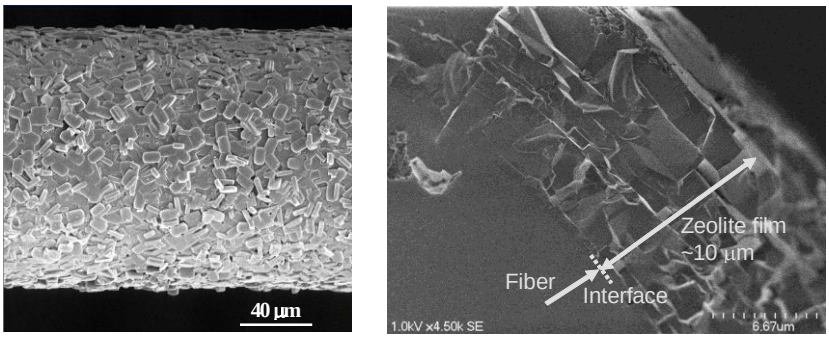

Figure 2.27 SEM pictures of the zeolite-LPFG surface (left) and fracture cross-section (right).

Organic vapor detection: The high temperature sensor activation and room temperature (i.e. 22^{o}C) chemical detection test were performed with an apparatus shown in Fig. 2.28. The zeolite-coated LPFG segment was hosted in a 1/8″–I.D. stainless steel tube, which is placed horizontally in a tubular furnace. The two ends of the stainless tube were connected to the sample gas supply system and ventilation, respectively. The concentration of the organic vapor was calculated from the vapor pressure at 0^{o}C and the diluting air flow rates, which were varied to control the vapor concentration.

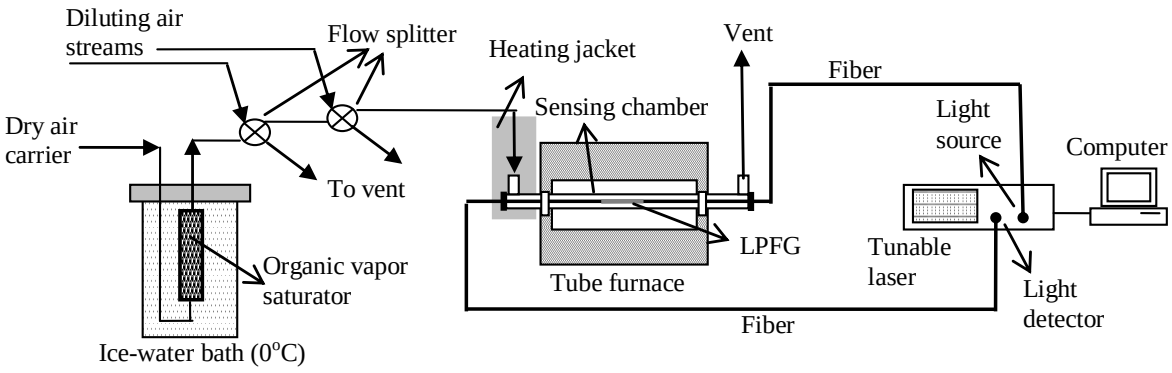

Figure 2.28 Schematic diagram of the sensor testing system

The transmission spectrum was obtained in a wavelength range from 1510 to 1640 nm. The source light was provided by a tunable laser equipped with a laser power detector (Agilent 8164A) and a computer data acquisition system. The calcination for

sensor activation was done by the following program: heating up to 500^{o}C at a rate of 4^{o}C/min, holding at 500^{o}C for 120 min, and then cooling down to room temperature at a rate of 2.5^{o}C/min.

The thermal activation process was continuously monitored by measuring the transmission spectrum at different temperature stages. Heating was paused during the spectrum scanning, which took about 130 s using a 1 nm wavelength step and a 1 s dwelling time. A wavelength increment of 0.1 nm and a dwelling time of 1 s were used in the organic sensing experiments.

As shown in Fig. 2.29, when heating up from room temperature to ~340^{o}C, λ_R increased with a linear temperature-dependence as a typical result of thermal effect on LPFG [104]. A drastic λ_R displacement of 21 nm toward smaller wavelength occurred at 350 – 380^{o}C where the SDA TPA molecules decomposed to free up the zeolite pores. As temperature further increased from 380 to 500^{o}C, λ_R of the SDA-removed LPFG continued to shift toward longer wavelength from the new λ_R value. No appreciable λ_R displacement was observed during the 120 min of dwelling time at 500^{o}C. The spectrum experienced a normal temperature-induced change of λ_R with no variation in resonant peak intensity during the cooling process. This indicates that the optical functions of the zeolite-coated LPFG were well preserved during and after the high temperature treatment. Also, the ability of LPFG to accurately detect the chemical reaction of loaded gust molecules (TPA^{+} in this case) may be potentially useful for *in situ* study of zeolite molecular catalysis which is a challenge in the chemical society.

The MFI zeolite-LPFG sensor was tested for detection of low concentration isopropanol and toluene vapors in air. The measurements were conducted at room temperature under atmospheric pressure. Fig. 2.30 and Fig. 2.31 present the results of the vapor detection tests. For both isopropanol and toluene vapors, increasing the vapor concentration caused λ_R shift toward smaller wavelength. Such a shift of λ_R is resulted from the increase of zeolite film refractive index induced by the increasing sorption of organic molecules into the zeolite cavity. The amount of analyte sorption increases as its concentration increases in the atmosphere. This observation is in good agreement with the predication of the three layer model.

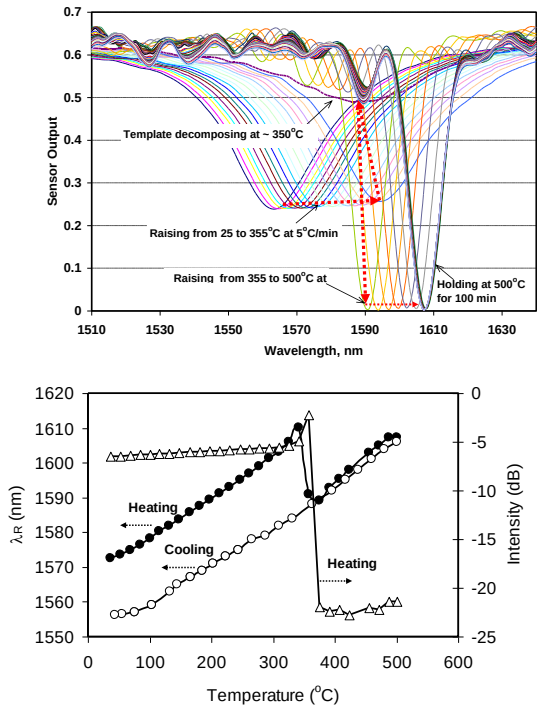

Figure 2.29 Spectrum evolution and λ_R and intensity changes during activation of the zeolite-LPFG sensor

The λ_R shifted 1.45 nm for an isopropanol vapor concentration of 5.5 ppm (parts per million) and shifted as much as 0.7 nm for a toluene vapor concentration of 0.22 ppm. The dependences of λ_R on the analyte vapor concentration are also provided in Fig. 5 and 6, which can be used for quantitative measurement after calibration. The measurement sensitivity and detection limit depend on the type of analyte molecule. For the same concentration, the amount of molecular sorption, sorbate-framework interaction, and molecular sorption-induced changes in zeolite structure and density are different for molecules with different chemical properties such as mass and polarity. These analyte-specific adsorbing behaviors affect the magnitude of variations in refractive index and optical thickness.

The zeolite-coated LPFG sensor response had a highly nonlinear relationship with the environmental analyte vapor concentration. This nonlinearity is caused by the dependence of zeolite refractive index on the nonlinear molecular adsorbing behavior. Because most of the zeolites exhibit type-I isotherms characterized by large equilibrium constants in low concentration region the sensor is particularly suited for trace detection.

It should be noted that the lowest concentration tested in this study was constrained by the sample gas generation technique used but not the limit for sensor detection.

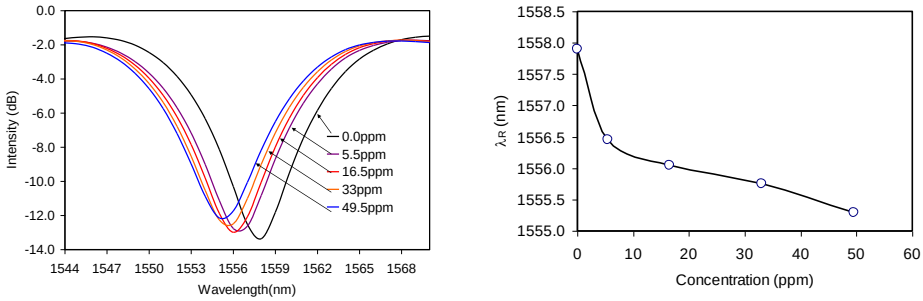

Figure 2.30 Displacement of transmission spectrum and λ_R as a function of isopropanol vapor concentration in air.

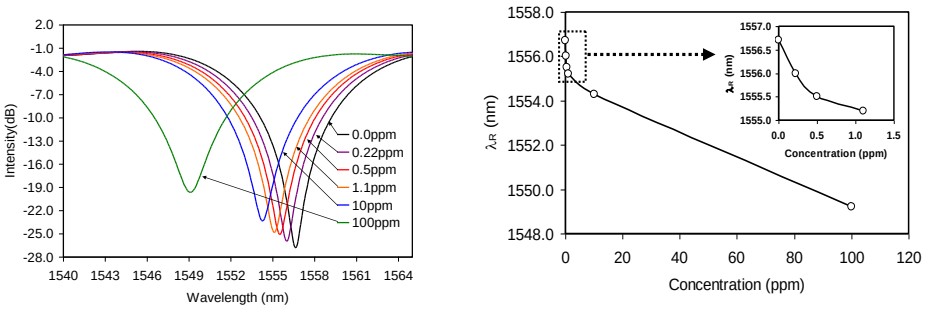

Figure 2.31 Displacement of transmission spectrum and λ_R as a function of toluene vapor concentration in air.

In conclusion, we demonstrated a zeolite-coated LPFG sensor for highly sensitive chemical vapor detection. The sensor operates by monitoring the molecular adsorption induced refractive index change of the zeolite coating. The zeolite film has multidimensional functions to act as an effective analyte collector/concentrator and an optical chemical probe. With its degassed refractive index around 1.33, the zeolite coating effectively shifts the operating point of LPFG to the region of higher sensitivity upon molecular adsorption. In the past decades, a large number of synthetic zeolitic materials, including the crystalline microporous aluminosilicates and their structural analogs of pure silica, borosilicates and aluminophosphates, have been developed with pore sizes ranging from 3Å to a few nanometers. The concept of physically and functionally integrating zeolite films with LPFG may offer new opportunities to develop a variety of chemical sensors for chemical detections with high sensitivities.

2.8. CONCLUSIONS

This chapter focused on one of the assembly free optical fiber inline sensors, LPFG. An LPFG has a grating period of several hundreds micrometers, much longer than that the optical communication wavelength. of the periodic refractive index modulation along the fiber length couples light from forward propagating core mode to the forward propagating cladding modes depending on the coupling conditions. Due to the lossy nature of the lcadding modes, the transmission spectrum of an LPFG has discrete loss peaks at specific resonant wavelengths. The fabrication technique in this work is by periodically point-by-point side irradiations of CO_2 laser pulses along an optical fiber. The refractive index change induced by CO_2 laser irradiation can be explained by the stress release effect. Such fabrication technique is supreme to the conventional UV exposure method for the reason that the CO_2 laser inscribed grating is capable to survive a temperature as high as 1000 ℃, making it possible to serve as high temperature, harsh environment sensor. An automated CO_2 laser based LPFG fabrication station was successfully implemented in our lab. High quality (e.g., low insertion loss and deep resonance) LPFGs of various cladding modes were successfully fabricated. By changing the grating period, we successfully fabricated LPFGs of LP_{05} through LP_{09} cladding modes with resonances in the optical communication wavelength regime. In general, we found that LPFGs of higher order cladding modes were more sensitive to both the temperature and the ambient refractive index in general.

An analytical LPFG model was established based on coupled mode theory. Transfer matrix method is used to solve the coupled differential equations and simulate the transmission spectra of LPFGs. The modeling work followed a procedure including calculation of the propagation constant of the LP_{0x} cladding modes based on the assumption of an azimuthally uniform cross-sectional index modulation, calculation of the inter modal coupling coefficient, establishment of the mode coupling differential equation matrix, and solving the coupled-mode equation matrix by applying the boundary conditions.

The CO_2 laser irradiation induced refractive index change in fiber was innovatively measured using optical interferometry. The index change was measured as a function of the laser insensitivities and as well as the pulse durations. It was found that

exposing a corning SMF-28 fiber to CO_2 laser irraditions actually decreased the refractive index in an optical fiber. The measured index modulation parameters were then applied to the established LPFG model and the simualted grating spectra agreed well with those of real devices fabricated using the same laser exposure conditions. Together with the established device model and simulation tool, the measurement results can be directly used for guiding the device fabrication.

The high-temperature survivability and stability of LPFG fabricated by CO_2 laser irradiations have been experimentally investigated. A thermal shock method was proposed and investigated to improve the high temperature stability of the LPFG. We also demonstrated the sensing capability of the LPFG in three application cases. The first one was the measurement of ambient refractive index using uncoated LPFGs. LPFGs with different cladding modes were tested for comparison and we found that the higher the cladding mode order was, the higher the sensitivity of the device in response to the refractive index change. In the second case, LPFG were coated with Pd films of nanometer thickness and used to measure the H_2 concentrations at various elevated temperatures. The last demonstration was using zeolite coated LPFG for chemical sensing. We found that the zeolite-coated LPFG had very high sensitivity (~ppb) for trace chemical detection.

3. FIBER INLINE CORE CLADDING MODE INTERFEROMETER SENSOR

This chapter reports a new assembly-free optical fiber incline sensor fabricated by controlled CO_2 laser irradiations and operating based on the optical interference between the core and cladding modes in an optical fiber. The operation principle of such a core-cladding mode interferometer is described and the possible configurations are presented. The previous reported fabrication techniques are reviewed and the associated challenges are discussed. A new method of using a CO_2 laser to fabricate such a device is proposed and studied experimentally. The mode excitation in the device is also discussed based on experimental results. The new device is evaluated for its capability for high temperature sensing applications.

3.1. INTRODUCION

Among optical fiber sensors, fiber inline core-cladding-mode interferometers (CCMI), including both Mach-Zehnder Interferometers (MZI) and Michelson Interferometers (MI), have attracted much interest recently. The operation mechanism of such a CCMI device is to couple a fraction of light propagating inside the core of a fiber (a single mode fiber in most cases) to the cladding modes, then to blend them after a certain distance. Both optical arms, traveling in fiber core and fiber cladding, undergo different optical paths, producing detectable interference. One unique feature of the inline CCMI is its sensitivity to the refractive index of the surrounding medium. Similar to a LPFG, the refractive index change of the environment around the fiber cladding can significantly vary the effective refractive index of the cladding modes, but barely impacts the light transmitting inside the core. As a result, the inline CCMI can be used as refractive index sensor by tracking the phase shift of the interference fringe. Due to the inline, assembly free structure of the sensor structure, the CCMIs are expected to survive high temperature harsh environments.

Other applications of such a CCMI have also been proposed. Examples include a temperature sensor based on the different changes of the core and cladding refractive indices in response to a temperature variation, pH, strain sensors and a curvature sensor

or inclinometer based on detecting the bending induced interference fringe shift. [105-118]

Fabrication of such a CCMI requires a mechanism to couple the light from the core into the cladding and vice versa. So far, a number of fabrication techniques have been demonstrated, including core diameter mismatch, fiber tapering, pair of LPFGs, micro structure collapsing on a photonic crystal fiber and tilted fiber bragg gratings [106, 115, 117, 119-121].

In this chapter, we report a new method to fabricate a fiber inline CCMI by controlled CO_2 laser irradiations. The laser irradiation induced a micronotch on the fiber structure, causing light coupling from the core mode to cladding modes, and vice versa. Compared with other fabrication techniques, the CO_2 laser irradiation method is simple, avoids complicated assembly, and maintains the mechanical property of an optical fiber. Additionally, with the help of precision transition stage, the optical length of the CCMI can be accurately controlled.

3.1.1. CCMI Configurations. The principle of operation of a typical MZI type CCMI sensor is illustrated in Fig. 3.1, where two mode splitters/combiners (MSC) is created on a single mode fiber. These two MSCs are separated by a distance of L, which is referred as to the length of the interferometer. The input light, originally guided inside the fiber core, is split into two parts at the first MSC. Part of the light remains propagation inside the fiber core while the rest is coupled into the fiber cladding. Passing through the interferometer section, the light traveling inside cladding is coupled back to the core at the second MSC, mixing with the core mode component to generate an interference signal.

The MI type CCMI sensor operates very similarly as the MZI type. As shown in Fig. 3.1, the MI type sensor is a “half” MZI-CCMI. Part of the light is coupled from the core mode to the cladding mode at the MSC. They propagate through the interferometer and are reflected from the cleaved fiber endface. Sometimes, the cleaved fiber endface can be coated with a highly reflective film to improve the signal strength. The two backward propagating waves are mixed again at the MSC, generating an interference

signal. A unique advantage of the MI-CCMI is that the sensor operates in reflection mode which can be conveniently deployed.

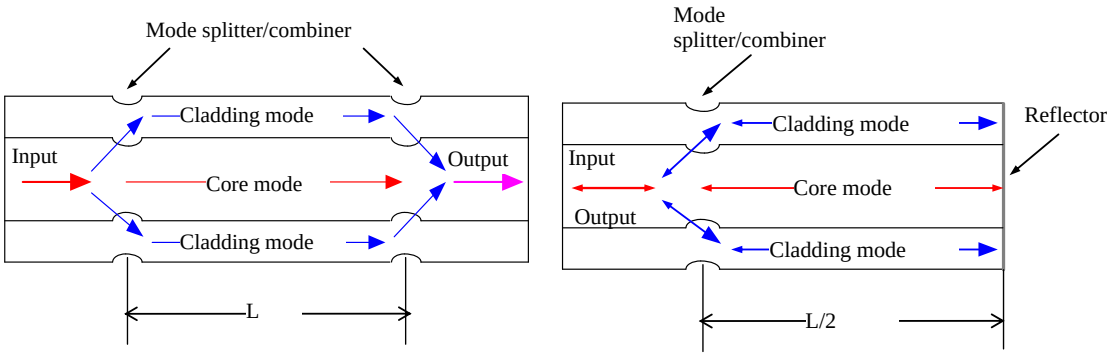

Figure 3.1 Principle of fiber inline CCMI sensors (a) Mach-Zehnder type, (b) Michelson type

3.1.2. CCMI Operating Principle. The CCMI can be modeled using the following two-beam interference equation:

$$I = I_1 + I_2 + 2\sqrt{I_1 I_2}\cos\left[\frac{2\pi(n_c^{\,eff} - n_{cl}^{\,eff})L}{\lambda} + \phi_0\right] \tag{3.1}$$

where, I is the intensity of the interference signal; I_1 and I_2 are the intensity of light propagating in the fiber core and cladding, respectively; L is the interferometer length; λ is the free space wavelength; Φ_0 is the initial phase of the interference; $n_c^{\,eff}$ and $n_{cl}^{\,eff}$ are the effective refractive indices of the core and cladding, respectively. The effective refractive index (n_{eff}) is related to the propagation constant (β) by $\beta = 2\pi\, n_{eff}/\lambda$. The typical interference spectrum of a CCMI is illustrated in Figure 3.2.

Eq. (3.1) indicates that a CCMI can be used for sensing various physical and chemical parameters. Sensing of physical parameters (e.g., temperature, strain and pressure) mainly relies on the measurement of the measurand induced interferometer length change. For example, the thermo-optic coefficients of the core and cladding materials of an optical fiber are different. As a result, the refractive index changes

different amount in the core and cladding as a function of temperature. The interferometer can thus be used to measure the environmental temperature.

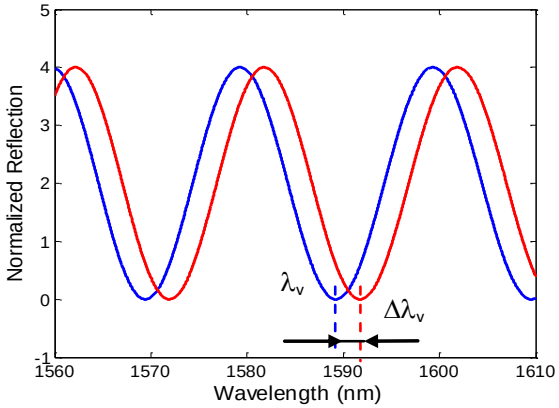

Figure 3.2 Illustration of the interference spectrum of a CCMI.

3.1.3. CCMI Based Chemical Sensor. A CCMI based chemical sensor operates by monitoring the environmental refractive index change. The core mode is guided by the core-cladding interface of the fiber and well shielded by the thick cladding. Therefore its propagation is insensitive to the refractive index change of the environment. However, the cladding mode, which is guided by the cladding-ambient interface, is directly exposed to the environment. As a result, its effective propagation constant (β_{cl}) is sensitive to the ambient refractive index change. The interference between the core mode and the cladding mode carries the ambient refractive index information, which can be used to develop compact, highly sensitive chemical sensors.

According to Eq. (3.1), the interference spectrum reaches its minimum (I_{min}) when the phase of the cosine term becomes an odd number of π. That is

$$I = I_{\min}, \qquad \text{when } \frac{2\pi(n_c^{eff} - n_{cl}^{eff})L}{\lambda_v} + \phi_0 = (2k+1)\pi \tag{3.2}$$

where k is an integer and λ_v is the center wavelength of a specific interference valley.

It is well known that the propagation constant of the cladding mode (thus n_{cl}^{eff}) is a function of the refractive index of the surrounding medium. On the other hand, the core mode is shielded by the cladding layer so its propagation constant does not vary when the surrounding medium changes its refractive index. The interferometer can thus be used as a sensor to monitor the environmental refractive index change.

In Eq. (3.2), taking the derivative of n_{cl}^{eff} with respect to λ_v, one finds:

$$\frac{dn_{cl}^{eff}}{d\lambda_v} = -\frac{(2k+1)\pi - \phi_0}{2\pi L} \quad . \tag{3.3}$$

In many cases, only the relative index change is of interest and the range of refractive index variation is small so the phase shift is less than 2π. Under this circumstance, the phase ambiguity issue can be avoided. The relative refractive index change can be computed based on the wavelength shift ($\Delta\lambda_v$ as shown in Fig. 3.2) of a particular interference valley using the following equation derived based on Eq. (3.3):

$$\frac{\Delta n_{cl}^{eff}}{n_{cl}^{eff}} = \frac{\Delta\lambda_v}{\lambda_v} \tag{3.4}$$

It is worth noting that Eq. (3.4) is also applicable to other characteristic spectral positions such as the interference peak and the center point of the interferogam. In addition, curve fitting of the interference fringe can also improve the measurement accuracy.

3.2. CCMI FABRICATION

3.2.1. Review of CMMI Fabrication. One of the key issues in fabrication of the CCMI device is to create high-quality mode splitters/combiners on an optical fiber. Over the years, a number of techniques have been explored, including the core diameter mismatch, fiber tapering, pair of LPFGs, micro structure collapsing on a photonic crystal fiber and tilted fiber Bragg gratings [106, 114, 115, 117, 119-121]. These fabrication techniques are briefly reviewed in this section.

Core Mismatch Techniques: Yam et al. demonstrated Mach–Zehnder and Michelson interferometers using core-offset attenuators, fabricated by a commercial fiber splicing machine with built-in attenuator program, shown in Figure 3.3 [114]. At the mismatched splicing interface, the light from the core of the input fiber is partially coupled into the cladding of the receiving fiber. As such, when they re-join at the second mismatched splice point, optical interference can be obtained. In general, the mismatch technique lacks the necessary control over the amount of light coupling from one-fiber to another. In addition, the cladding modes excited by the mismatched splice are random. As such, it is difficult to fabricate high-quality device using this method.

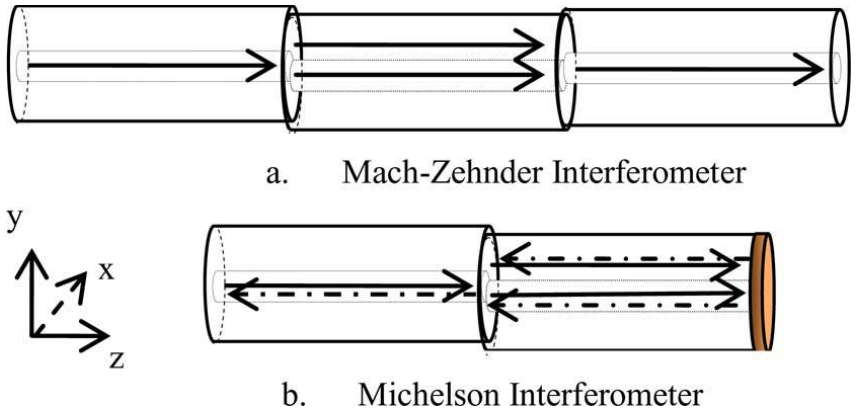

Figure 3.3 Structure of core-offset attenuator-type interferometer

Nguyen et al report a simple fiber sensor for measurement of high temperature with high sensitivity. The sensing head is a multimode-single mode-multimode (MM-SM-MM) fiber configuration formed by splicing a section of uncoated single mode fiber (SMF) with two short sections of multimode fibers (MMF) whose core is composed of pure silica, shown in Fig. 3.4. Because of the mode-field mismatch at the splicing points of the SMF with 2 sections of MMFs, as well as index matching between the core of the MMF and the cladding of the SMF, optical power from the lead-in fiber can be partly coupled to the cladding modes of the SMF through the MMF. The cladding modes of the SMF then re-coupled to the lead-out fiber, in the same fashion. The interference pattern was found to shift to the longer wavelength region with respect to temperature variation.

The temperature sensor can measure temperature stably up to more than 900 ℃ with sensitivity of 0.088 nm/ ℃ [112].

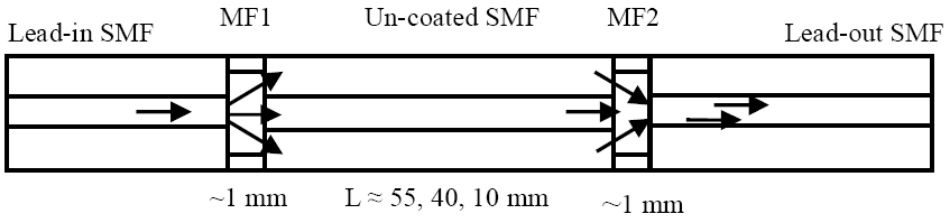

Figure 3.4 Schematic of MM-SM-MM configuration

The alternating SMF-MF structure has a better control in terms of the excited cladding modes. However, the fabrication process is complicated and the lengths of the MF need to be controlled accurately. As such, the success rate is expected to be low.

LPFG pair Technique: One of the methods to form CCMI is by cascading a pair of LPFG, which was firstly introduced by Dianov et al in 1996 [122]. Fig. 3.5 shows the schematic of such a device, where some of the light is coupled to the cladding mode near the resonant wavelength, following the blue path in the figure. It is worth noting that the interference visibility or extinction ratio reaches its maximum, when the LPFG promotes half of the energy into the cladding modes. The second LPFG is used collect the cladding mode energy and to form an interference pattern by mixing these two beams, which can be detected via the transmitted wave. Figure 3.6 plots the spectrum of LPFG-MZ-CCMI with LP_{05} cladding mode resonance with grating pair located 8 cm away from each other.

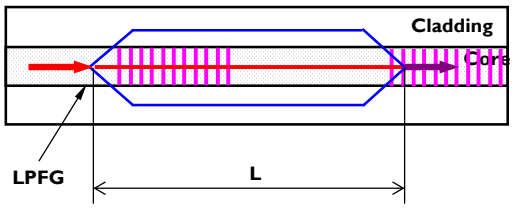

Figure 3.5 Schematic of LPFG-MZ-CCMI device

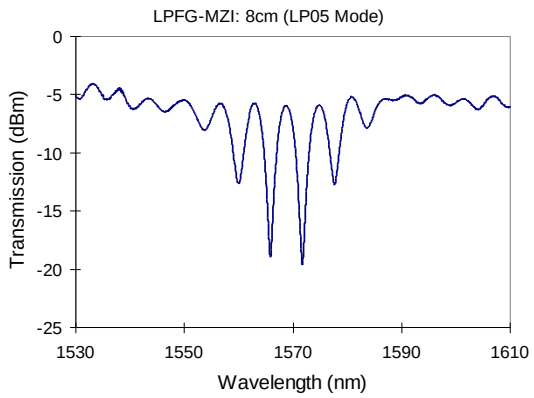

Figure 3.6 Transmission spectrum of LPFG-MZ-CCMI with LP_{05} cladding modes

In general, LPFG pairs CCMI is easy to control in terms of energy coupling ratio and coupling wavelength range, since LPFG fabrication techniques are comparatively mature. However, LPFG pair based CCMI is limited to the fact that the core-to-cladding coupling solely happens near the resonant wavelength. Therefore, when the targeted sensing parameter changes too much, the interference pattern may shift out of the observation wavelength range. The other restriction for such a device is that the LPFG is usually a couple of centimeters long, making it a fairy long sensor probe. Core mismatch method, on the other hand, is supreme to LPFG pairs, since the interference pattern spans all over the wavelengths, and we do not suffer loose-track during the measurement. However, the drawback for core mismatch method is that it endures a complicated fabrication procedure, and in particular, the assembling is full of complexness. In addition, short interferometer length is too difficult to handle, therefore, so-fabricated sensors generally have a length of tens of centimeter. Also, limited by the cleaving uncertainty, the length was not actually control. This work proposed a novel method using strong CO_2 laser fabrication pulse, which may overcome the fabrication complexness and length accuracy.

3.2.2. CMMI Fabrication Using CO_2 Laser Pulses. In this research, we investigated a new method to fabricate the CCMI device using controlled CO_2 laser irradiations. A CO_2 laser (SYNRAD, Inc.) with a free space wavelength of 10.6 μm and a maximum output power of 20W was used in the system. A ZnSe cylindrical lens with a

focal length of 50mm was used to shape the CO_2 laser beam into a narrow line with a linewidth of around 220 μm. The CO_2 laser was controlled by a computer so that the output power and exposure time-trajectory could be accurately adjusted. A three dimensional (3D) motorized translation stage was used to position the optical fiber to the center of the focused laser beam with the fiber axis perpendicular to the laser line. A microscope vision system was used to visualize the optical fiber. During fabrication, the CO_2 laser heats the fiber and created the first micronotch at one position. Controlled by the computer, the translation stage moved the fiber with a certain distance. Then the laser was fired again to create the second micronotch. These two micronotches and the fiber in between made a fiber inline core-cladding-mode MZI.

Fig. 3.6 shows a microscopic image of a typical micronotch on an optical fiber induced by CO_2 laser irradiation. At the micronotch, part of the light guided by the fiber core is coupled into the cladding mode. The reset of the light remain propagation inside the fiber core. Passing through the interferometer section, the light traveling inside cladding is coupled back to the core at the second micronotch, mixing with the core mode component to generate optical interference.

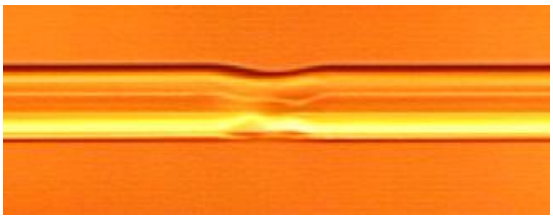

Figure 3.6 Microscopic image of a typical micronotch on an optical fiber induced by controlled CO_2 laser irradiation.

A tunable laser (HP81642A) and an optical power meter (HP 81618A) were used to monitor the MFI transmission spectrum. The tunable laser is coupled into one end of the fiber and the other end is connected to the power meter. The tunable laser was controlled by the computer to step from 1510 to 1640 nm at a step size of 1 nm and the transmitted power was detected by the optical power meter so that the interference spectrum could be recorded after its fabrication.

3.3. RESULTS AND DISCUSSIONS

3.3.1. Interferogram of CCMI. Using the described system, we made several fiber inline MZI type CCMI on Corning SMF-28e single mode fibers with different interferometer lengths. The laser power was set to 10 W and the exposure duration was 300 ms. Fig. 3.7 shows the interference spectra of MZIs with the length of 5, 10, 20 and 40 mm, respectively. The typical interference fringe had a visibility around 20 dB, which was sufficient for most sensing applications. The background loss varied among devices with a typical value of about 10 dB. With the increase of the interferometer length, the spectral separation between two adjacent interference fringes decreased in approximately an inversely proportional fashion.

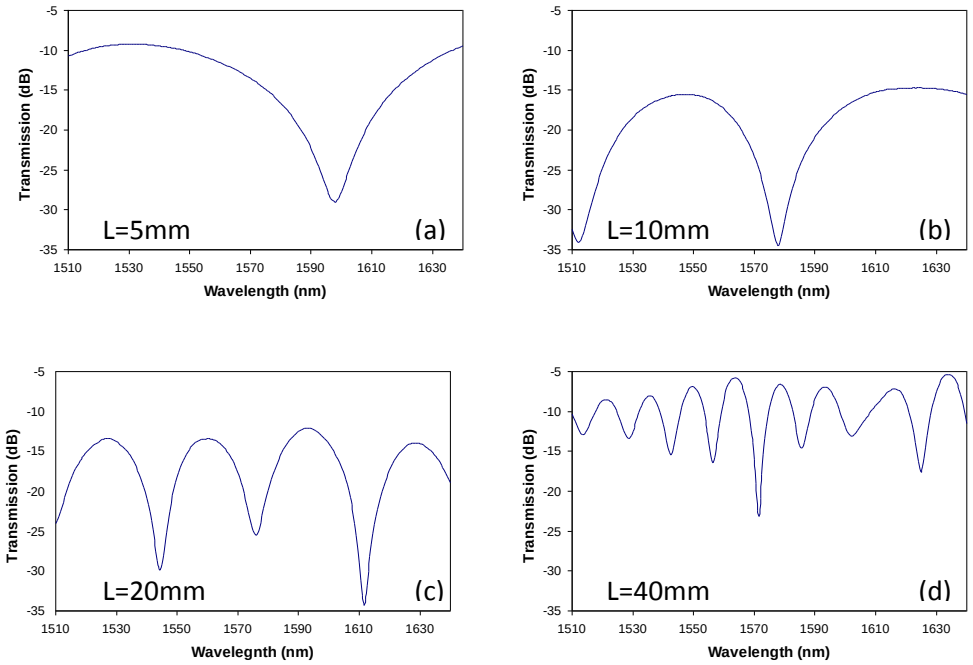

Figure 3.7 Transmission spectra of fiber inline core-cladding-mode MZIs with different interferometer lengths: (a) 5 mm; (b) 10 mm; (c) 20 mm; (d) 40 mm.

3.3.2. Sensing Capability of CMMI. Temperature Sensing: A fiber inline MZI with a length of 5 mm was employed to evaluate its sensitivity towards temperature variation. The interferometer was placed in a quartz tube without stress, fixed in a tubular electric furnace (Lindberg/blue M). A broadband source made by multiplexing a C-band (AFC, BBS-1550A-TS) and an L-band (Highwave, HWT-BSL-P) erbium-doped fiber

amplified-spontaneous-emission (ASE) source was used to excite the device. The reflected interference signal from the sensor was detected by an optical spectrum analyzer (OSA, HP70952B). The spectral resolution of the OSA was set to 0.5 nm and 1000 data points were taken per OSA scan. The device was first heated up to 120 ℃ read from the built-in thermometer of the furnace. The furnace was then turned off to allow the temperature cool down while the interference spectra were recorded at around every 10 ℃ of temperature dropping. The recorded interference spectra were processed to find the spectral position of the interference minima. The temperature response test ended till the temperature inside the furnace reached 50 ℃. Fig. 3.8 shows the wavelength shift of the interference minimum as a function of the furnace temperature where the relation is roughly linear. The linear fit of the experiment data indicated that the temperature sensitivity of the device was 0.0817 nm/°C. The temperature sensitivity of the device can be attributed to the different thermo-optic dependence of the fiber core and cladding modes [119, 123]. n_c^{eff} and n_{cl}^{eff} changes differently when temperature varies, causing a phase shift of the interference fringe as predicted by Eq. (3.1).

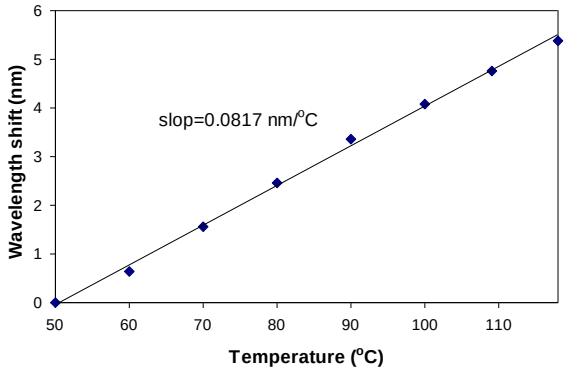

Figure 3.8 Temperature response of a fiber inline MZI fabricated by 2-point CO_2 laser irradiation

As observed from Fig. 3.8, inteferogram shift follow a well-defined linear curve. The device was first heated up to 1100 ℃ read from the built-in thermometer of the furnace, then cooled down while the interference spectra were recorded at every 100 ℃ drop of temperature. The recorded interference spectra were processed to find the spectral

position of the interference minima. The temperature response test ended till the temperature inside the furnace reached 50 ℃. Fig. 3.9 shows the wavelength shift of the interference minimum as a function of the furnace temperature at high temperature range where the relation is nonlinear. It behaves more sensitive at higher temperature.

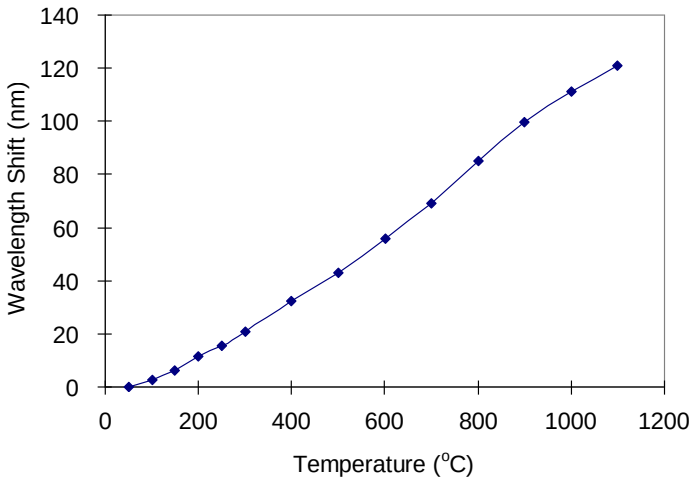

Figure 3.9 Temperature response of a fiber inline MI-CCMI device fabricated by CO_2 laser irradiations

Ambient Refractive Index Sensing: The same fiber inline MZI used in temperature response test was evaluated for its capability for refractive index measurement at room temperature. Various liquids were used including deionized (DI) water, isopropanol (IPA) and refractive index liquids ranging from 1.40 to 1.44. During the tests, the device was fixed on a glass plate to avoid any bending induced signal change. Then we immersed the glass plate into different liquids and recoded the interference fringes for each test. The device was carefully cleaned by subsequent acetone and water ultrasonic baths and air dried between tests in different liquids to avoid any liquid residue from previous test.

Fig. 3.10 shows the wavelength shift of the fiber inline MZI with respect to refractive index change. The increase of ambient refractive index caused a shift of the interference spectrum towards the short wavelength. In addition, the sensitivity grew as the refractive index approaching that of the cladding. This can be explained by the well known waveguide theory, that fields extent more into the ambience and interact more

with material outside the cladding [124]. The propagation constant (thus the effective index) of the cladding mode increases with the refractive index of the surrounding medium. The propagation constant is also a nonlinear function of the surrounding medium. The change is more significant as the surrounding media has a refractive index approaching that of the fiber cladding.

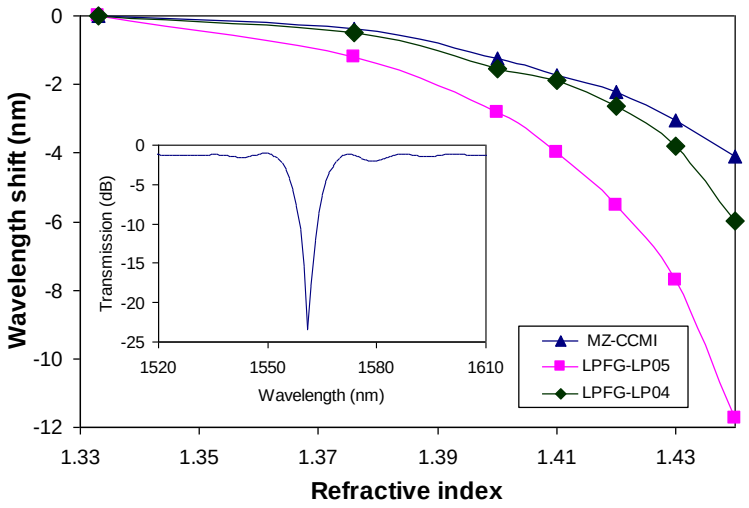

Figure 3.10 Wavelength shift as a function of refractive index in MZI and LPFG with cladding mode of LP_{05} and LP_{06} (Inset: LPFG transmission spectrum of LP_{05} mode).

We also compared the device with a LPFG in terms of refractive index measurement sensitivity. A LPFG fabricated by point-by-point CO_2 laser irradiations was used for comparison. The LPFG had a period of 525 μm, a length of 50 mm, and the resonance wavelength of 1561nm in air at room temperature. The transmission spectrum of the LPFG is shown in the insert of Fig. 3.10 and the resonance peak is resulted from light coupling from the core mode to the LP_{05} cladding mode. The shift in resonance wavelength of LPFG in response to the refractive index changes is shown in Fig. 3.10 The LPFG had a higher sensitivity than the MZI.

The resonance wavelength (λ_{res}) of a LPFG can be roughly estimated by the phase matching condition, Eq. (2.2). Accordingly, the relative effective refractive index change is proportional to the relative resonance wavelength, given by:

$$\frac{\Delta n_{cl}^{\ eff}}{n_{cl}^{\ eff}} = \frac{\Delta \lambda_{res}}{\lambda_{res}} \tag{3.5}$$

Compare Eqs. (3.4) and (3.5), one finds that a LPFG and an inline MZI operate based on the same mechanism that the propagation constant of the cladding mode is a function of the refractive index of the surrounding medium. The higher the order of the cladding mode, the more sensitive to ambient index change. From Fig. 3.10, we find that the sensitivity of the CCMI is smaller than LPFG-LP_{04} and LPFG-LP_{05}, but every close to LPFG-LP_{04}. This suggested that the order of the cladding mode excited in this CCMI was lower than but every close to LP_{04}. It is possible for the laser exposure to excite more than one cladding mode. However, the high-quality interference fringes of different interferometer lengths indicated that one cladding mode dominated.

3.4. CONCLUSIONS

To summarize, we report an inline MZI type CCMI device fabricated by 2-point CO_2 laser irradiations on a single mode fiber. High quality interference spectra with a fringe visibility of about 20 dB and an average background loss of about 12 dB were observed for four different interferometer lengths (5, 10, 20 and 40 mm). The device survived high temperatures up to 1100°C, indicating its supreme robustness for high temperature harsh environment applications. The inline MZI with a length of 5 mm has a temperature sensitivity of 0.0817 nm/℃ at lower temperatures and exhibits a non-linear behavior at higher temperatures. The device was also evaluated for refractive index measurement using various liquids. It was found that the sensitivity for refractive index measurement of the MZI was smaller than that of a LPFG of LP_{05} cladding mode, but very close to LP_{04} mode, indicating that the CO_2 laser irradiation mainly causes light coupling from the core mode to the low order cladding modes. The easy fabrication and simple structure make the device useful for monitoring refractive index changes.

4. FIBER INLINE CORE CLADDING MODE INTERFEROMETER SENSOR

This chapter reports a novel, assembly-free, optical fiber inline Fabry-Perot interferometer (FPI) with an open cavity fabricated by femtosecond (fs) laser ablation. Starting with a brief introduction to the optical fiber FPI device, the operating principle, sensing mechanism and signal processing methods of the device are described and the common device fabrication methods are reviewed. The fs laser based fabrication method and the quality of the device are then described in details. The high temperature survivability of the fabricated FPI device is experimentally evaluated. The device is used to measure the temperature-dependent refractive index of water, demonstrating its potential for chemical sensing.

4.1. INTRODUCTION

Among various interferometer based optical fiber sensors, FP interferometer (FPI) has drawn a great deal of research interest because the FPI-based fiber optic sensors provide many operational benefits in comparison with other configurations. For example, a serious issue associated with the conventional Mach-Zehnder and Michelson interferometers is the polarization-induced fading (PIF) which was initially identified as early as 1980 by Stowe et al. [125]. The problem originates from the fact that as the light is split into two separate paths in Michelson and Mach-Zehnder configurations, the state of polarization (SOP) of light guided in both fiber arms varies in an arbitrary and unpredictable manner. As a result, the SOPs of the recombined optical components from the two interferometer arms vary independently, leading to a suppression of the interfereometric optical mixing efficiency and a loss (“fading”) of the interference signal [126]. Sagnac interferometer suffers the same problem as well, either because SOP of light evolves differently as the light propagating in different directions in a Sagnac interferometer, although along the same fiber.

Fortunately, the PIF problem does not present in optical fiber inline FPI sensors, where the light interference occurs consist either of optical components with very short length (tens of micrometers) in which the SOP variations are negligible, or simply,

because the materials in the FP cavity (eg. air, vacuum or liquid phased medium) have little effect on polarization state as wave propagates through. In addition, different from the other three sensor interferometric configurations, where the sensing probe is an entire fiber arm, an optical FPI sensor takes the FP cavity (up to 300 μm) as the sensing element. This promises a very small structure and a much better spatial measurement resolution.

In the early stage, the optical fiber inline FPI sensor includes introducing "internal" mirrors in a SMF to form intrinsic FPI (IFPI) sensors by splicing two SMFs with one metal coated at the fiber end, where the fiber section in between the two metal mirrors serves at the FP cavity [127]. Later, the most widely reported FPI based sensor, developed at Virginia Polytechnic Institute and State University, is in the form of extrinsic FPI (EFPI), where the air gap in between two optical fiber endfaces functions as the FP cavity [128]. The sensors are simply fabricated by inserting two fibers into an alignment tube to form a FP cavity, with one as the lead-in/lead-out fiber to carry the light and the other as the sensing fiber. Later, various types of EFPI fiber optic sensors have been designed and implemented in the measurement of a variety of measurands, such as temperature [129], pressure [30, 130], strain [129, 131], magnetic field [132], flow [133], acoustic waves [134], and chemical and biological parameters [37, 133].

4.2. FPI PRINCIPLE

4.2.1. FPI Basics. Although the two reflectors forming the Fabry-Perot (FP) cavity can be the surfaces of any optical components, a very simple way of constructing a fiber FPI is to directly use the cleaved endfaces of two fibers as shown in Fig. 4.1. Typically, singlemode fibers are used because of their small numerical aperture (NA). The small NA results in a small divergence angle of the exiting beam as it passes through the cavity, which is preferable to produce a high quality interference signal. Multimode fibers have also been used for the construction of FPI sensors. The main reason of using a multimode fiber is to allow easy and efficient coupling from the light source to the fiber. As shown in Fig. 4.1, the incident light partially reflects (I_1) at the endface of the input fiber. The remainder of the light propagates across the cavity and partially reflects (I_2) at the endface of the reflect fiber. The two reflections interfere to generate a signal whose

phase is linearly proportional to the optical length of the cavity, defined as the product of the cavity length and the refractive index of the medium filling the cavity.

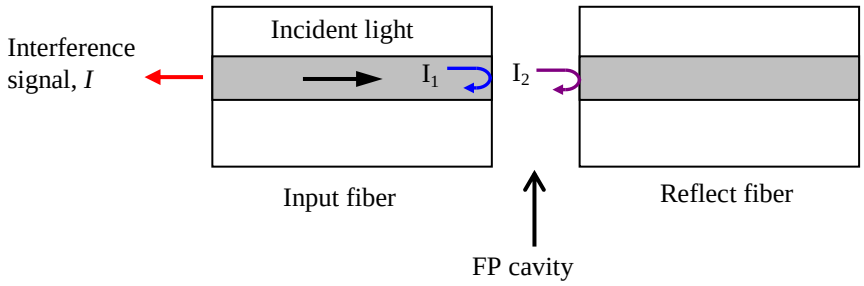

Figure 4.1 Illustration of a fiber FPI sensor

4.2.2. Sensing Mechanism. When the reflectivity of the two endfaces is low (e.g., 4% from an air-glass interface), the multiplex reflections in the cavity have negligible contribution to the optical interference. Under this circumstance, the FP cavity is commonly referred as to the low-finesse cavity and the signal can be modeled using a two-beam interference model, given by Eq. (2.15). The only difference here is that *OL* can be written as $OL = n \times L$, where n is the refractive index of the medium filling the FP cavity and L is the length of the cavity.

Eq. (2.15) indicates that the optical interference signal is a function of the length of the FP cavity. When used as a physical sensor (e.g., temperature, pressure, strain, etc.), the parameters to be measured change the length of the cavity which can be calculated based on the characteristics (e.g., phase, intensity and frequency) of the interference signal.

Accordingly, if the FP cavity is made accessible to the external environment, the device can be used as a chemical sensor by measuring the refractive index change of a liquid solution or a gas mixture filling the open cavity. A unique advantage of such sensor is that the phase of the interference signal is a linear function of the refractive index. Compared with other types of sensors, a fiber FPI refractive index sensor has the unique advantage of constant sensitivity over a large dynamic range.

4.3. SIGNAL PROCESSING

Eq. (4.1) states that the intensity of the interference signal is a periodic function of the cavity length, the refractive index and the wavelength. For most sensing applications, the interference signal needs to be processed to obtain either the absolute value or the relative change of the cavity length (or the refractive index) that is related to the physical (or chemical) environment of interest. Although many signal processing methods have been studied in the past, the white light interferometry method produces the highest accuracy.

White light interferometry commonly uses a broadband source to excite the interferometer and an optical spectrum analyzer (OSA) to record the interference signal in the spectral domain. Sometimes, a tunable laser is used to replace the broadband source and a regular photodetector is used to replace the OSA. The spectral signal is obtained by stepping the tunable laser over the entire available wavelength range. In either way, an interference spectrum can be obtained similar to that is given in Fig. 3.2(c).

4.3.1. Period Tracking Method. According to Eq. (3.1), the two adjacent interference minimums have a phase difference of 2π. That is

$$\left(4\pi Ln/\lambda_{v1}+\varphi_0\right)-\left(4\pi Ln/\lambda_{v2}+\varphi_0\right)=2\pi \tag{4.1}$$

where λ_{v1} and λ_{v2} are the wavelengths of two adjacent valleys (Fig. 3.2(c)) in the interference spectrum. The optical length of the FP cavity, defined as the product of the cavity length and the refractive index, can thus be found as

$$L\cdot n=\frac{1}{2}\frac{\lambda_{v1}\lambda_{v2}}{\lambda_{v2}-\lambda_{v1}} \tag{4.2}$$

In theory, Eq. 4.2 can be used to calculate either the absolute refractive index (n) or the absolute length (L) of the cavity if one of them is known. However, the

measurement based on Eq. 4.2 has a poor resolution because the period is not a sensitive function of the optical path change [89, 135].

In this study, the minimum detectable change in optical length of FP cavity (S_l) is defined as the standard deviation of the measurement uncertainty of the optical length of FP cavity. When λ_{v1} and λ_{v2} are assumed to be two independent random variables, S_l can be derived from Eq. (4.2) and expressed into:

$$S_l = \sqrt{(\frac{\partial l}{\partial \lambda_{v1}})^2 (S_{\lambda_{v1}})^2 + (\frac{\partial l}{\partial \lambda_{v2}})^2 (S_{\lambda_{v2}})^2} = \sqrt{\frac{{\lambda_{v1}}^4}{4(\lambda_{v2} - \lambda_{v1})^4} (S_{\lambda_{v1}})^2 + \frac{{\lambda_{v2}}^4}{4(\lambda_{v2} - \lambda_{v1})^4} (S_{\lambda_{v2}})^2} \quad (4.3)$$

in which $S_{\lambda 1}$ and $S_{\lambda 2}$ represent the standard deviations of the wavelength measurement of the two consecutive valleys, respectively. Determined from the performance specifications of a particular OSA instrument, $S_{\lambda 1}$ and $S_{\lambda 2}$ are equal or $S_{\lambda 1} = S_{\lambda 2} = S_\lambda$ since the instrument has consistent measurement accuracy of wavelength within the specified observation bandwidth. In addition, within a relatively small observation spectrum range, both λ_1 and λ_2 can be approximated by the center wavelength of the range, λ_0. As a result, Eq. (4.3) can be simplified into:

$$S_l \approx S_\lambda \frac{{\lambda_0}^2}{\sqrt{2}(\Delta\lambda)^2} \quad (4.4)$$

where $\Delta\lambda$ is the wavelength difference between the two consecutive valleys. For the estimation of measurement errors, $\Delta\lambda$ at a given cavity length can be considered as a constant within the wavelength bandwidth of observation though $\Delta\lambda$ increases with wavelength. In this case, Eqs. (4.2) and (4.4) indicate that the minimum detectable cavity length increases quadratically with cavity length as $\Delta\lambda$ decreases.

4.3.2. Phase Tracking Method. In many cases, only the relative refractive index change is of interest and the range of refractive index variation is small so the phase shift is less than 2π. In this case, the phase ambiguity issue can be avoided. The relative refractive index change can be calculated based on the spectral shift of the interferogram.

According to Eq. (4.1), the interference signal reaches its minimum (I_{min}) when the phase of the cosine term becomes an odd number of π. That is $I = I_{\min}$, when

$$4\pi n \cdot L / \lambda_v + \phi_0 = (2m+1)\pi \tag{4.5}$$

where m is an integer and λ_v is the center wavelength of the specific interference valley. In Eq. (4.5), taking the derivative of n with respect to λ_v, one finds:

$$dn / d\lambda_v = [(2m+1)\pi - \phi_0] / 4\pi L \tag{4.6}$$

Assuming the cavity length L is maintained constant during measurement, Eq. (4.6) indicates that the refractive index is a linear function of the valley wavelength, or the sensitivity of the FPI sensor is a constant. The amount of refractive index change (Δn) can thus be computed based on the wavelength shift ($\Delta\lambda_v$ as shown in Fig. 3.2(c)) of a particular interference valley using the following equation derived based on Eq. (4.6):

$$\Delta n = n \cdot \Delta\lambda_v / \lambda_v \tag{4.7}$$

where the relative refractive index change is directly proportional to the spectral shift of the interferogram. It is worth noting that Eq. (4.7) is also applicable to other characteristic spectral positions such as the interference peak and the center point of the interferogam (λ_c and $\Delta\lambda_c$ in Fig. 3.2(c) where the curve is relatively linear). The advantage of using the center point in calculation is that its spectral position can be resolved with a higher resolution compared to the valley or the peak that typically has a flat bottom or top. In addition, curve fitting of the interference fringe can also improve the measurement

accuracy. Since the minimum $\Delta\lambda_v$ can be represented by the instrument measurement accuracy or S_λ, the resolution of the phase tracking method decreases linearly with the cavity length.

Comparing Eqs. (4.4) and (4.7), one finds that Eq. 4.4 can be used to calculate the absolute FP cavity optical length while Eq. (4.7) only provides the relative change of the FP cavity optical length, or change of refractive index given a fixed physical length. However, the calculation based on Eq. (4.7) has a much higher resolution than that obtained using Eq. (4.4).

4.3.3. Interference Frequency Tracking Method. The spectral interferogram of an EFPI typically represents a harmonic function of wavenumber with a dominant frequency known as interference frequency. By taking the Fourier transform of such an interferogram, an approximate delta function of cavity length corresponding to the interference frequency is obtained [136]. The cavity length of the EFPI, *l*, can be calculated by:

$$l = \frac{n\pi}{\left(v_E - v_S\right)} \tag{4.8}$$

in which v_S and v_E are the wavenumbers of the starting and ending points of an observation bandwidth, respectively, and *n* is an integer representing the Fourier series index.

It can be easily observed from Eq. (4.8) that the minimum detectable cavity optical length change using spatial Fourier transform method is $\pi/(v_E - v_S)$ when $n=1$. For a light source with a spectrum width of 100 nm, the detectable cavity length change is approximately 12 μm. Given that the physical cavity length of an optical fiber inline FPI is 60 μm, optical length higher than 20% is able to be detected using this signal processing method. The measurement resolution then requires a broader bandwidth of the optical source, which can only be provided by limited equipment available in the market. As a result, this method would not be conducted in this research.

4.4. REVIEW OF EXISTING FPI SENSORS

4.4.1. Holey Sleeve Hosted FPI Sensor. The fiber FPI sensor illustrated in Fig. 4.2 can be fabricated by inserting two endface-cleaved optical fibers into a ferrule. The ferrule usually has a diameter slightly larger than that of an optical fiber to provide necessary alignment. After assembly, these components are bonded together to construct the FPI device. Over the years, the bonding methods have evolved from epoxy in the early days [137] to the more recent thermal fusion using a CO_2 laser [3] or an electric arc [138].

To minimize the temperature dependence and to improve the device robustness, fused glass ferrules have been used to construct the FPI cavity. Fig. 4.2 shows a fiber FPI device made by thermal fusion of two singlemode fibers into a fused silica tube using a CO_2 laser. The device has been demonstrated for temperature, pressure and strain sensing and successfully survived a high temperature (200°C) and high pressure (8000 psi) co-existing environment [30]. Later, a short section of micro fused silica tube, with an outer diameter of 126 μm and an inner diameter of 50 μm, was spliced between two cleaved singlemode fibers to construct the FPI sensor in which the tube served as a spacer [139].

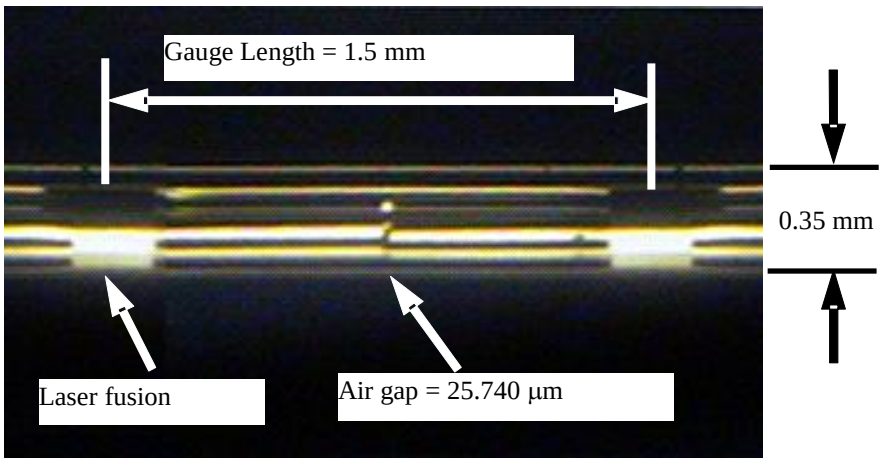

Figure 4.2 Microscopic image of a fiber FPI sensor made by thermal fusion.

In general the mciro-assembly methods involve complicated procedures of assembling multiple components together. The length of the cavity varies in each device,

and the performance is neither predictable nor controllable. The multiple parts assembly also compromises the robustness of the device owing to the limited strength of the joints. At high temperature, the CTE mismatch between different parts significantly affects the aimed signal, decreases the mechanical strength and possibly takes the FPIs apart under really extreme conditions.

The micro-assembly based fabrication processes commonly result in a sealed FP cavity [30, 129, 138, 139]. The applications of such sealed FPI sensor have been limited to the measurement of physical parameters such as displacement, temperature, strain, pressure, acoustic waves, and flow.

In order to make a FPI chemical sensor, the FP cavity needs to be made accessible by the analyte molecules. One way to achieve this is to use a holey sleeve to host the cavity. Xiao et al. [135] reported such a fiber FPI gas sensor formed by bonding two endface-polished fibers in a holey sleeve using epoxy. The holey sleeve allows gas to freely enter and leave the cavity. A resolution of 10^{-5} was estimated in monitoring the changes in the refractive index caused by varying the gas composition. However, the sensor assembly was complicated and required the use of epoxy. In addition, the various components used in sensor construction were made of different materials. As a result, the device had a strong dependence on temperature.

4.4.2. Multicavity FPI Sensor. Wang, et al. designed a fiber optic biosensor based on cascaded multiple FP cavities [139]. The fabrication process of the reported sensor is illustrated in Fig. 4.3. A silica capillary tube (50 mm inner diameter and 126 mm outer diameter) was spliced onto a single-mode fiber. An FP cavity was formed by cleaving the tube and splicing it to another single-mode fiber. An air cavity with the size down to 10mm could be achieved by cleaving under a microscope. Another fiber cavity was created by cleaving the second fiber as shown in Fig. 4.3. The fiber cavity could be as small as 10 mm, limited by cleaving, and up to the centimeter range, limited by the coherence length of the laser to interrogate the sensor. The overall fringe pattern as shown in Fig. 4.4 was due to the interference between the reflection signals from the three reflection interfaces. Multiple-beam interference was evaluated by matrix formalism.

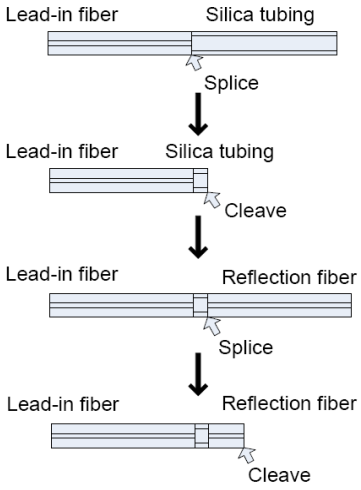

Figure 4.3 Fabrication procedures of a multicavity fiber FPI sensor

The developed sensor was used for ultrathin-film measurement. The reflection spectrum was shifted during the deposition of thin films (e.g. self-assembly of polyelectrolyte layers) onto the sensor end. The reflection between the thin film and the fiber endface was neglected because of their similar refractive indices. As the film increased its thickness, the length of the fiber cavity changed. The amount of change was estimated by the phase shift of the interferogram. The device could also be used as an immunosensor in which the optical thickness changes were used to evaluate the immobilization of the IgG and the immunological activities of the immobilized layers. The binding of IgG and the corresponding antigen was observed, and the nonspecific binding characteristics were investigated.

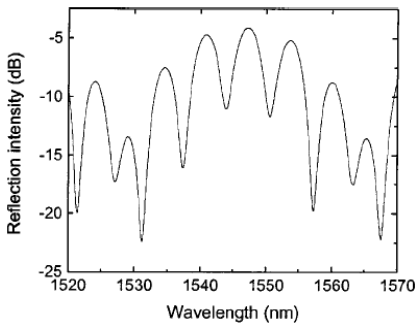

Figure 4.4 Reflection spectrum of a multicavity FPI sensor

4.4.3. FP Modulated Tip Sensor. Recently, Ran et al. described a refractive index sensor by adding a sealed Fabry-Perot cavity near the tip of a single-mode fiber [140]. To fabricate the sensor head, a circular hole was produced using a 157-nm laser micromachining system. The cleaved endface of the PCF was exposed directly to the focused laser beam of a 157 nm pulsed laser (Coherent, LPF202). The pulse energy density, pulse width, and pulse repetition rate used were 12 J/cm^2, 15 ns, and 20 Hz, respectively. As a result of the focused exposure, a circular hole was formed at the center of the cross section, with a depth of ~23 μm and a diameter of ~56 μm, as shown in Fig. 4.5(a),. A total of 160 pulses were used to produce the hole, which took only 8 seconds to complete. The micromachined hole was then spliced to another fiber to form a sealed FP cavity. Finally, the spliced fiber was cleaved at a short distance from the air cavity to complete the sensor as shown in Fig. 4.5(b). The length of the air cavity was 29 μm and the distance from the air cavity to the fiber end was 1014 μm.

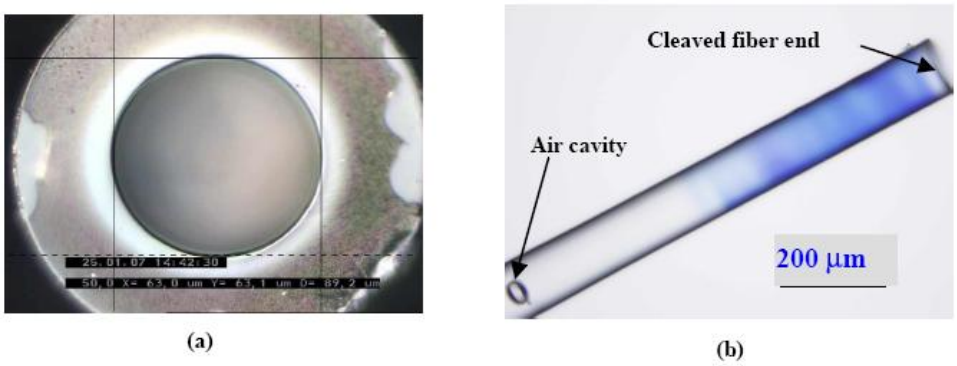

Figure 4.5 (a) Microscopic image of the micro-machined hole introduced on the fiber cross-section. (b) Microscopic image of the fabricated sensor head.

In this structure, the sealed FPI itself was not a sensing device but only served as a signal modulator. The external refractive index variation changed the reflectivity of the exposed fiber tip. The amount of refractive index change was determined by change in the maximum fringe contrast in the reflected spectrum. The sensor head was dipped into a glycerin solution (for $n < 1.45$) or a solution of carbon bisulfide (CS_2) and alcohol (for $1.45 < n < 1.62$). The refractive index of the solution was controlled by changing the concentration of the solvent. The reflection spectrum of the sensor in air is shown in Fig. 4.6(a). A close-up of the fringes is shown in Fig. 4.6(b) for several values of RI: 1.0 (air),

1.33 (water), and 1.404 (glycerin solution). The resolution of RI measurement was estimated to be ~4×10^{-5} in its linear operating range.

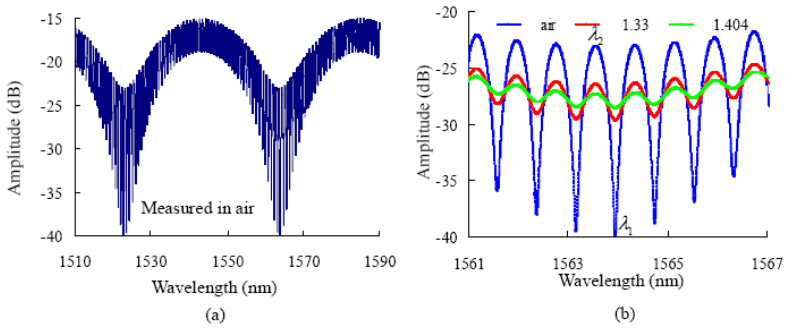

Figure 4.6 (a) Reflection spectrum of the sensor measured in air. (b) Close-up displays of the fringes for n_2 = 1.0 (air), 1.33, and 1.404, respectively.

4.5. OPEN CAVITY FPI SENSOR FABRICATED BY FEMTOSECOND LASER MICROMACHINING

4.5.1. Introduction of Femtoseond Laser Micromachining. The latest advancement in femtosecond (fs) based micromachining technology has opened a new window of opportunity for fabrication of micro-devices. Direct exposure of most solid materials (including fused silica glass) to high power fs laser pulses may lead to the ablation of a thin layer of materials at the laser focal point [141]. Due to the muliphoton nature of the laser-material interaction, the ablation process can be conducted on the material surface as well as within its bulk. As a result, true three-dimensional (3D) micro photonic devices can be fabricated with sub-micron accuracy [141, 142]. Optical device examples include microlenses [143], microfluidic channels [144], and fiber inline FPI [90, 140, 145, 146]. In this work, we demonstrated an inline FPI device with a fringe visibility of 16 dB by fs laser one-step micromachining a micro-notch on a single-mode fiber [90, 146].

4.5.2. Fabrication Setup and Procedure. The device fabrication was carried out using a home-integrated fs laser 3D micromachining system as schematically shown in Fig. 4.7. The repetition rate, center wavelength and pulse width of the fs laser (Legend-F, Coherent, Inc.) were 1kHz, 800 nm and 120 fs, respectively. The maximum output

power of the fs laser was approximately 1 W. The actual laser power used in fabrication was reduced to about 20 mW by using the combination of waveplates, polarizers, and several neutral density (ND) filters. The attenuated laser beam was directed into an objective lens with a numerical aperture (NA) of 0.45 and focused onto the single mode optical fiber (Corning SMF 28) mounted on a computer-controlled five-axis translation stage with a resolution of 1μm.

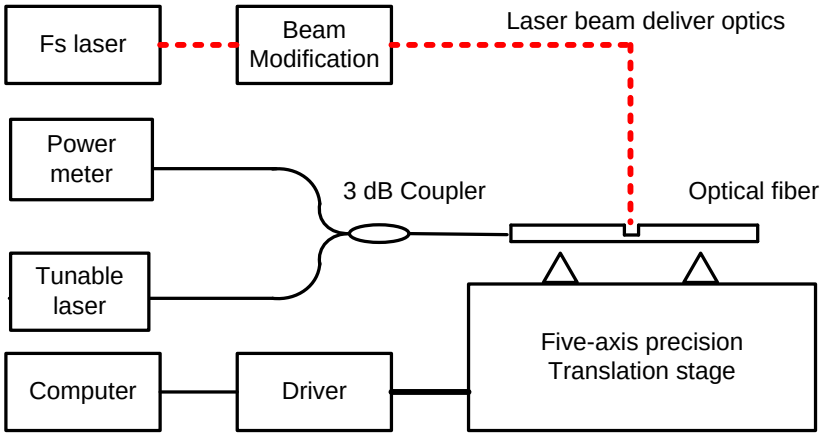

Figure 4.7 Fiber inline FPI device fabrication using an fs laser

During fabrication, the interference signal of the fiber FP device was continuously monitored. A tunable laser source (HP 8168E) was connected to one of the input ports of the 3 dB fiber coupler. The output port of the coupler was connected to the device under fabrication. Controlled by the computer, the tunable laser continuously scanned through its wavelength range (1475-1575nm) at the rate of 1 nm per step. The signal reflected from the device at each wavelength step was recorded by an optical power meter (Agilent 8163A). The fabrication was stopped after a well-formed interference pattern was recorded.

4.6. FEATURES OF FS LASER FABRICATED OPTICAL FIBER INLINE FPI

Fig. 4.8 shows the schematic structure and scanning electron microscope (SEM) images of the fabricated fiber FP device, where Fig. 4.8(b) shows that a micro-notch was formed on the optical fiber. Fig. 4.8(c) shows the fs laser ablated surface. The cavity

length was about 60 μm as estimated from the SEM image. The depth of ablation was around 72 μm, just passing the fiber core. The FP cavity can be made very close (within a few hundreds of microns) to the end of the fiber. With such a short bending arm, the chance of bending induced device breakage is small.

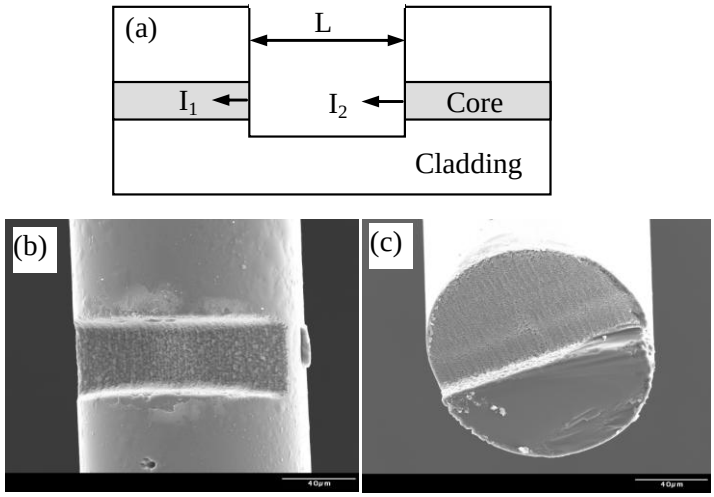

Figure 4.8 Schematic and SEM images of a fiber inline FPI device fabricated by fs laser

Fig. 4.9 shows the interference spectrum of an inline fiber FPI device fabricated by the fs laser. The excess loss of this particular device was about 16 dB. This relatively high loss was mainly caused by three reasons: 1) the light scattering loss at the laser-ablated surface, 2) the non-perpendicular surface orientation with respect to the fiber axis, which was partially evidenced by the non-flat interference peak intensities shown in Fig. 2, and 3) the coupling loss as a result of recoupling the light reflected from the second endface of the FP cavity back into the fiber core. The surface roughness can be reduced by reducing the laser scanning steps, of course, at the expense of a long device fabrication time. The non-perpendicular surface orientation can also be minimized by careful adjustment of the stages. The coupling loss increases with the length of the FP cavity. As a result, it may eventually limit the practical length of the cavity. Nevertheless, the interference spectrum indicated a high fringe visibility, exceeding 14 dB, which is sufficient for most sensing applications.

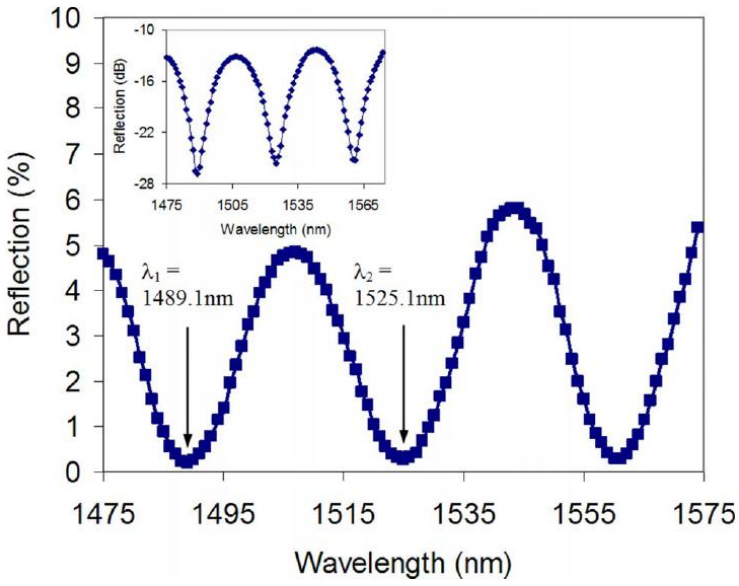

Figure 4.9 Interference spectrum of the fs laser fabricated fiber inline FPI device. Insert: interference fringe plotted in dB scale.

The optical length of the FP cavity can thus be found by applying Eq (4.2). We calculated that the FPI cavity length was 30.8 μm, which was very close to the length estimated by SEM imaging. Given the valley measurement uncertainty of 0.2 nm (Tunable laser's absolute accuracy value from datasheet), by implementing Eq. (4.4), we figured that the tolerance of the FPI cavity length measurement equals to 250 nm. Then, the cavity length of the optical fiber inline FPI is rewritten as 30.8 ± 0.25 μm.

4.7. APPLICATIONS OF FS LASER FABRICATED FIBER INLINE FPI

The device has an all-glass structure and does not involve assembly of multiple components. As a result, we expect that the device will have very small temperature dependence. In addition, the open micro-notch FP cavity allows prompt access to gas or liquid samples for direct refractive index measurement, making it possible to be used as an ultra-compact chemical sensor based on refractive index measurement.

4.7.1. Temperature Dependence. The fabricated device was tested for its ability to survive high temperatures. The sensor was placed in a programmable electric tubular furnace. The temperature of the furnace was increased from room 50°C to

1100°C (limited by the highest temperature of the furnace used) at a step of 50°C and the interference spectra at these temperatures were recorded using a similar interrogation system as shown in Fig. 1. However, to improve the accuracy, we replaced the tunable laser with a broadband source made by multiplexing a C-band and an L-band Erbium doped fiber ASE (amplified spontaneous emission) sources. The interference fringe reflected from the device was recorded by an optical spectrum analyzer (OSA, HP 70952B).

The cavity length as a function of the temperature is plotted in Fig. 4.10, where it increased nearly linearly following the increase of temperature. The fiber FP device successfully survived high temperatures up to 1100°C. However, as temperature increased to 1100°C, the interference fringe visibility was dropped by about 2dB compared to that at room temperature. The temperature sensitivity of this particular FP device was estimated to be 74 pm/°C based on the linear fit of the measurement data. The thermal test was repeated several times and the results were quite reproducible. The equivalent CTE of the fiber FP device was 2.4×10^{-6} /°C, which was about four times larger than the known CTE of the fiber cladding (fused silica, 5.5×10^{-7} /°C). Therefore, we concluded that the large device CTE was mainly caused by the thermally induced bending of the asymmetric FP structure, partially evidenced by the decreasing interference visibility at high temperatures.

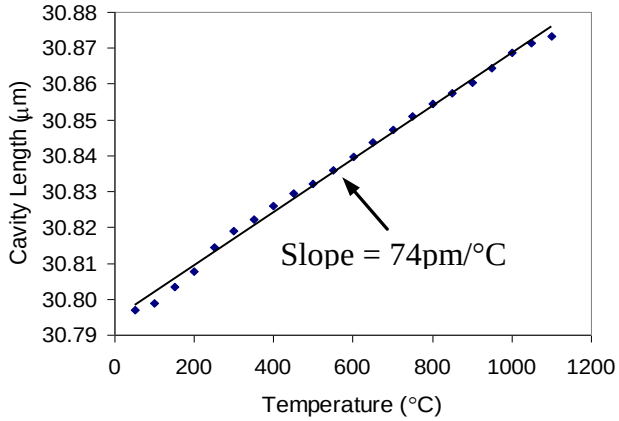

Figure 4.10 Optical fiber inline FPI cavity length as a function of temperature

4.7.2. Absolute Refractive Index Measurement. To evaluate its capability for refractive index measurement, the fiber FPI device was tested using various liquids including methanol, acetone and isopropanol at room temperature (25 ℃). The interrogation of the optical fiber inline FPI sensor is schematically shown in Fig. 4.11. A broadband source made by multiplexing a C-band (AFC, BBS-1550A-TS) and an L-band (Highwave, HWT-BSL-P) erbium-doped fiber amplified-spontaneous-emission (ASE) source was used to excite the device through a 3 dB fiber coupler. The reflected interference signal from the sensor was detected by an optical spectrum analyzer (OSA, HP70952B). The spectral resolution bandwidth of OSA was set to 0.5 nm and 1600 data points were obtained per OSA scan.

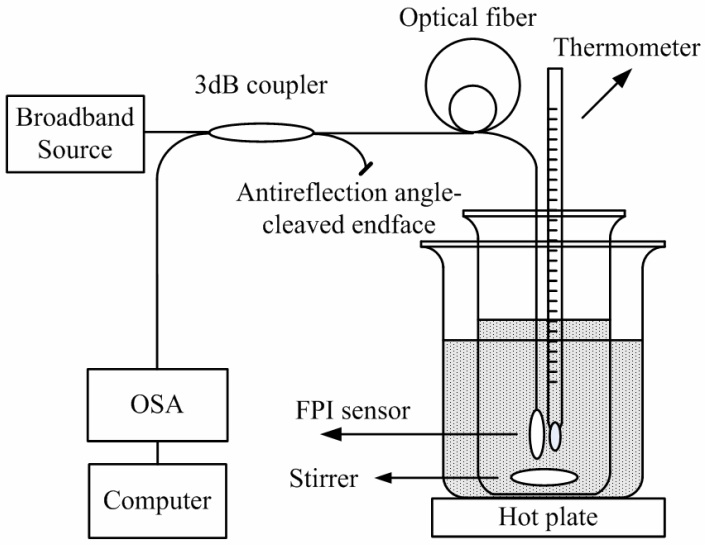

Figure 4.11 Experimental setup for the refractive index measurement

The interference spectrum of the fabricated device in air at room temperature is shown in Fig. 4.12. The loss of this particular device was about 20 dB higher than that of a FPI formed by cleaved fiber endfaces. The interference spectrum indicated a fringe visibility of about 5 dB, which was sufficient for most sensing applications. The length of the FPI cavity was found to be 63.1 μm using Eq. (4.2) with n set to be 1.0003 for air at the wavelength of 1550 nm [147]. Assuming the valley wavelength measurement uncertainty is 0.2 nm. It is worth noting that although the spectral resolution bandwidth is

0.5 nm, the large number of sampling points provides a good spectral accuracy. After applying Eq. (4.3), the length measurement uncertainty for this FPI is 0.88 μm, hence, the length is rewritten as 63.1 ± 0.88 μm.

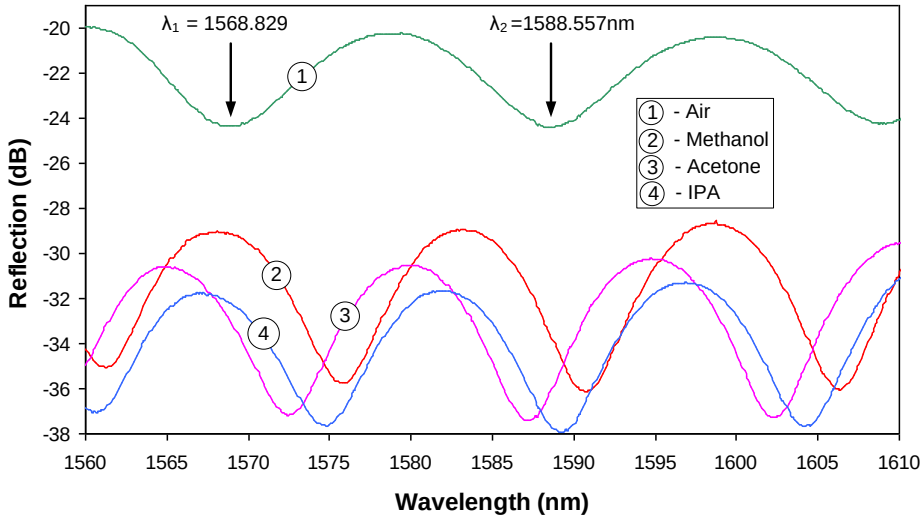

Figure 4.12 Interference spectra of the FPI device in air, methanol, acetone and isopropanol.

To evaluate its capability for refractive index measurement, the optical fiber FPI device was tested using various liquids including methanol, acetone and isopropanol at room temperature. The interference spectra of the device immersed in various liquids are also shown in Fig. 4.12 for comparison. The signal intensity dropped when the device was immersed in liquids as a result of the reduced refractive index contrast and thus lower Fresnel reflections from the cavity endfaces. However, the interference fringes maintained a similar visibility. The spectral distance between the two adjacent valleys also decreased, indicating the increase of refractive index of the medium inside the cavity. Using Eq. (4.2), the refractive indices of the liquids were calculated to be: $n_{methanol}$ = 1.328, $n_{acetone}$ = 1.358, and $n_{isopropanol}$ = 1.374, which were close to the commonly accepted values, 1.329, 1.36 and 1.377 for methanol, acetone and isopropanol in the near infrared wavelength range, respectively. To evaluate the measurement error, Eq. (4.3) was used to investigate the error propagation from the interrogation equipment. It was

found that the equipment contributed refractive index uncertainty is around 4×10^{-4}. It is worth noting that the some of the documented refractive indices have values beyond this uncertainty bar, due to the reason that the refractive index of liquid phased medium has a strong dependence on temperature. Also, the purity of the solution we purchased may vary gradually after a period of time.

4.7.3. Relative Refractive Index Measurement. The device was also evaluated for temperature-insensitive refractive index sensing by measuring the temperature-dependent refractive index of deionized water. Figure 4.13 shows the measured refractive index of deionized water as a function of temperature. As the temperature increases, the interference fringe shifts to a shorter wavelength indicating the decrease in its refractive index. The refractive index change was calculated using Eq. (4.7), by tracing the spectral shift of the interferogram, assuming a constant cavity length over the entire temperature range. To improve the accuracy of spectral shift measurement, the interference fringes were first normalized to have the same average intensities, then curve-fitted using a fourth-order polynomial. The spectral shift was computed as the difference in wavelength between the two fitted curves at the center point.

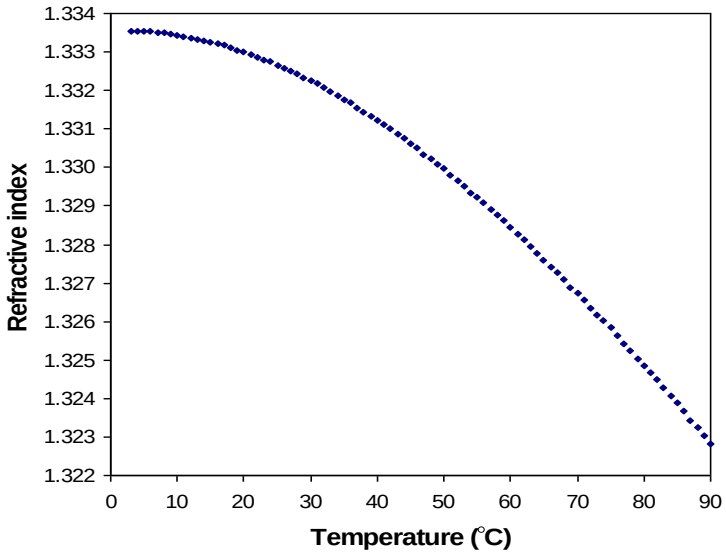

Figure 4.13 Measured refractive index of deionized water as a function of temperature

The measurement results, as shown in Fig. 4.13, indicate that the refractive index of water decreases nonlinearly as its temperature increases. The amount and shape of the measured refractive index of water change as a function of temperature agreed well with the previously reported measurement data [148]. When used to monitor the relative refractive index change of water with a nominal refractive index of 1.333, the sensitivity of measurement is 1163 nm/RIU at the wavelength of 1550 nm according to Eq. (4.7). The actual detection limit depends on the resolution with which the spectral shift of the interferogram can be determined. If a resolution of 0.10 pm is achieved in the determination of interferogram shift, a detection limit of 8.6×10^{-6} RIU is attainable. With a rough resolution of 1 nm, the detection limit of 8.6×10^{-4} RIU can still be achieved.

The above measurement results also included the error contribution of the temperature cross-sensitivity of the device. From Fig. 4.10, the temperature dependence of the device was 74 pm/°C. Based on Eq. (4.7), the temperature cross-sensitivity of the device was less than 4.8×10^{-5} RIU/°C. Therefore, the accumulated temperature cross-sensitivity induced measurement error was about 4.2×10^{-3} RIU at 87 ℃. The temperature dependence of the device was small at lower temperatures and contributed about 4% to the total refractive index variation at the highest temperature. Temperature compensation scheme would be necessary at higher temperatures.

4.8. CONCLUSIONS

To summarize, a novel fiber inline FP device with an accessible cavity was fabricated by one-step fs laser micromaching. Although the roughness of the laser ablated surfaces introduced a considerable background loss, the fringe visibility of the device was high enough for most sensing applications. The device successfully survived high temperatures up to 1100°C. The device may be directly utilized for temperature sensing or strain monitoring in harsh environments. The unique accessible FP cavity makes it attractive to develop ultra-compact chemical sensors based on refractive index measurement.

The miniaturized fiber inline FPI device was also demonstrated for highly sensitive refractive index measurement. The device was evaluated for refractive index measurement of various liquids and the results matched well with the reported data. The

inline fiber FPI was also tested to measure the temperature-dependent refractive index of deionized water from 3 to 87 ℃ with a sensitivity of 1163 nm/RIU. The temperature cross-sensitivity of the device was less than 4.8×10^{-5} RIU/ ℃. The small size, all-fiber inline structure, small temperature dependence at lower temperature, linear response, high sensitivity, and most attractively, an open cavity that is accessible to the external environment, make the new fiber inline FPI an attractive refractive index sensor that has many applications in chemical and biological sensing, especially under high temperature harsh environment.

5. SUMMARY AND FUTURE WORK

5.1. BRIEFLY SUMMARIZE THE DISSERTATION WORK

Harsh environments are commonly seen in modern industry where various high performance and miniaturized sensors are demanded for in situ process monitoring and optimization. These harsh environments can be characterized by the combination of high temperature, high pressure, corrosive/erosive atmosphere, and strong EMI. However, currently available sensors have difficulty to survive and operate in these extreme conditions. This situation suggests that innovative research is required to fill the capability gaps.

With the unique advantages of temperature tolerance, small size, resistance to corrosion/erosion, immunity to EMI, and capability of multiplexing and remote interrogation, optical fiber sensors are attractive for sensing and monitoring applications under the otherwise-inaccessible extreme conditions. However, there exist a number of unsolved issues in most existing optical fiber sensors that are commonly fabricated based on assembly of multiple components. These assembly-based fiber sensor probes have shown shortcomings for harsh environment applications, including structural and mechanical deterioration resulted from CTE mismatch, false signal induced by large temperature cross sensitivity, and high-cost due to the complicated fabrication processes.

Motivated by the needs for embedded sensors for harsh environment applications, this work focuses on design, development and demonstration of robust, miniaturized fiber sensor probes for harsh environment applications through assembly-free, laser fabrication. Towards this objective, the dissertation explored three types of fiber inline microsensors fabricated by two types of laser systems. Using a CO_2 laser, long period fiber grating (LPFG) and core-cladding mode interferometer sensors were fabricated. Using a femto-second laser, an extrinsic Fabry-Perot interferometric (EFPI) sensor with an open cavity was fabricated. The scope of the dissertation work consists of device design, device modeling/simulation, laser fabrication system setups, signal processing method development, and sensor performance evaluation and demonstration.

The dissertation presented our work on development, fabrication and demonstration of LPFGs made by CO_2 laser irradiation. LPFGs have grating period much

longer than the optical wavelength. The periodic refractive index modulation in an LPFG enables mode coupling from the forward propagating core mode to the discrete cladding modes. The mode-coupling is a function of various environmental parameters such as the temperature, period, and refractive index of the ambient medium. As a result, LPFGs can be used physical and chemical sensors. Traditional LPFG fabrication methods include UV exposure. However the UV light induced refractive index modulation cannot survive a high temperature. In this dissertation, LPFGs were fabricated by point-by-point shooting CO_2 laser pulses on an optical fiber from the side. The refractive index along the LPFG is changed as a result of laser irradiation based on the stress release effect. Such fabrication technique is supreme to the conventional UV exposure method for the reason that the CO_2 laser inscribed grating is capable to survive a temperature as high as 1000 ℃, making it possible to serve as high temperature, harsh environment sensor. High qualify LPFGs of various cladding modes (LP_{05} through LP_{09}) were successfully fabricated using the established automated grating fabrication station. By tuning the grating period of LPFG, we were able to fabricate LPFGs of various cladding modes with resonance peaks in the communication wavelength regime. Characterizations of these gratings indicated that higher cladding mode coupled resonances were more sensitive to both the temperature and ambient refractive index.

An analytical device model of the LPFG was developed based on coupled mode theory. A simulation tool was also developed based on the transfer matrix method. In order to better guide the fabrication of LPFG, the CO_2 laser exposure induced refractive index changes inside an optical fiber was measured using optical interferometry and studied as a function of the laser power and pulse duration. The measured index modulation parameters were then plugged into the analytical device model and the simulation result agreed well with the experimental results in terms of LPFG transmission characteristics. Our measurement results also indicated that that the CO_2 laser modification actually decreased the refractive index in an optical fiber.

High temperature survivability and stability of the fabricated LPFGs were experimentally investigated. A thermal shock method was proposed and verified to improve the LPFG high temperature stability. In addition, three sensing applications of LPFGs were demonstrated. Uncoated LPFGs have been used for measurement of ambient

refractive index changes. The higher order LPFGs have shown higher sensitivity towards refractive index changes. Pd thin film coated LPFGs were used to measurement H_2 concentration at elevated temperatures. Zeolite coated LPFG were also demonstrated for highly sensitive detection of trace chemicals.

An assembly-free inline MZI type core-cladding-mode interferometer (CCMI) fabricated by controlled 2-point CO_2 laser irradiations on a single mode fiber was reported. High quality interference spectra with a fringe visibility of about 20 dB and an average background loss of about 12 dB were observed for four different interferometer lengths (5, 10, 20 and 40 mm). The miniaturized CCMI device successfully survived high temperatures upto 1100°C, indicating its capability for high temperature harsh environment sensing. The inline MZI with a length of 5mm has a temperature sensitivity of 0.0817 nm/℃ at lower temperatures and exhibits a non-linear behavior at higher temperatures. The device was also evaluated for refractive index measurement using various liquids. It was found that the sensitivity for refractive index measurement of the MZI was smaller than that of a LPFG of LP_{05} cladding mode, but very close to LP_{04} mode, indicating that the CO_2 laser irradiation mainly causes light coupling from the core mode to the low order cladding modes. The easy fabrication and simple structure make the device useful for many potential sensing applications, especially those involved high temperature harsh environments.

Lastly, a novel, assembly-free fiber inline FP device with an accessible cavity was proposed and fabricated by one-step fs laser micromaching. Although the roughness of the laser ablated surfaces introduced a considerable background loss, the fringe visibility of the device was high enough for most sensing applications. The device successfully survived high temperatures up to 1100 ℃. The device may be directly utilized for temperature sensing or strain monitoring in harsh environments. The unique accessible FP cavity makes it attractive to develop ultra-compact chemical sensors based on refractive index measurement.

The miniaturized open-cavity FPI device was demonstrated for highly sensitive refractive index measurement. The device was evaluated for refractive index measurement of various liquids and the results matched well with the reported data. The inline fiber FPI was also tested to measure the temperature-dependent refractive index of

deionized water from 3 to 87 ℃ with a sensitivity of 1163 nm/RIU. The temperature cross-sensitivity of the device was less than 4.8×10^{-5} RIU/ ℃. The small size, all-fiber inline structure, small temperature dependence at lower temperature, linear response, high sensitivity, and most attractively, an open cavity that is accessible to the external environment, make the new fiber inline FPI an attractive refractive index sensor that has many applications in chemical and biological sensing, especially under high temperature harsh environment.

5.2. INNOVATION/CONTRIBUTIONS

The major scientific and technical merits of this work include:

1) For the first time, an inteferometric method was investigated to measure the refractive index change in an optical fiber core caused by CO_2 laser exposure. The interferometry based method had shown high measurement accuracy and our measurement results confirmed that the CO_2 laser modification decreased the optical fiber core refractive index. Together with the developed device model, the measurement results provided the guidance for optimal sensor design and fabrication.

   The developed interferometric method can also be applied to measurement of refractive index changes induced by other lasers (e.g., an fs laser). As laser based methods gaining their popularity in optical device fabrications, our fundamental study on accurate characterization of laser induced optical refractive index change could inspire other researchers to study laser material interactions for device design and fabrication process optimization.

2) A novel CCMI sensor structure was successfully fabricated by controlled CO_2 laser irradiations. The device survived high-temperature tests upto 1100°C. The excited cladding modes in the CCMI structure were experimentally determined. The device was also successfully demonstrated for refractive index measurement. The simple and solid structure of the CCMI platform may promise many potential sensing applications which are yet to be explored in the future.

3) An optical fiber inline EFPI senor with an open cavity was successfully fabricated using femtosecond laser ablation. The assembly-free fabrication prevents the

sensor from being affected from CTE mismatch caused mechanical deterioration, making it more robust for high temperature sensing applications. The sensor survived high temperatures upto 1100°C. The open-cavity FPI sensor was also successfully demonstrated for highly sensitive monitoring of ambient refractive index change. With many unique advantages such as small size, negligible temperature cross-sensitivity, and linear response toward refractive index changes, the assembly-free, open cavity FPI sensor may find many applications in chemical and biological sensing, especially under high temperature harsh environment.

5.3. PUBLICATIONS DURING THE DISSERTATION WORK

Papers with asterisk symbol are related to this work.

1. Y. Huang, T. Wei, Z. Zhou, Y. Zhang, G. Chen, and H. Xiao, "An extrinsic Fabry–Perot interferometer-based large strain sensor with high resolution " Meas. Sci. Technol. **21**, 105308 (2010).
2.* C. Eggen, Y. S. Lin, T. Wei, and H. Xiao, "Detection of lipid bilayer membranes formed on silica fibers by double-long period fiber grating laser refractometry " Sensors and Actuators B: Chemical **Article in Press**.
3.* Y. Han, T. Wei, H.-L. Tsai, and H. Xiao, "Measurement of refractive index change of optical fiber core induced by femtosecond laser scanning," Optical Engineering **49**, 064301-064304 (2010).
4. Z. Yinan, L. Yanjun, W. Tao, L. Xinwei, H. Ying, G. Chen, and X. Hai, "Fringe Visibility Enhanced Extrinsic Fabry-Perot Interferometer Using a Graded Index Fiber Collimator," Photonics Journal, IEEE **2**, 469-481 (2010).
5.* X. Wei, T. Wei, J. Li, X. Lan, H. Xiao, and Y. S. Lin, "Strontium cobaltite coated optical sensors for high temperature carbon dioxide detection," Sensors and Actuators B: Chemical **144**, 260-266 (2010).
6. Y. Han, X. Lan, T. Wei, H.-L. Tsai, and H. Xiao, "Surface enhanced Raman scattering silica substrate fast fabrication by femtosecond laser pulses," Applied Physics A: Materials Science & Processing **97**, 721-724 (2009).
7. X. Lan, Y. Han, T. Wei, Y. Zhang, L. Jiang, H.-L. Tsai, and H. Xiao, "Surface-enhanced Raman-scattering fiber probe fabricated by femtosecond laser," Opt. Lett. **34**, 2285-2287 (2009).
8.* T. Wei, X. Lan, and H. Xiao, "Fiber inline core-cladding-mode Mach-Zehnder interferometer fabricated by two-point CO_2 laser irradiations," IEEE Photonics Technology Letters **21**, 669-671 (2009).
9.* J. Zhang, X. Tang, J. Dong, T. Wei, and H. Xiao, "Zeolite thin film-coated long period fiber grating sensor for measuring trace organic vapors," Sensors and Actuators, B: Chemical **135**, 420-425 (2009).
10.* Y. Li, T. Wei, J. A. Montoya, S. V. Saini, X. Lan, X. Tang, J. Dong, and H. Xiao, "Measurement of CO_2-laser-irradiation-induced refractive index modulation in

single-mode fiber toward long-period fiber grating design and fabrication," Applied Optics **47**, 5296-5304 (2008).
11.* J. Zhang, X. Tang, J. Dong, T. Wei, and H. Xiao, "Zeolite thin film-coated long period fiber grating sensor for measuring trace chemical," Optics Express **16**, 8317-8323 (2008).
12.* T. Wei, Y. Han, H. L. Tsai, and H. Xiao, "Miniaturized fiber inline Fabry-Perot interferometer fabricated with a femtosecond laser," Optics Letters **33**, 536-538 (2008).
13.* T. Wei, Y. Han, Y. Li, H. L. Tsai, and H. Xiao, "Temperature-insensitive miniaturized fiber inline Fabry-Perot interferometer for highly sensitive refractive index measurement," Optics Express **16**, 5764-5769 (2008).
14.* X. Wei, T. Wei, H. Xiao, and Y. S. Lin, "Nano-structured Pd-long period fiber gratings integrated optical sensor for hydrogen detection," Sensors and Actuators B: Chemical **134**, 687-693 (2008).
15.* Hai Xiao and Tao Wei, Chapter 7 *Miniaturized Optical Fiber Inline Interferometers for Chemical Sensing*
X. Fan, *Advanced photonic structure for biological and chemical detection* (Springer, New York; London, 2009).

5.4. FUTURE WORK

The future work recommendations for each device are listed below:

LPFG fabricated by CO_2 laser irradiation

1) Although the wavelength drift under extreme temperatures can be suppressed by thermal shock method, the mechanism behind this phenomenon has not been fully unveiled. The understanding of this effect can help optimize this thermal treatment procedure and LPFG with better thermal stability is expected.
2) Also, temperature cross-sensitivity is still restricting us from acquiring more accurate signal. It is known that by placing a temperature sensor head-to-head with the LPFG, it may compensate the temperature induced signal. However, this approach will involve tremendous extra work when dealing with hundreds of sensing probes. A self-compensated or temperature insensitive LPFG device is desired to get better performance.
3) The signal processing technique employed currently is mainly based on curve fitting. Because in most cases, researchers are more interested in the relative position of the resonance peak. A waveform cross-correlation technique may

be useful to acquire better measurement accuracy and evidently suppress the noise signal.

4) Various functional material coatings with good selectivity are anticipated to broaden its application fields.

CCMI fabricated by CO_2 laser exposure

1) The combination of cladding modes is still an issue that limits its development as a real sensor. The different sensitivities of different cladding modes significantly deteriorate the signal quality. The sensitivity between different devices made under same condition varies evidently. A novel signal processing method is needed to eliminate the multimode interference induced device uncertainty.
2) Same as LPFG, various functional material coatings with good selectivity are anticipated to broaden its application fields.

FPI fabricated by fs laser ablation

1) The surface quality of the FP cavity fabricated by fs laser is desired to be improved to obtain better signal strength. The improvement approaches may include post thermal treatment, high power laser reflow or fine polishing using fs laser with much smaller energy.
2) By cascading intrinsic and extrinsic FP cavities, the structured fiber probe may achieve multi-parameter sensing capability.

BIBLIOGRAPHY

1. R. J. Bates and I. ebrary, *Optical switching and networking handbook* (McGraw-Hill, New York, 2001).
2. J. Hecht, *City of light : the story of fiber optics*, The Sloan technology series (Oxford University Press, New York, 1999).
3. B. Lee, "Review of the present status of optical fiber sensors," Optical Fiber Technology **9**, 57-79 (2003).
4. N. Lagakos, J. A. Bucaro, and J. Jarzynski, "TEMPERATURE-INDUCED OPTICAL PHASE SHIFTS IN FIBERS," Applied Optics **20**, 2305-2308 (1981).
5. A. B. Tveten, A. Dandridge, C. M. Davis, and T. G. Giallorenzi, "FIBRE OPTIC ACCELEROMETER," Electronics Letters **16**, 854-856 (1980).
6. D. Chen, W. Liu, M. Jiang, and S. He, "Strain sensor system based on a high finesse fiber Bragg grating fabry-perot cavity," in 2008),
7. A. P. Abel, M. G. Weller, G. L. Duveneck, M. Ehrat, and H. M. Widmer, "Fiber-optic evanescent wave biosensor for the detection of oligonucleotides," Analytical Chemistry **68**, 2905-2912 (1996).
8. H. Y. Fu, H. Y. Tam, L. Y. Shao, X. Dong, P. K. A. Wai, C. Lu, and S. K. Khijwania, "Pressure sensor realized with polarization-maintaining photonic crystal fiber-based Sagnac interferometer," Applied Optics **47**, 2835-2839 (2008).
9. T. Wei, Y. Han, H. L. Tsai, and H. Xiao, "Miniaturized fiber inline fabry-p érot interferometer for chemical sensing," in 2009),
10. S. Kuehn, F. Bomholt, and N. Kuster, "Miniature electro-optical probe for magnitude, phase and time-domain measurements of radio-frequency magnetic fields," in 2010 Asia-Pacific Symposium on Electromagnetic Compatibility, APEMC 2010 2010), 272-273.
11. W. R. Fahrner, R. Job, and M. Werner, "Sensors and smart electronics in harsh environment applications," Microsystem Technologies **7**, 138-144 (2001).
12. Z. H. Wu, P. T. Lai, and J. K. O. Sin, "A new high-temperature thermal sensor based on large-grain polysilicon on insulator," Sensors and Actuators A: Physical **130-131**, 129-134 (2006).
13. G. Rinaldi and et al., "Dynamic pressure as a measure of gas turbine engine (GTE) performance," Measurement Science and Technology **21**, 045201 (2010).
14. S. Esquivel and et al., "Nonlocal thin films in calculations of the Casimir force," Physical Review B **72**(2005).
15. N. G. Wright and A. B. Horsfall, "SiC sensors: a review," Journal of Physics D: Applied Physics **40**, 6345 (2007).
16. D. R. Sparks, "Application of MEMS technology in automotive sensors and actuators," in *Micromechatronics and Human Science, 1998. MHS '98. Proceedings of the 1998 International Symposium on*, 1998), 9-15.
17. J. Zhou, S. Dasgupta, H. Kobayashi, J. M. Wolff, H. E. Jackson, and J. T. Boyd, "Optically interrogated MEMS pressure sensors for propulsion applications," Optical Engineering **40**, 598-604 (2001).

18. T. Kvisterøy, O. H. Gusland, B. Stark, H. Nakstad, M. Eriksrud, and B. Bjørnstad, "Optically excited silicon sensor for permanently installed downhole pressure monitoring applications," Sensors and Actuators A: Physical **31**, 164-167 (1992).
19. M. Tanaka, "An industrial and applied review of new MEMS devices features," Microelectronic Engineering **84**, 1341-1344.
20. B. S. Douma, P. Eigenraam, and P. Hatlem, "Modelling the pressure and temperature sensitivity of an optically excited micromachined silicon sensor for permanently installed downhole monitoring systems," Sensors and Actuators A: Physical **31**, 215-219 (1992).
21. E. Udd, *Fiber optic sensors : an introduction for engineers and scientists*, Wiley series in pure and applied optics (Wiley, New York, 1991).
22. A. Morris, M. Kourmpetis, I. D. Dear, M. Sjödahl, and J. P. Dear, "Optical strain monitoring techniques for life assessment of components in power generation plants," Proceedings of the Institution of Mechanical Engineers, Part A: Journal of Power and Energy **221**, 1141-1152 (2007).
23. P. Ferraro and G. De Natale, "On the possible use of optical fiber Bragg gratings as strain sensors for geodynamical monitoring," Optics and Lasers in Engineering **37**, 115-130 (2002).
24. A. D. Kersey, "Opticaleiber sensors for permanent downwell monitoring applications in the oil and gas industry," IEICE Transactions on Electronics **E83-C**, 400-404 (2000).
25. P. M. Nellen, P. Mauron, A. Frank, U. Sennhauser, K. Bohnert, P. Pequignot, P. Bodor, and H. Brändle, "Reliability of fiber Bragg grating based sensors for downhole applications," Sensors and Actuators, A: Physical **103**, 364-376 (2003).
26. C. Zhan, Y. Zhu, S. Yin, and P. Ruffin, "Multi-parameter harsh environment sensing using asymmetric Bragg gratings inscribed by IR femtosecond irradiation," Optical Fiber Technology **13**, 98-107 (2007).
27. D. D. Davis, T. K. Gaylord, E. N. Glytsis, and S. C. Mettler, "Very-high-temperature stable CO_2-laser-induced long-period fibre gratings," Electronics Letters **35**, 740-742 (1999).
28. T. Erdogan, "Fiber grating spectra," Journal of Lightwave Technology **15**, 1277-1294 (1997).
29. E. Anemogiannis, E. N. Glytsis, and T. K. Gaylord, "Transmission characteristics of long-period fiber gratings having arbitrary azimuthal/radial refractive index variations," Journal of Lightwave Technology **21**, 218-227 (2003).
30. H. Xiao, J. Deng, Z. Wang, W. Huo, P. Zhang, M. Luo, G. R. Pickrell, R. G. May, and A. Wang, "Fiber optic pressure sensor with self-compensation capability for harsh environment applications," Optical Engineering **44**, 1-10 (2005).
31. A. Wang, H. Xiao, J. Wang, Z. Wang, W. Zhao, and R. G. May, "Self-calibrated interferometric-intensity-based optical fiber sensors," Journal of Lightwave Technology **19**, 1495-1501 (2001).
32. M. Luo, J. Hui, A. Jalomilo, J. Dong, R. A. Normann, and H. Xiao, "Fiber optic fabry-perot interferometric sensor interrogated by the amplified spontaneous emission of an erbium-doped fiber amplifier for geothermal applications," in 2005),

33. N. A. Riza, M. A. Arain, and F. Perez, "Harsh environments minimally invasive optical sensor using free-space targeted single-crystal silicon carbide," IEEE Sensors Journal **6**, 672-685 (2006).
34. N. A. Riza, F. Ghauri, and F. Perez, "Silicon carbide-based remote wireless optical pressure sensor," IEEE Photonics Technology Letters **19**, 504-506 (2007).
35. G. A. Bufetova, V. V. Kashin, D. A. Nikolaev, Y. M. Papin, S. Y. Rusanov, V. F. Seregin, I. A. Shcherbakov, V. B. Tsvetkov, and A. A. Yakovlev, "Zonal doped crystal fibers for temperature measurements," Laser Physics Letters **4**, 440-443 (2007).
36. Y. Zhang, G. R. Pickrell, B. Qi, A. Safaai-Jazi, and A. Wang, "Single-crystal sapphire-based optical high-temperature sensor for harsh environments," Optical Engineering **43**, 157-164 (2004).
37. Y. Zhu, Z. Huang, F. Shen, and A. Wang, "Sapphire-fiber-based white-light interferometric sensor for high-temperature measurements," Optics Letters **30**, 711-713 (2005).
38. D. Grobnic, S. J. Mihailov, C. W. Smelser, and H. Ding, "Sapphire fiber bragg grating sensor made using femtosecond laser radiation for ultrahigh temperature applications," IEEE Photonics Technology Letters **16**, 2505-2507 (2004).
39. C. Zhan, J. H. Kim, J. Lee, S. Yin, P. Ruffin, and C. Luo, "High temperature sensing using higher-order-mode rejected sapphire-crystal fiber gratings," in Photonic Fiber and Crystal Devices: Advances in Materials and Innovations in Device Applications 2007),
40. G. N. Merberg and J. A. Harrington, "Optical and mechanical properties of single-crystal sapphire optical fibers," Applied Optics **32**, 3201-3209 (1993).
41. R. K. Nubling and J. A. Harrington, "Optical properties of single-crystal sapphire fibers," Applied Optics **36**, 5934-5940 (1997).
42. A. International Energy, *World energy outlook 2002* (OECD/IEA, Paris, 2002).
43. M. Susan and R. R. Robert, "Sensors and Controls Workshop Summary Report" (2008), retrieved.
44. D. G. Hawkins, D. A. Lashof, and R. H. Williams, "CARBON CAPTURE AND STORAGE - What to Do about Coal - Coal is plentiful, but we must manage its environmental dark side," Scientific American. **295**, 68 (2006).
45. B. S. Kawasaki, K. O. Hill, D. C. Johnson, and Y. Fujii, "Narrow-band Bragg reflectors in optical fibers," Optics Letters **3**, 66-68 (1978).
46. K. O. Hill, "Photosensitivity in optical fiber waveguides: From discovery to commercialization," IEEE Journal on Selected Topics in Quantum Electronics **6**, 1186-1189 (2000).
47. D. K. Lam and B. K. Garside, "Characterization of single-mode optical fiber filters," Applied Optics **20**, 440-445 (1981).
48. G. Meltz, W. W. Morey, and W. H. Glenn, "Formation of Bragg gratings in optical fibers by a transverse holographic method," Optics Letters **14**, 823-825 (1989).
49. A. D. Kersey, M. A. Davis, H. J. Patrick, M. LeBlanc, K. P. Koo, C. G. Askins, M. A. Putnam, and E. J. Friebele, "Fiber grating sensors," Journal of Lightwave Technology **15**, 1442-1462 (1997).

50. A. M. Vengsarkar, P. J. Lemaire, J. B. Judkins, V. Bhatia, T. Erdogan, and J. E. Sipe, "Long-period fiber gratings as band-rejection filters," Journal of Lightwave Technology **14**, 58-64 (1996).
51. S. W. James and R. P. Tatam, "Optical fibre long-period grating sensors: Characteristics and application," Measurement Science and Technology **14**(2003).
52. V. Bhatia, "Applications of long-period gratings to single and multi-parameter sensing," Optics Express **4**, 457-466 (1999).
53. N. D. Rees, S. W. James, R. P. Tatam, and G. J. Ashwell, "Optical fiber long-period gratings with Langmuir-Blodgett thin-film overlays," Optics Letters **27**, 686-688 (2002).
54. X. Shu, L. Zhang, and I. Bennion, "Sensitivity characteristics of long-period fiber gratings," Journal of Lightwave Technology **20**, 255-266 (2002).
55. V. Bhatia and A. M. Vengsarkar, "Optical fiber long-period grating sensors," Optics Letters **21**, 692-694 (1996).
56. H. J. Patrick, A. D. Kersey, and F. Bucholtz, "Analysis of the response of long period fiber gratings to external index of refraction," Journal of Lightwave Technology **16**, 1606-1612 (1998).
57. D. Flannery, S. W. James, R. P. Tatam, and G. J. Ashwell, "Fiber-optic chemical sensing with Langmuir-Blodgett overlay waveguides," Applied Optics **38**, 7370-7374 (1999).
58. I. D. Villar, I. R. Mat ás, F. J. Arregui, and P. Lalanne, "Optimization of sensitivity in Long Period Fiber Gratings with overlay deposition," Optics Express **13**, 56-69 (2005).
59. Z. Wang, J. R. Heflin, R. H. Stolen, and S. Ramachandran, "Analysis of optical response of long period fiber gratings to nm-thick thin-film coatings," Optics Express **13**, 2808-2813 (2005).
60. A. Cusano, A. Iadicicco, P. Pilla, L. Contessa, S. Campopiano, A. Cutolo, and M. Giordano, "Cladding mode reorganization in high-refractive-index-coated long-period gratings: Effects on the refractive-index sensitivity," Optics Letters **30**, 2536-2538 (2005).
61. Y. J. Rao, Z. L. Ran, X. Liao, and H. Y. Deng, "Hybrid LPFG/MEFPI sensor for simultaneous measurement of high-temperature and strain," Optics Express **15**, 14936-14941 (2007).
62. Y. J. Rao, S. F. Yuan, X. K. Zeng, D. K. Lian, Y. Zhu, Y. P. Wang, S. L. Huang, T. Y. Liu, G. F. Fernando, L. Zhang, and I. Bennion, "Simultaneous strain and temperature measurement of advanced 3-D braided composite materials using an improved EFPI/FBG system," Optics and Lasers in Engineering **38**, 557-566 (2002).
63. Y. P. Wang, D. N. Wang, and W. Jin, "CO_2 laser-grooved long period fiber grating temperature sensor system based on intensity modulation," Applied Optics **45**, 7966-7970 (2006).
64. D. D. Davis, T. K. Gaylord, E. N. Glytsis, S. G. Kosinski, S. C. Mettler, and A. M. Vengsarkar, "Long-period fibre grating fabrication with focused CO_2 laser pulses," Electronics Letters **34**, 302-303 (1998).

65. Y. J. Rao, Y. P. Wang, Z. L. Ran, and T. Zhu, "Novel fiber-optic sensors based on long-period fiber gratings written by high-frequency CO_2 laser pulses," Journal of Lightwave Technology **21**, 1320-1327 (2003).
66. Y. Kondo, K. Nouchi, T. Mitsuyu, M. Watanabe, P. G. Kazansky, and K. Hirao, "Fabrication of long-period fiber gratings by focused irradiation of infrared femtosecond laser pulses," Optics Letters **24**, 646-648 (1999).
67. S. H. Nam, C. Zhan, J. Lee, C. Hahn, K. Reichard, P. Ruffin, K. L. Deng, and S. Yin, "Bend-insensitive ultra short long-period gratings by the electric arc method and their applications to harsh environment sensing and communication," Optics Express **13**, 731-737 (2005).
68. S. G. Kosinski and A. M. Vengsarkar, "Splicer-based long-period fiber gratings," in Proceedings of the 1998 Optical Fiber Communication Conference, OFC'98 (IEEE, 1998), 278-279.
69. G. Humbert, A. Malki, S. Février, P. Roy, and D. Pagnoux, "Characterizations at high temperatures of long-period gratings written in germanium-free air-silica microstructure fiber," Optics Letters **29**, 38-40 (2004).
70. M. Fujimaki, Y. Ohki, J. L. Brebner, and S. Roorda, "Fabrication of long-period optical fiber gratings by use of ion implantation," Optics Letters **25**, 88-89 (2000).
71. Y. Jeong, B. Yang, B. Lee, H. S. Seo, S. Choi, and K. Oh, "Electrically Controllable Long-Period Liquid Crystal Fiber Gratings," IEEE Photonics Technology Letters **12**, 519-521 (2000).
72. S. Savin, M. J. F. Digonnet, G. S. Kino, and H. J. Shaw, "Tunable mechanically induced long-period fiber gratings," Optics Letters **25**, 710-712 (2000).
73. T. Yokouchi, Y. Suzaki, K. Nakagawa, M. Yamauchi, M. Kimura, Y. Mizutani, S. Kimura, and S. Ejima, "Thermal tuning of mechanically induced long-period fiber grating," Applied Optics **44**, 5024-5028 (2005).
74. T. Wei, J. Montoya, J. Zhang, J. Dong, and H. Xiao, "Fabrication of long-period fiber gratings by CO2 laser irradiations for high temperature applications," in Sensors for Harsh Environments III 2007),
75. W. R. Young, "Modes of optical waveguides," 1978).
76. J.-R. Qian and W.-P. Huang, "LP MODES AND IDEAL MODES ON OPTICAL FIBERS," Journal of Lightwave Technology **LT-4**, 626-630 (1986).
77. A. W. Snyder and J. D. Love, *Optical waveguide theory*, Science paperbacks, 190 (Chapman and Hall, London; New York, 1983).
78. D. Gloge, "Weakly guiding fibers," Applied Optics **10**, 2252-2258 (1971).
79. B. H. Kim, Y. Park, T. J. Ahn, D. Y. Kim, B. H. Lee, Y. Chung, U. C. Paek, and W. T. Han, "Residual stress relaxation in the core of optical fiber by CO_2 laser irradiation," Optics Letters **26**, 1657-1659 (2001).
80. T. Erdogan, "Cladding-mode resonances in short- and long-period fiber grating filters," Journal of the Optical Society of America A: Optics and Image Science, and Vision **14**, 1760-1773 (1997).
81. D. Marcuse, *Integrated optics* (IEEE Press, New York, 1973).
82. U. C. Paek and C. R. Kurkjian, "CALCULATION OF COOLING RATE AND INDUCED STRESSES IN DRAWING OF OPTICAL FIBERS," Journal of the American Ceramic Society **58**, 330-335 (1975).

83. Y. Hibino, F. Hanawa, T. Abe, and S. Shibata, "Residual stress effects on refractive indices in undoped silica-core single-mode fibers," Applied Physics Letters **50**, 1565-1566 (1987).
84. M. Akiyama, K. Nishide, K. Shima, A. Wada, and R. Yamauchi, "Novel long-period fiber grating using periodically released residual stress of pure-silica core fiber," in 1998), 276-277.
85. C. S. Kim, Y. Han, B. H. Lee, W. T. Han, U. C. Paek, and Y. Chung, "Induction of the refractive index change in B-doped optical fibers through relaxation of the mechanical stress," Optics Communications **185**, 337-342 (2000).
86. A. C. Hardy and F. H. Perrin, *The principles of optics*, International series in physics (McGraw-Hill book company, inc., New York; London, 1932).
87. F. Dürr, G. Rego, P. V. S. Marques, S. L. Semjonov, E. M. Dianov, H. G. Limberger, and R. P. Salathé, "Tomographic stress profiling of arc-induced long-period fiber gratings," Journal of Lightwave Technology **23**, 3947-3953 (2005).
88. B. H. Kim, T. J. Ahn, D. Y. Kim, B. H. Lee, Y. Chung, U. C. Paek, and W. T. Han, "Effect of CO_2 laser irradiation on the refractive-index change in optical fibers," Applied Optics **41**, 3809-3815 (2002).
89. B. Qi, G. R. Plckrell, J. C. Xu, P. Zhang, Y. Duan, W. Peng, Z. Huang, W. Huo, H. Xiao, R. G. May, and A. Wang, "Novel data processing techniques for dispersive white light interferometer," Optical Engineering **42**, 3165-3171 (2003).
90. T. Wei, Y. Han, Y. Li, H. L. Tsai, and H. Xiao, "Temperature-insensitive miniaturized fiber inline Fabry-Perot interferometer for highly sensitive refractive index measurement," Optics Express **16**, 5764-5769 (2008).
91. Y. Liu, K. S. Chiang, Y. J. Rao, Z. L. Ran, and T. Zhu, "Light coupling between two parallel CO_2-laser written long-period fiber gratings," Optics Express **15**, 17645-17651 (2007).
92. W. P. Jakubik, M. W. Urbańczyk, S. Kochowski, and J. Bodzenta, "Bilayer structure for hydrogen detection in a surface acoustic wave sensor system," Sensors and Actuators, B: Chemical **82**, 265-271 (2002).
93. Z. Zhao, M. A. Carpenter, H. Xia, and D. Welch, "All-optical hydrogen sensor based on a high alloy content palladium thin film," Sensors and Actuators, B: Chemical **113**, 532-538 (2006).
94. M. Slaman, B. Dam, M. Pasturel, D. M. Borsa, H. Schreuders, J. H. Rector, and R. Griessen, "Fiber optic hydrogen detectors containing Mg-based metal hydrides," Sensors and Actuators, B: Chemical **123**, 538-545 (2007).
95. M. Pasturel, M. Slaman, H. Schreuders, J. H. Rector, D. M. Borsa, B. Dam, and R. Griessen, "Hydrogen absorption kinetics and optical properties of Pd-doped Mg thin films," Journal of Applied Physics **100**(2006).
96. M. E. Davis, "Ordered porous materials for emerging applications," Nature **417**, 813-821 (2002).
97. J. L. Meinershagen and T. Bein, "Optical sensing in nanopores. Encapsulation of the solvatochromic dye nile red in zeolites," Journal of the American Chemical Society **121**, 448-449 (1999).
98. S. M. Auerbach, K. A. Carrado, and P. K. Dutta, *Handbook of zeolite science and technology* (M. Dekker, New York, 2003).

99. S. M. Kuznicki, V. A. Bell, S. Nair, H. W. Hillhouse, R. M. Jacubinas, C. M. Braunbarth, B. H. Toby, and M. Tsapatsis, "A titanosilicate molecular sieve with adjustable pores for sizeselective adsorption of molecules," Nature. **412**, 720 (2001).
100. X. Gu, Z. Tang, and J. Dong, "On-stream modification of MFI zeolite membranes for enhancing hydrogen separation at high temperature," Microporous and Mesoporous Materials **111**, 441-448 (2008).
101. H. Xiao, J. Zhang, J. Dong, M. Luo, R. Lee, and V. Romero, "Synthesis of MFI zeolite films on optical fibers for detection of chemical vapors," Optics Letters **30**, 1270-1272 (2005).
102. J. Zhang, J. Dong, M. Luo, H. Xiao, S. Murad, and R. A. Normann, "Zeolite-fiber integrated optical chemical sensors for detection of dissolved organics in water," Langmuir **21**, 8609-8612 (2005).
103. J. Zhang, M. Luo, H. Xiao, and J. Dong, "Interferometric study on the adsorption-dependent refractive index of silicalite thin films grown on optical fibers," Chemistry of Materials **18**, 4-6 (2006).
104. M. Chomát, D. Berková, V. Matějec, I. Kašík, J. Kaňka, R. Slavík, A. Jančárek, and P. Bittner, "Responses of a long-period grating fabricated in a graded-index optical fiber to temperature and refractive-index changes," Materials Science and Engineering C **26**, 457-461 (2006).
105. S. H. Aref, R. Amezcua-Correa, J. P. Carvalho, O. Fraz ão, P. Caldas, J. L. Santos, F. M. Ara újo, H. Latifi, F. Farahi, L. A. Ferreira, and J. C. Knight, "Modal interferometer based on hollow-core photonic crystal fiber for strain and temperature measurement," Optics Express **17**, 18669-18675 (2009).
106. H. Y. Choi, M. J. Kim, and B. H. Lee, "All-fiber Mach-Zehnder type interferometers formed in photonic crystal fiber," Optics Express **15**, 5711-5720 (2007).
107. O. Fraz ão, R. Falate, J. L. Fabris, J. L. Santos, L. A. Ferreira, and F. M. Ara újo, "Optical inclinometer based on a single long-period fiber grating combined with a fused taper," Optics Letters **31**, 2960-2962 (2006).
108. B. Gu, M. J. Yin, A. P. Zhang, J. W. Qian, and S. He, "Low-cost high-performance fiber-optic pH sensor based on thin-core fiber modal interferometer," Optics Express **17**, 22296-22302 (2009).
109. R. Jha, J. Villatoro, G. Badenes, and V. Pruneri, "Refractometry based on a photonic crystal fiber interferometer," Optics Letters **34**, 617-619 (2009).
110. M. Jiang, A. P. Zhang, Y. C. Wang, H. Y. Tam, and S. He, "Fabrication of a compact reflective long-period grating sensor with a cladding-mode-selective fiber end-face mirror," Optics Express **17**, 17976-17982 (2009).
111. J. Ju, L. Ma, W. Jin, and Y. Hu, "Photonic bandgap fiber tapers and in-fiber interferometric sensors," Optics Letters **34**, 1861-1863 (2009).
112. L. V. Nguyen, D. Hwang, S. Moon, D. S. Moon, and Y. Chung, "High temperature fiber sensor with high sensitivity based on core diameter mismatch," Optics Express **16**, 11369-11375 (2008).
113. Z. Tian and S. S. H. Yam, "In-line single-mode optical fiber interferometric refractive index sensors," Journal of Lightwave Technology **27**, 2296-2306 (2009).

114. Z. Tian, S. S. H. Yam, and H. P. Loock, "Single-mode fiber refractive index sensor based on core-offset attenuators," IEEE Photonics Technology Letters **20**, 1387-1389 (2008).
115. Z. Tian, S. S. H. Yam, and H. P. Loock, "Refractive index sensor based on an abrupt taper Michelson interferometer in a single-mode fiber," Optics Letters **33**, 1105-1107 (2008).
116. J. Villatoro, V. P. Minkovich, V. Pruneri, and G. Badenes, "Simple all-microstructured-optical-fiber interferometer built via fusion splicing," Optics Express **15**, 1491-1496 (2007).
117. J. Villatoro and D. Monzón-Hernández, "Low-cost optical fiber refractive-index sensor based on core diameter mismatch," Journal of Lightwave Technology **24**, 1409-1413 (2006).
118. T. Wei, X. Lan, and H. Xiao, "Fiber inline core-cladding-mode Mach-Zehnder interferometer fabricated by two-point CO_2 laser irradiations," IEEE Photonics Technology Letters **21**, 669-671 (2009).
119. E. Li, X. Wang, and C. Zhang, "Fiber-optic temperature sensor based on interference of selective higher-order modes," Applied Physics Letters **89**(2006).
120. J. Canning and A. L. G. Carter, "Modal interferometer for in situ measurements of induced core index change in optical fibers," Optics Letters **22**, 561-563 (1997).
121. B. H. Lee and J. Nishii, "Self-interference of long-period fibre grating and its application as temperature sensor," Electronics Letters **34**, 2059-2060 (1998).
122. E. M. Dianov, S. A. Vasiliev, A. S. Kurkov, O. I. Medvedkov, and V. N. Protopopov, "In-fiber Mach-Zehnder interferometer based on a pair of long-period gratings," in *Optical Communication, 1996. ECOC '96. 22nd European Conference on*, 1996), 65-68 vol.61.
123. Y. J. Kim, U. C. Paek, and B. H. Lee, "Measurement of refractive-index variation with temperature by use of long-period fiber gratings," Optics Letters **27**, 1297-1299 (2002).
124. T. Allsop, R. Reeves, D. J. Webb, I. Bennion, and R. Neal, "A high sensitivity refractometer based upon a long period grating Mach-Zehnder interferometer," Review of Scientific Instruments **73**, 1702 (2002).
125. D. W. Stowe, D. R. Moore, and R. G. Priest, "POLARIZATION FADING IN FIBER INTERFEROMETRIC SENSORS," IEEE J QUANTUM ELECTRON **V QE-18**, 1644-1647 (1982).
126. A. D. Kersey, "A review of recent developments in fiber optic sensor technology," Optical Fiber Technology **2**, 291-317 (1996).
127. C. E. Lee and H. F. Taylor, "Interferometric optical fibre sensors using internal mirrors," Electronics Letters **24**, 193-194 (1988).
128. K. A. Murphy, M. F. Gunther, A. Wang, R. O. Claus, and A. M. Vengsarkar, "Extrinsic Fabry-Perot Optical Fiber Sensor," in *Optical Fiber Sensors Conference, 1992. 8th*, 1992), 193-196.
129. H. Xiao, J. Deng, G. Pickrell, R. G. May, and A. Wang, "Single-Crystal Sapphire Fiber-Based Strain Sensor for High-Temperature Applications," Journal of Lightwave Technology **21**, 2276-2283 (2003).
130. Y. Zhu and A. Wang, "Miniature fiber-optic pressure sensor," IEEE Photonics Technology Letters **17**, 447-449 (2005).

131. M. Schmidt, B. Werther, N. Fürstenau, M. Matthias, and T. Melz, "Fiber-optic extrinsic Fabry-Perot interferometer strain sensor with <50 pm displacement resolution using three-wavelength digital phase demodulation," Optics Express **8**, 475-480 (2001).
132. K. D. Oh, A. Wang, and R. O. Claus, "Fiber-optic extrinsic Fabry-Perot dc magnetic field sensor," Optics Letters **29**, 2115-2117 (2004).
133. W. Peng, G. R. Pickrell, F. Shen, and A. Wang, "Experimental investigation of optical waveguide-based multigas sensing," IEEE Photonics Technology Letters **16**, 2317-2319 (2004).
134. M. Han, X. Wang, J. Xu, K. L. Cooper, and A. Wang, "Diaphragm-based extrinsic Fabry-Perot interferometric optical fiber sensor for acoustic wave detection under high background pressure," Optical Engineering **44**, 1-2 (2005).
135. G. Z. Xiao, A. Adnet, Z. Zhang, F. G. Sun, and C. P. Grover, "Monitoring changes in the refractive index of gases by means of a fiber optic Fabry-Perot interferometer sensor," Sensors and Actuators A: Physical **118**, 177-182 (2005).
136. T. Liu and G. F. Fernando, "A frequency division multiplexed low-finesse fiber optic Fabry-Perot sensor system for strain and displacement measurements," Review of Scientific Instruments **71**, 1275-1278 (2000).
137. V. Bhatia, K. A. Murphy, R. O. Claus, M. E. Jones, J. L. Grace, T. A. Tran, and J. A. Greene, "Optical fibre based absolute extrinsic Fabry-Pérot interferometric sensing system," Measurement Science and Technology **7**, 58-61 (1996).
138. Y. Zhang, X. Chen, Y. Wang, K. L. Cooper, and A. Wang, "Microgap multicavity Fabry-Pérot biosensor," Journal of Lightwave Technology **25**, 1797-1804 (2007).
139. Y. Zhang, H. Shibru, K. L. Cooper, and A. Wang, "Miniature fiber-optic multicavity Fabry-Perot interferometric biosensor," Optics Letters **30**, 1021-1023 (2005).
140. Z. L. Ran, Y. J. Rao, W. J. Liu, X. Liao, and K. S. Chiang, "Laser-micromachined Fabry-Perot optical fiber tip sensor for high-resolution temperatureindependent measurement of refractive index," Optics Express **16**, 2252-2263 (2008).
141. M. Li, S. Menon, J. P. Nibarger, and G. N. Gibson, "Ultrafast Electron Dynamics in Femtosecond Optical Breakdown of Dielectrics," Physical Review Letters **82**, 2394-2397 (1999).
142. A. Szameit, D. Blömer, J. Burghoff, T. Pertsch, S. Nolte, and A. Tünnermann, "Hexagonal waveguide arrays written with fs-laser pulses," Applied Physics B: Lasers and Optics **82**, 507-512 (2006).
143. Y. Cheng, H. L. Tsai, K. Sugioka, and K. Midorikawa, "Fabrication of 3D microoptical lenses in photosensitive glass using femtosecond laser micromachining," Applied Physics A: Materials Science and Processing **85**, 11-14 (2006).
144. H. Sun, F. He, Z. Zhou, Y. Cheng, Z. Xu, K. Sugioka, and K. Midorikawa, "Fabrication of microfluidic optical waveguides on glass chips with femtosecond laser pulses," Optics Letters **32**, 1536-1539 (2007).
145. Y. J. Rao, M. Deng, D. W. Duan, X. C. Yang, T. Zhu, and G. H. Cheng, "Micro Fabry-Perot interferometers in silica fibers machined by femtosecond laser," Optics Express **15**, 14123-14128 (2007).

146. T. Wei, Y. Han, H. L. Tsai, and H. Xiao, "Miniaturized fiber inline Fabry-Perot interferometer fabricated with a femtosecond laser," Optics Letters **33**, 536-538 (2008).
147. G. Z. Xiao, A. Adnet, Z. Zhang, F. G. Sun, and C. P. Grover, "Monitoring changes in the refractive index of gases by means of a fiber optic Fabry-Perot interferometer sensor," Sensors and Actuators, A: Physical **118**, 177-182 (2005).
148. J. B. Hawkes and R. W. Astheimer, "The temperature coefficient of the refractive index of water," Journal of the Optical Society of America **38**, 804-806 (1948).

VITA

Tao Wei was born on September 23, 1983 in Nanjing, China. In June 2002, he obtained a bachelor's degree in Department of Mechanical Engineering from Nanjing University of Technology, Nanjing, China. In August 2006, he enrolled at the University of Missouri-Rolla to pursue a master's degree in Department of Electrical and Computer Engineering under the guidance of Dr. Hai Xiao. He received his Master of Science Degree in Electrical Engineering in 2008.

In January 2008, he continued his study towards a doctoral degree in Department of Electrical and Computer Engineering under the guidance of Dr. Hai Xiao. He received his Doctor of Philosophy in Electrical Engineering in 2010. During his graduate study, he authored and co-authored 1 book chapter, 14 journal papers and more than 10 conference papers. He reviewed more than 7 papers for Journal of Sensor, Applied Optics, Journal of Optical Society of America A and Optical Express.